Magnetic and Spintronic Properties of Rare-Earth Iron Garnets

By

Ethan Rosenberg

B.S., UCLA (2015)

Submitted to the Department of Materials Science and Engineering

In partial fulfillment of the requirements for the degree of

Doctor of Philosophy

at the

MASSACHUSETTS INSTITUTE OF TECHNOLOGY

June 2021

Signature of Author……

Department of Materials Science and Engineering

May 14, 2021

Certified by……

Caroline A. Ross

Professor of Materials Science and Engineering

Thesis Supervisor

Accepted by…….....

Frances M. Ross

Professor of Materials Science and Engineering

Chair, Departmental Committee on Graduate Studies

Magnetic and Spintronic Properties of Rare-Earth Iron Garnet Thin Films

By

Ethan Rosenberg

B.S., UCLA (2015)

Submitted to the Department of Materials Science and Engineering

In partial fulfillment of the requirements for the degree of

Doctor of Philosophy

Abstract

Rare earth iron garnets (REIG) can be grown as thin films with strain-induced perpendicular magnetic anisotropy (PMA), and their potential for spintronic device applications has been studied extensively in recent years. In particular, thulium iron garnet (TmIG) has excited great interest due to record-breaking spin orbit torque-driven domain wall velocities over 2km/s and the presence of the Dzyaloshinskii-Moriya interaction, which stabilizes chiral Néel domain walls. In order to optimize REIG for these applications, it is useful to develop methods for tuning their magnetic and spintronic properties. In this work, we accomplish this through varying the RE site occupancy.

We report the growth and characterization of fully-strained terbium iron garnet (TbIG) and europium iron garnet (EuIG) with PMA ranging in thickness from 10 to 80 nm. EuIG can be grown with PMA on (100) and (111) gadolinium gallium garnet (GGG) substrates, making it ideal for orientation-dependent studies. For instance, Pt/EuIG had similar (001) and (111) imaginary spin mixing conductances of 4.6-5.4$\times10^{12}$ $\Omega^{-1}m^{-2}$ in contrast to similar studies on the Pt/CFO system. The (111) imaginary spin mixing conductance of Pt/TbIG (4.6×10^{12} $\Omega^{-1}m^{-2}$) was similar to the Pt/EuIG system, and both Pt/TbIG and Pt/EuIG had comparable spin mixing conductances to Pt/TmIG.

The TbIG films had a low saturation magnetization (~30 emu/cc) at room temperature due to their easily accessible magnetic compensation point of 330K, and anomalous Hall effect measurements of Pt/TbIG showed a sign change at the compensation point. Through a combination of x-ray absorption measurements and molecular field simulations, we propose a model to explain this observation involving point defects such as iron vacancies and terbium antisite defects.

We also report the static and dynamic magnetic properties of yttrium substituted thulium iron garnet (Y:TmIG) thin films on GGG as a function of Y concentration. We report the tunability of the magnetic anisotropy energy, with full control achieved over the type of anisotropy (from perpendicular, to isotropic, to an in-plane easy axis) on the same substrate. In addition, we report a nonmonotonic composition-dependent anisotropy term, which we ascribe to growth-induced anisotropy similar to what has been reported in garnet thin films grown by liquid-phase epitaxy. Ferromagnetic resonance shows linear variation of the damping and the g-factor across the composition range, consistent with prior theoretical work. Domain imaging reveals differences in reversal modes, remanant states, and domain sizes in Y_xTm_{3-x} iron-garnet thin films as a function of anisotropy.

Acknowledgements

I would like to extend my sincere gratitude to a number of people who were instrumental in my completion of this thesis.

My advisor, Professor Caroline A. Ross, for taking me into her laboratory and teaching me what I know today about research. Without her guidance and constant support, this thesis would never have been possible.

My thesis committee members, Professor Geoffrey S.D. Beach and Professor Juejun Hu, for their invaluable insight regarding my thesis work.

Members of the Ross group, past and present, who provided me with their own perspectives regarding research. I would especially like to thank my office-mate, Jackson Bauer, for being a great conversation partner and collaborator. I would also like to thank Enno Lage and Andy Quindeau for starting me out in the garnet field.

Members of the Beach group, for welcoming an outsider into their laboratories and offices. It was a pleasure to spend time with them both in and out of the lab.

David Bono, who taught me everything I know about electronics and instrumentation and who has been a great role model and friend throughout my PhD.

The MRL staff scientists Charlie Settens and Elisabeth Shaw, the MTL staff, and Mike Tarkanian, James Hunter, and Shaymus Hudson. Without their help none of the characterization work in this thesis would have been feasible.

The staff of beamline 4-IDC at Argonne National Laboratory, Professor Frank de Groot, and Dr. Johnny Pelliciari for helping me collect and analyze XAS and XMCD data.

Dr. Hans Nembach, Dr. Justin Shaw, and Dr. Grant Reilly for being great collaborators

The “DMSE Dream Team” (Core members: Peter Su and Karthik Akkiraju) at 72 Dane Street, Apt 3 for being the best roommates and support system I could have asked for, especially during the COVID lockdown.

Jack Stropko and Joey Gu for being great roommates during my final year.

Jack Stropko and Bao Minh Hoang for being great friends and giving me the opportunity to escape MIT and travel around the country.

The MIT/Harvard music community (MITSO, MIT CMS, Ambient Ensemble, Harvard Summer Pops, and MIT VGO) for giving me an artistic outlet away from research.

Total Performance Sports for teaching me the value of hard physical work and pulling me out of the lab twice a week to work out my frustrations.

Dr. Viktor Frankl, who I never met but whose work helped me as it has helped millions of others around the world.

My family (Moshe Rosenberg, Yael Rosenberg, Shirley Miller, Steve Miller, Daniel Miller, and Zipora Mor), who have supported me in more ways that I can write here throughout my studies. I cannot thank them enough.

Table of Contents

List of Figures

3.A3 Macrospin fit of SMR data from (111) Pt/EuIG

3.A4 Quantification of Tb $3d_{5/2}$ XPS spectrum

4.1 XMCD fingerprints of iron L-edge features

4.2 Normalized XAS data

4.3 Comparison of bulk and thin-film compensation temperatures

4.4 Normalized XMCD data from bulk and thin film samples

4.5 Best fit calculated XMCD spectra

4.6 Simulated compensation temperatures for TbIG with point defects

4.7 M(T) data taken near T_{Curie} for thin film and bulk samples

4.A1 Powder XRD and Rietveld refinement from bulk TbIG sample

4.A2 XPS survey scan from thin film and bulk TbIG samples

4.A3 High-resolution XPS of Tb 4d peak in thin film and bulk samples

5.1 Structural characterization of $Y_xTm_{3-x}IG$ thin films

5.2 Out-of-plane and in-plane VSM hysteresis loops from $Y_xTm_{3-x}IG$ thin films

5.3 Extracted anisotropy and magnetostriction from $Y_xTm_{3-x}IG$ thin films

5.4 FMR characterization data and extracted g factors and damping from $Y_xTm_{3-x}IG$ thin films

5.5 AC demagnetized MOKE images from TmIG and $Y_{0.51}Tm_{2.49}IG$ thin films

5.6 MOKE microscope hysteresis loops from TmIG and $Y_{0.51}Tm_{2.49}IG$ thin films

5.A1 HRXRD fitting results from selected $Y_xTm_{3-x}IG$ thin films

5.A2 XPS depth profiles from selected $Y_xTm_{3-x}IG$ thin films

5.A3 HRXRD scans of YIG/GGG and YIG/SGGG

5.A4 In-plane VSM scans of YIG/GGG and YIG/SGGG

5.A5 Out-of-plane VSM scan of YIG/SGGG

5.A6 Multiple FMR resonances in $Y_{0.51}Tm_{2.49}IG$ thin films

5.A7 Multiple FMR resonances in YIG

5.A8 FMR data from the backside of $Y_{0.51}Tm_{2.49}IG$ to isolate the GGG background signal

5.A9 Relative signal strengths of film and substrate signals

6.1 SOT switching results for Pt/TmIG Hall bars

6.2 SMR and MOKE characterization of Pt/TmIG domain wall tracks

6.3 Field-induced domain-wall depinning results from Pt/TmIG domain wall tracks

6.4 Structural characterization, magnetic characterization and compositional mapping of TmIG/GGG thin films

6.5 SOT efficiency and DMI energies for TmIG/GGG domain wall tracks

6.6 Tm M-edge XAS/XMCD data and sum rule analysis

List of Tables

Chapter 1

Introduction

1.1 Overview and Motivation

As microelectronics continue to scale to ever smaller technology nodes, a variety of problems arise. For example, SRAM and DRAM (memory technologies operating close to the core memory of a microprocessor) are plagued by high power consumption due to their inherent volatility and a widening speed gap[1]. One possible replacement for SRAM and DRAM is spin transfer torque magnetoresistive memory (STT-MRAM), which is a memory technology which uses the spin transfer torque (STT) effect to manipulate and store information in the magnetic state of a magnetic tunnel junction (MTJ)[2]. This technology is attractive due to its nonvolatility – unlike SRAM and DRAM, no power is required to maintain the state of an MTJ[1]. A great deal of research and development has gone into STT-MRAM technology, and it has already entered the market[2]. The current state-of-the-art commercially is a 256 Mb MRAM based on an MTJ with perpendicular magnetic anisotropy (PMA)[3].

Despite STT-MRAMs promise as an emerging memory technology, it is not without its own issues. Because the read and write current paths in an STT-MRAM bit are the same, accidental writing and damage of the tunnel barrier are possible[2]. In addition, STT-MRAM operation at high switching speeds (<10 ns) is hindered by switching incubation effects which greatly increase switching currents and broaden switching current distributions[2,4]. The most serious problem facing STT-MRAM, however, is the so-called MRAM trilemma: STT-MRAM bits must simultaneously

be able to write data with low writing currents, read data accurately (high TMR), and store data for long periods of time[2]. These goals are very difficult to achieve simultaneously[2,5].

One proposed solution to these problems is to use a newly discovered torque known as spin orbit torque (SOT) to manipulate the magnetization state of an MTJ[1,5]. SOT is activated by the flow of in-plane currents through a normal metal (NM) layer adjacent to the MTJ free layer, so this breaks the MRAM trilemma and protects the fragile tunnel barrier by separating the read and write paths[1,6]. Demonstrations of three-terminal perpendicular SOT-MRAM devices have already been achieved using all-metallic systems[1,5–7]. However, because the materials used in these devices acquire their anisotropy through an interfacial effect[2], they are unlikely to possess adequate thermal stability at small (~20 nm) technology nodes[8].

In recent years, a new approach to spintronic memories has been to use magnetic insulators as the storage medium. Insulators present a number of advantages over metallic magnets, including:

- Their low conductivity means that current is confined to the NM layer, leading to higher efficiencies.
- PMA in insulators can be caused by bulk phenomena such as magnetostriction or growth-induced anisotropy, enabling higher thermal stability.
- Some magnetic insulators have lower magnetic damping than metallic magnets, which is important for spin wave applications – namely, yttrium iron garnet (YIG) has the lowest damping of any material.

The first step towards magnetic insulator memory was the reported current-assisted switching of barium hexaferrite, but this material was too hard magnetically to support true current-induced

switching[9]. The first current-induced switching of a magnetic insulator was reported by our group in PMA Pt/thulium iron garnet (TmIG) heterostructures[10]. Since then, there has been an explosion of spintronic studies carried out on magnetic insulators, especially rare-earth iron garnets (REIG). Over the past five years, ultrafast domain wall motion (up to relativistic speeds)[11–14], chiral spin textures[11,13,15,16], and ultrafast current-induced switching[14] have all been reported in REIG materials. Clearly, these materials are promising for future spintronic memory applications. This thesis focuses on the development of new REIG materials for spintronic applications, focusing on the effects of substitution on the RE site in the crystal lattice.

1.2 Outline of Thesis

The remainder of Chapter 1 provides background on magnetism and spintronics in REIG materials. First, the garnet structure will be introduced. Then, the various sources of anisotropy in REIG thin films will be discussed. Finally, a review of recent spintronic studies in REIG thin film heterostructures will be provided.

Chapter 2 describes the experimental methods used in this thesis.

Chapter 3 discusses the perpendicular magnetic anisotropy and spintronic properties of EuIG and TbIG thin films.

Chapter 4 uses a combination of XMCD, XRD, molecular field simulations, and Curie temperature measurements to develop a model for the elevated compensation temperature in TbIG thin films.

Chapter 5 presents a systematic study of the static and dynamic magnetic properties of Y-substituted TmIG thin films. Full control over the anisotropy is achieved, with implications on the domain structure and reversal mechanism. Growth-induced anisotropy in this system is also discussed – one of the first reports of this type of anisotropy in PLD-grown thin films.

Chapter 6 encompasses a variety of spintronic studies on REIG materials that the author has contributed to.

Chapter 7 will summarize the previous chapters and provide a perspective on future work suggested by the results of this thesis.

1.3 Garnet Structure and Magnetism

Despite the relatively recent interest that REIG materials with PMA have attracted in the spintronics field, this class of materials is one of the oldest and most well-characterized in the history of magnetism. They were first discovered accidentally by Forestier and Guiot-Guillain while studying the properties of perovskites[17]. They then attracted the attention of workers such as Pauthenet, Gilleo, Geller, and Kittel, who studied the structure, stoichiometry, and magnetic interactions in garnets extensively over the next few decades. This intense interest culminated in the development of magneto-optical magnetic bubble memories, for which garnets were found to be ideally suited[18].

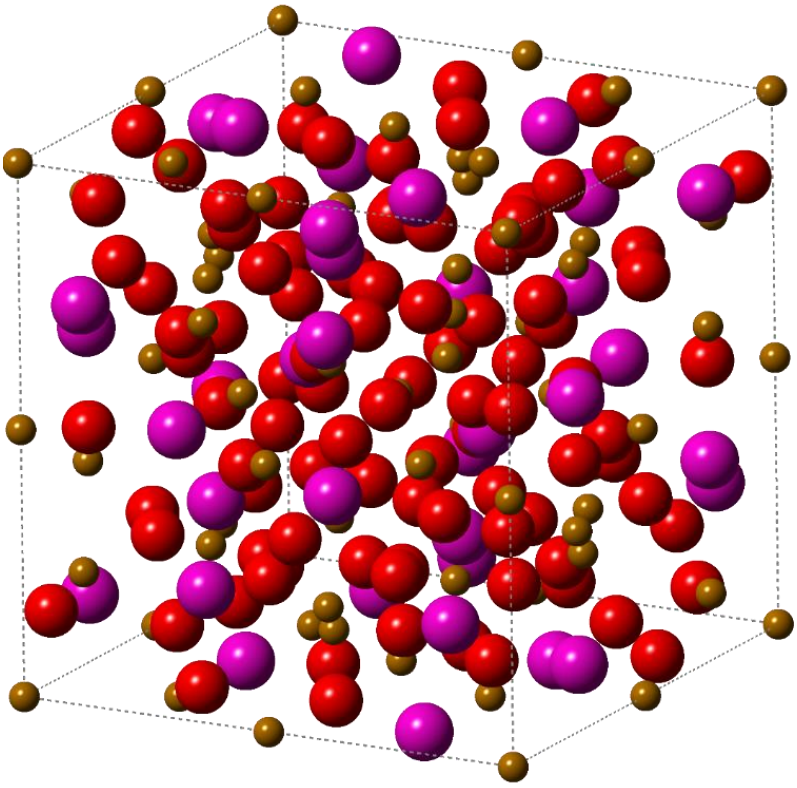

Figure 1.1: Garnet unit cell. Purple atoms are RE, yellow atoms are Fe, and red atoms are O.

REIG are so named because they have the same crystal structure as garnet minerals such as grossularite, $Ca_3Al_2Si_3O_{12}$[19]. However, a pure REIG makes the substitutions Ca→RE, (Al,Si)→Fe so that its formula unit is $RE_3Fe_5O_{12}$. A unit cell contains 8 of these formula units with various rotations and reflections (see Figure 1.1). Within the unit cell, the RE ions are dodecahedrally (c) coordinated by oxygen anions, two of the iron ions are octahedrally (a) coordinated, and three of the iron ions are tetrahedrally coordinated (d). Of course, as we will see later, real garnet materials can depart from this ideal stoichiometry and coordination structure.

Garnets, like other ferrites, are ferromagnetic due to the superexchange interaction[20], which is a symmetric exchange interaction between two transition metal ions mediated by an intervening

oxygen anion. Put simply, superexchange is a consequence of the bonding between the transition metal d orbitals and the oxygen p orbitals[21]. For instance, imagine the interaction between the $3d_{x^2-y^2}$ orbitals of a transition metal and the p_x orbital of oxygen. Even though the bond is largely ionic, some hopping is allowed between the metal cations and the oxygen anions. However, the p_x orbital can only support a spin up and a spin down electron due to the Pauli exclusion principle. Therefore, the Hund's rule tendency to stabilize the maximum S state within each transition metal ion plus the Pauli exclusion necessity for the shared electrons between the transition metal and the oxygen to have opposite spin stabilizes an antiferromagnetic arrangement of adjacent transition metal cations (see Figure 1.2). This can be summarized in the phenomenological Heisenberg Hamiltonian:

$$H_{Heisenberg} = -2\sum_{i<j} J_{ij} \boldsymbol{S_i} \cdot \boldsymbol{S_j} \text{ [1]}$$

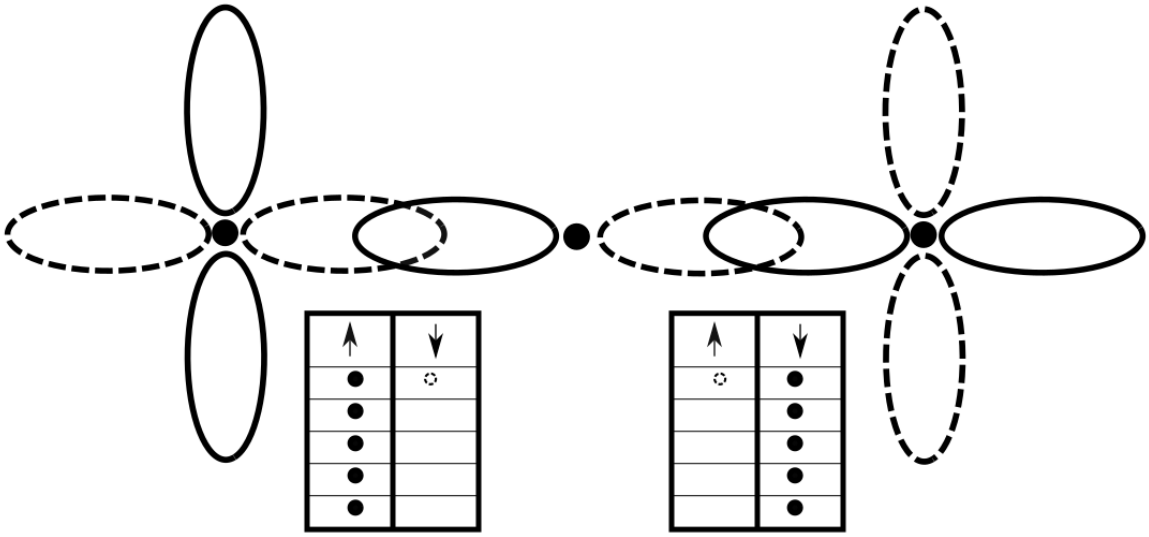

Figure 1.2: Schematic of superexchange interaction between two transition metal ions and an oxygen anion. Adapted from "Modern Magnetic Materials: Principles and Applications"[21]

where $J_{ij}<0$ stabilizes antiferromagnetic arrangements. In magnetic oxides with a variety of bond angles, ion types, and coordination types, the Goodenough-Kanamori[22] rules can be used to determine the resultant magnetic structure. In the case of ideal garnets, the tetrahedral and octahedral iron ions tend to align antiparallel to each other, and the dodecahedral rare earth ions tend to align parallel to the octahedral iron ions.

Despite its transparent physical interpretation, the Heisenberg Hamiltonian is not often used in the analysis of real materials. Instead, the molecular field theory due to Néel is preferred[23,24]. Under this formalism, the cations are considered to be sitting in a mean "molecular" field due to their neighbors. For example, in YIG, the molecular field equations are[25]:

$$M = M_d - M_a$$

$$M_a = 75.7 B_{\frac{5}{2}}\left(3.359 \times 10^{-4}\frac{1}{T}\right) H_a$$

$$M_d = 113.55 B_{\frac{5}{2}}\left(3.359 \times 10^{-4}\frac{1}{T}\right) H_d$$

$$H_a = \lambda_{aa} M_a - \lambda_{ad} M_d$$

$$H_d = -\lambda_{ad} M_a + \lambda_{dd} M_d \quad [3]$$

In these expressions, the molecular field coefficients λ_{ij} are related to the J_{ij} of the Heisenberg Hamiltonian, M is the total magnetization, M_i is the magnetization of the i sublattice, and $B_{5/2}$ is the Brillouin function for a J=5/2 particle (such as Fe^{3+}). This expression yields an M(T) curve such as that seen in Figure 1.3.

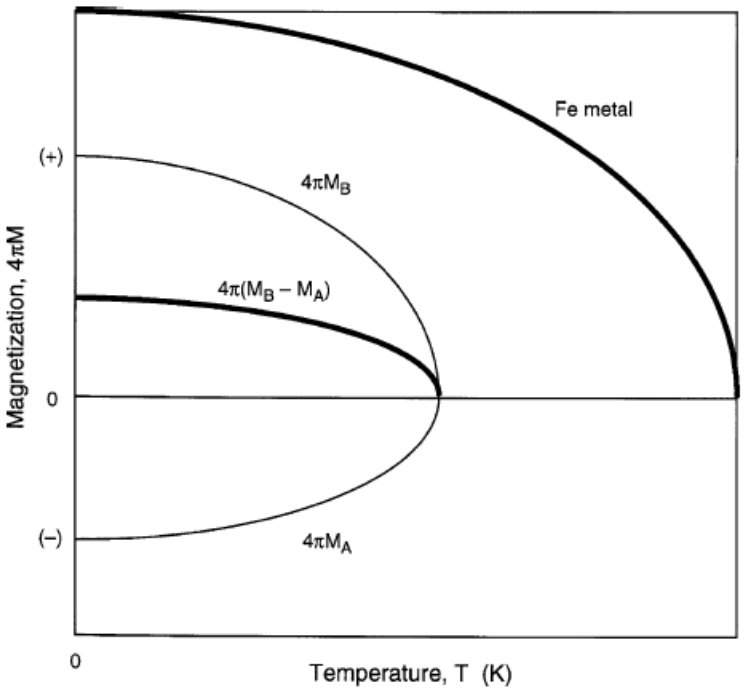

Figure 1.3: Prototypical M(T) curve for two-sublattice and one-sublattice magnetic materials. Reprinted from "Magnetic Oxides" with permission[23]

The introduction of rare-earth ions into YIG changes the character of the magnetic interactions through the introduction of an additional magnetic sublattice. This greatly complicates the thermomagnetic behavior, as now the first equation in the above set changes to:

$$M = |(M_d - M_a) - M_c| \text{[4]}$$

and an additional set of molecular field coefficients must be introduced[23]. It is important to note that the RE-RE exchange field is much smaller than the Fe-Fe and Fe-RE exchange fields due to the shielding of the RE 4f electrons[26]. In addition, the so-called rare-earth canting effect can arise, causing the rare-earth magnetization to be lower than the predicted free-ion value. This is due to a

reduction in the orbital angular momentum due to the crystal field, which is small but not negligible in rare-earth ions[23].

In some cases, the presence of rare-earth ions may give rise to a *magnetic compensation point*, a temperature at which the sublattices perfectly cancel and the net magnetization goes to zero. Magnetic compensation points are technologically interesting because they can support ultrasmall and ultrafast spin textures[27] and efficient spin orbit torque switching[28]. However, the presence and exact positions of magnetic compensation points is affected strongly by the distribution of ions between the magnetic sublattices. We will study this more closely for the case of TbIG in Chapter 4. To close our present discussion of the magnetism of rare-earth iron garnets, Figure 1.4 shows the thermomagnetic behavior of the REIG series.

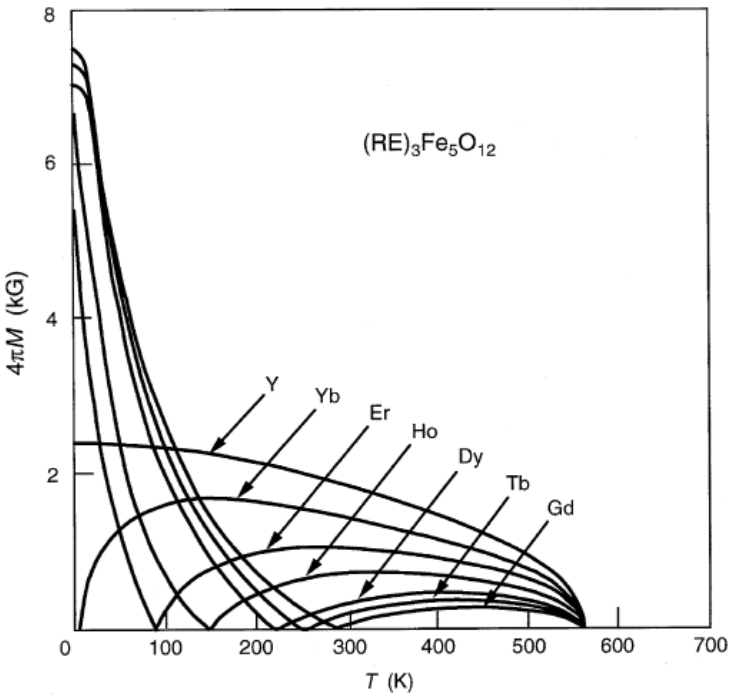

Figure 1.4: Thermomagnetism curve of the various REIG materials. Note the vanishing magnetization at the magnetic compensation problems of, e.g., TbIG and GdIG. Reprinted from "Magnetic Oxides" with permission[23].

1.4 Sources of Anisotropy in Rare-Earth Iron Garnet Thin Films

In order to achieve PMA in REIG thin films and spintronic devices, a number of different anisotropy terms must be balanced. In this section, the physical origins of each will be discussed, with special attention paid to their relevance to garnet materials in particular. Then, an equation incorporating all these anisotropies will be presented and the continuum of behaviors possible in garnets as a function of overall anisotropy will be reviewed. Finally, the various garnets which have been grown with PMA using PLD will be discussed.

1.4.1 Shape (Magnetostatic) Anisotropy

Maxwell's divergence equation for **B** is:

$$\nabla \cdot \boldsymbol{B} = \nabla \cdot (\mu_0 \boldsymbol{H} + \boldsymbol{M}) = 0 \text{ [5]}$$

Where **B** is the magnetic flux density, **H** is the magnetic field, and **M** is the magnetization. This equation can be reformulated as:

$$\nabla \cdot \boldsymbol{H} = -\nabla \cdot \frac{\boldsymbol{M}}{\mu_0} \text{ [6]}$$

Therefore, a stray field is set up at interfaces where the divergence of **M** is nonzero. The energy of this stray field – or demagnetization energy – when integrated through all space is:

$$E_{demag} = \int \frac{1}{2} \mu_0 \boldsymbol{H}^2 dV \text{ [7]}$$

In this thesis, there is a particular case of interest: thin films where there is one finite dimension (typically along the z-axis) and two infinite dimensions. In this case, the demagnetization energy is[29]:

$$K_d = \frac{M_S^2}{2\mu_0} [8]$$

This expression gives the difference in energy between the out-of-plane and in-plane magnetized situations. Even for the devices considered in this thesis, the thickness is sufficiently small compared to the device extent that this case can be applied. The demagnetization energy for a thin film always tends to pull **M** into the plane of the film, so other sources of anisotropy must be explored in order to oppose shape anisotropy and achieve PMA.

1.4.2 Magnetocrystalline Anisotropy

In contrast to shape anisotropy, magnetocrystalline anisotropy is a fundamentally quantum-mechanical phenomenon. This anisotropy has a symmetry which is controlled by the crystal structure and is thus independent of specimen shape. For a cubic crystal (such as a garnet), the anisotropy energy can be written as[30]

$$U_{mc} = K_0 + K_1(\alpha_1^2\alpha_2^2 + \alpha_2^2\alpha_3^2 + \alpha_3^2\alpha_1^2) + K_2\alpha_1^2\alpha_2^2\alpha_3^2 + \cdots [9]$$

Where α_i are the direction cosines of the magnetization with respect to the crystal axes. The dominant term (K_1) can be positive or negative[21]. If it is positive, the easy axes are <100> while they are <111> for negative K_1 (See Figure 1.5). In order to understand the origins of this anisotropy, we will first review a simple single-ion model of the anisotropy of Co^{2+} in spinels due to Slonczewski[30] and then look at applications to rare-earth garnets. The single-ion Hamiltonian is:

$$H' = 2\beta \boldsymbol{H} \cdot \boldsymbol{S} + \lambda \boldsymbol{L} \cdot \boldsymbol{S} [10]$$

where the first term represents the exchange interaction in the mean field **H** and the second term represents spin-orbit coupling.

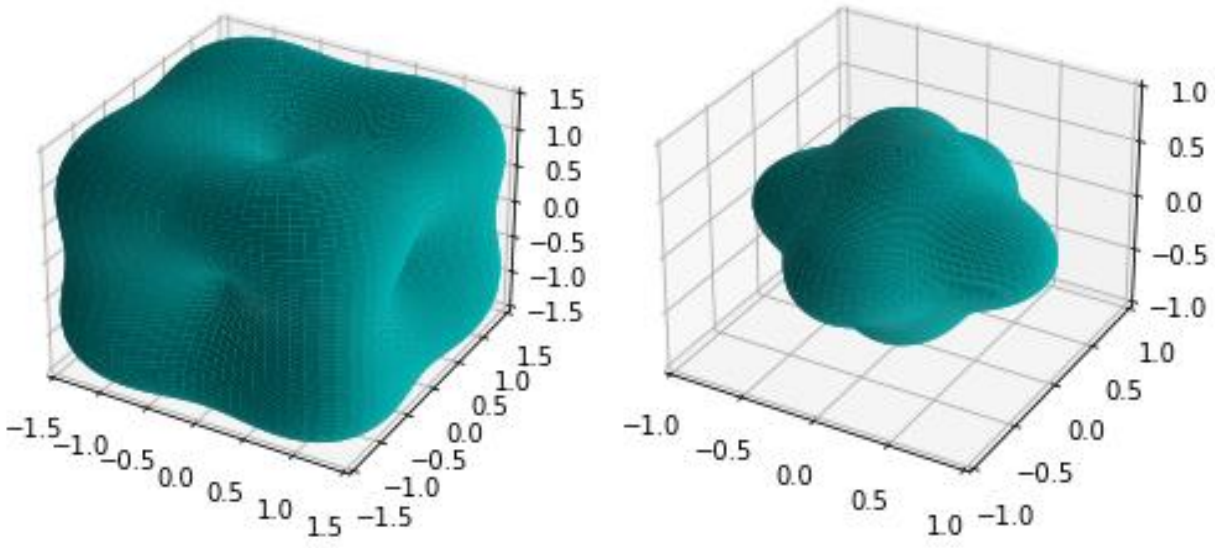

Figure 1.5: Surface plots of the cubic magnetocrystalline anisotropy energy. Left: $K_1>0$. Right: $K_1<0$

The d-orbitals of Co^{2+} (d^7) are split by the cubic crystal field of the surrounding oxygen anions into two degenerate e_g orbitals and three degenerate t_{2g} orbitals, with the e_g orbitals being the higher-energy states for octahedral sites. The next-nearest neighbor cations cause the octahedral oxygen anions to become displaced in a <111> direction, giving rise to an additional trigonal crystal field that further splits the t_{2g} orbitals into a singlet and a doublet with 0 and ±1 units of orbital angular momentum respectively[30,31]. In Co^{2+}, the electron occupation scheme (Figure 5) causes the perturbation Hamiltonian to give the energy levels:

$$\epsilon = |2\beta \boldsymbol{H} \mp \alpha\lambda \boldsymbol{k_t}| M_s, M_s = -S, \dots, S \text{ [11]}$$

where $\mathbf{k_t}$ is the trigonal axis. To calculate K_1, the eigenvalues are calculated for the 4 trigonal axis directions and then like terms are grouped and compared with equation []. The important physical phenomena at play are the crystal field (parametrized by α), the spin-orbit interaction (parametrized by λ), and the exchange interaction (parametrized by β). The preferential direction

is chosen by the second-nearest-neighbor cation field. The temperature dependence enters from the mean field **H**, which decreases with increasing temperature. In Co^{2+}-containing spinels, the most important term is $\alpha\lambda$.

Now let us turn our attention to rare-earth garnets. Ideally (although not in reality, as we will see in Chapter 4), REIG materials contain only Fe^{3+} and RE^{3+} cations. Fe^{3+} ($3d^5$) has zero orbital angular momentum in the ground state, so to first order the spin-orbit coupling term in the anisotropy expression above is zero. However, higher-order terms enter through the mixing of excited states with nonzero orbital angular momentum[23], and this gives rise to a small, but nonzero single-ion anisotropy. This is responsible for the magnetocrystalline anisotropy of YIG.

Rare-earth ions, on the other hand, have $4f^n$ electronic structures. The 4f electrons have, in general, a strong unquenched orbital angular momentum and thus strong spin-orbit coupling[23] which cause them to dominate the magnetocrystalline anisotropy of REIG materials. There is a strong correlation between the presence of unquenched angular momentum and the magnetocrystalline anisotropy[32].

1.4.3 Magnetoelastic Anisotropy

As we have seen, spin-orbit coupling can cause anisotropy in magnetic oxides by causing the spin system to "see" lattice directions through the crystal field. The implication is that, if the crystal field is distorted through strain, the anisotropy can be affected. This gives rise to another source of anisotropy known as magnetoelastic anisotropy. The phenomological form of the magnetoelastic anisotropy energy for a cubic crystal is[21]:

$$U_{me} = B_1\left[e_{xx}\left(\alpha_1^2 - \frac{1}{3}\right) + e_{yy}\left(\alpha_2^2 - \frac{1}{3}\right) + e_{zz}\left(\alpha_3^2 - \frac{1}{3}\right)\right] +$$

$$B_2\left[e_{xy}\alpha_1\alpha_2 + e_{yz}\alpha_2\alpha_3 + e_{zx}\alpha_3\alpha_1\right] [12]$$

where B_1 and B_2 are phenomenological magnetoelastic coupling constants and e_{ij} is the strain:

$$e_{ij} = \frac{1}{2}\left(\frac{\partial u_i}{\partial x_j} + \frac{\partial u_j}{\partial x_i}\right) [13]$$

In this thesis, the magnetostriction coefficients λ_{ijk} will be used instead of B_1 and B_2. For a cubic crystal, there are two independent magnetostriction coefficients, λ_{111} and λ_{100}:

$$\lambda_{100} = -\frac{\frac{2}{3}B_1}{c_{11}-c_{12}} [14]$$

$$\lambda_{111} = -\frac{\frac{1}{3}B_2}{c_{44}} [15]$$

At its core, magnetostriction in oxides is caused by the anisotropic repulsion of cation orbitals by the surrounding oxygen anions under deformation[30]. Slonczewski's single-ion anisotropy model for Co^{2+} can also explain the quantum-mechanical origins of magnetostriction[30]. As before, when embedded in an octahedral+trigonal crystal field, the triplet t_{2g} orbitals of Co^{2+} are mixed into a doublet $\psi_{\pm 1}$ with one unit of orbital angular momentum aligned along the trigonal axis and a singlet ψ_0 with no orbital angular momentum. Thus, to zero order in λ (here denoting the spin-orbit parameter) spin-orbit coupling does not cause any magnetostrictive effect and first-order degenerate perturbation theory must be used. The Hamiltonian is:

$$H = E_t(1 - l_{z'}^2) + \alpha\lambda S l_{z'} cos\theta + \alpha\lambda S l_x sin\theta + V' [16]$$

Where E_t is the trigonal field splitting of the t_{2g} orbitals, **l'** is the angular momentum operator for the octahedrally coordinated ψ orbitals, and V' is the extra crystal field potential due to strain. By

carrying out the perturbation theory calculation over the degenerate ψ manifold, an expression for $f_{rs}=df/d\varepsilon_{rs}$ (where f is the free energy of a Co^{2+} ion) can be carried out at various angles of the magnetization for a given strain potential V'. The details of this calculation need not concern us here; let it suffice to say that to first order the combined effects of spin-orbit coupling and the strain-induced crystal field potential cause an excess anisotropy through the lifting of the degeneracy of the $\psi_{\pm 1}$ states.

As before, let us turn now to the rare-earth iron garnets. Iida[33] tabulated the magnetostrictions of garnets which he divided into two groups: A(YIG, GdIG, and EuIG) and B(SmIG, TbIG, DyIG, HoIG, ErIG, TmIG, and YbIG). In general, group A had lower magnetostriction than group B. He explained this fact by considering the electronic structure of the rare-earth ions.

Y^{3+}, being a diamagnetic ion, does not contribute to the magnetostriction so the magnetostriction of YIG was entirely due to Fe^{3+} just as in the case of the magnetocrystalline anisotropy. The ground state of Eu^{3+} has J=0, but the exchange field mixes in excited states with J=1 or J=2 [34] which causes an induced magnetostriction proportional to the square of the exchange field. Gd^{3+}, an s-state ion, exhibits a small magnetostriction due to its vanishing orbital moment. However, it may have some magnetostriction due to the admixture of excited states as in EuIG[33]. The group B ions have non-zero orbital moment in their ground states, which causes a similar electrostatic interaction with the surrounding oxygen ligands as in the case of Co^{2+} treated above. As we will see in Chapters 3 and 4, the high magnetostriction of rare-earth garnet garnets can be leveraged to achieve PMA in PLD-grown TbIG and EuIG thin films.

1.4.4 Growth-Induced Anisotropy

All of the sources of anisotropy previously mentioned are relatively independent of growth kinetics. Shape anisotropy is only affected by the form factor of the sample in question, while magnetocrystalline/magnetoelastic anisotropy are only affected by the types of ions and lattice sites in the crystal. However, there is an additional source of anisotropy which is due to the kinetics of ion incorporation during growth. This growth-induced anisotropy has been extensively studied in LPE-grown garnets but has been largely ignored in PLD-grown garnets. In chapter 5, strong evidence for the existence of growth-induced anisotropy in PLD-grown garnets will be presented.

The garnet crystal structure contains several inequivalent dodecahedral lattice sites, distinguished by their nearest-neighbor tetrahedral (Td) and octahedral (Oh) sites[35]. "X" sites have Td neighbors to the left and right, "Y" sites have Td neighbors in front and behind, and "Z" sites have Td neighbors above and below. These sites can be further divided by their Oh neighbors into X_i, Y_i, Z_i (i=1,2,3,4) (see Figure 1.6).

Now, consider a growing crystal in the (111) orientation[18]. From the point of view of the incoming rare-earth ions, there are two classes of dodecahedral sites (see Figure 1.7) with different cross-sectional areas. Therefore, if a garnet crystal is grown with two differently-sized rare-earth ions, the larger ions will find a lower energy barrier to become incorporated into one class of sites. This preferential occupation will break the crystal symmetry and give rise to an additional anisotropy term, as we will now show.

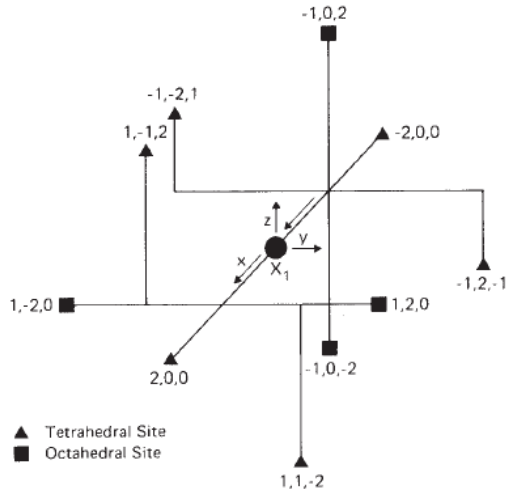

Figure 1.6: One example of a dodecahedral site in a REIG (in this case, an X_1 site), denoted by its spatial relationship to neighboring tetrahedral and octahedral sites. Reprinted from "Magnetic Bubble Technology" with permission[18]

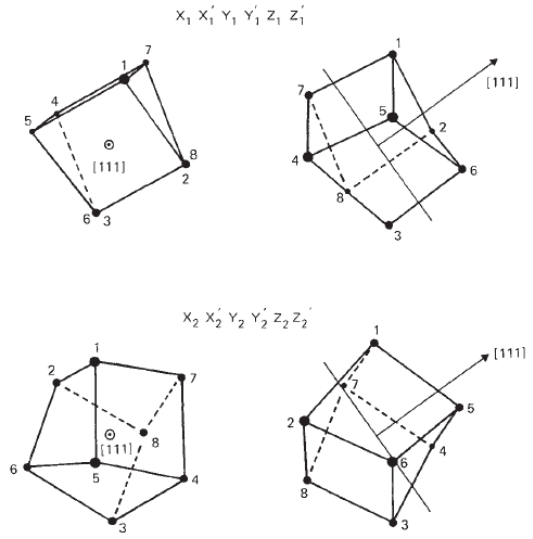

Figure 1.7: Different views of the various inequivalent dodecahedral sites in a (111)-oriented garnet thin film. The sites can be divided into two different classes. Reprinted from "Magnetic Bubble Technology" with permission[18]

Phenomenologically, anisotropy can be expressed as an effective dipole interaction between an ion and its nearest neighbors[36]. With this approach, the single-ion anisotropy due to a rare-earth ion can be written as[35,36]:

$$\sum_i \cos^2 \theta_i = (\boldsymbol{\alpha} \cdot \boldsymbol{r_i})^2 \text{ [17]}$$

where $\mathbf{r_i}$ is the unit vector from the rare-earth site to its i^{th} neighbor and $\boldsymbol{\alpha}$ is the magnetization unit vector. If the X_1-type sites are all filled, evaluating this expression leads to[18]:

$$\sum_i \cos^2 \theta_i = 4a - 2b(\alpha_1\alpha_2 + \alpha_2\alpha_3 + \alpha_3\alpha_1) \text{ [18]}$$

where a and b are constants dependent on nearest-neighbor bond lengths. Meanwhile, if all the X_2-type sites are filled, the excess anisotropy becomes:

$$\sum_i \cos^2 \theta_i = 4a + 2b(\alpha_1\alpha_2 + \alpha_2\alpha_3 + \alpha_3\alpha_1) \text{ [19]}$$

Therefore, preferential occupation of either X_1 or X_2 sites can lead to either an enhancement or a reduction in the uniaxial anisotropy constant K_u.

The effects of different pairs of ions and stoichiometries have been extensively studied in LPE-grown garnet thin films. For (111) garnets, the growth-induced anisotropy can be expressed as[18]:

$$E_K^G = \frac{A+B}{3} - \frac{B}{2}\sin^2\theta = K_0 + K_u^G \sin^2\theta \text{ [20]}$$

K_u^G has been found to vary quadratically with the dodecahedral-site stoichiometry, $K_u^G = K_{ij}x_ix_j$. Here, K_{ij} is a constant proportional to the ion size difference between ion i and ion j (for instance, in Chapter 5, i can be taken to be Y^{3+} and j can be taken to be Tm^{3+}). A size difference of more than 0.05Å was found to be necessary for growth-induced anisotropy to appear[37].

The kinetic nature of the phenomenon was confirmed through temperature-dependent growth and annealing experiments. In $Y_{2.6}Sm_{0.4}Ga_{1.2}Fe_{3.8}O_{12}$, the growth-induced anisotropy was found to decay linearly with annealing time[38]. This was taken to mean that the cation ordering is "frozen-in" during growth but does not represent an energetically favorable state. In $Eu_{2.5}Ca_{0.5}Si_{0.5}Fe_{4.5}$, films grown at 940˚C exhibited no growth-induced anisotropy while films grown at 835˚C had a nonzero K_u^G which decreased with annealing, lending more credence to this hypothesis[39].

All of the data mentioned in this section so far is on LPE-grown garnet crystals. To date, there have not been many investigations of growth-induced anisotropy in PLD-grown garnets. In 2009, Manuilov *et al*. found convincing evidence of growth-induced anisotropy in YIG due to ordering of iron vacancies in Fe-deficient PLD-grown YIG[40]. In the supplementary information of Soumah *et al*.'s (2018) paper on Bi:YIG with PMA, the authors report an additional source of anisotropy (i.e. non-magnetoelastic) which they ascribe to growth-induced anisotropy[41]. This is plausible because K_{ij} when $i=Bi^{3+}$ and $j=Y^{3+}$ in LPE-grown films is likely very large[18] and growth-induced anisotropy in LPE-grown Bi:YIG films has been previously reported in the literature[42]. However, at the time of writing, other reports of growth-induced anisotropy in PLD-grown garnets are sparse or nonexistent.

1.4.5 Overall Uniaxial Anisotropy and Magnetic Domains

In this section, we have explored the various sources of anisotropy operating in epitaxial garnet thin films. Some of these (shape, magnetocrystalline, magnetoelastic) are due to fundamental materials properties and interactions such as magnetostatic energy and spin-orbit coupling. Others (growth-induced) are due to effects induced by the growth mode of the garnet films. Equations incorporating all of these interactions which will be used in later chapters can be written as[43]:

$$K^{111} = \frac{K_1}{12} + \frac{9}{4}\lambda_{111}c_{44}\left(\frac{\pi}{2} - \beta\right) - \left(\frac{\mu_0}{2}\right)M_S^2 + K_G \text{ [21]}$$

$$K^{001} = \frac{3}{2}\lambda_{001}(c_{11} - c_{12})(\epsilon_{zz} - \epsilon_{xx}) - \left(\frac{\mu_0}{2}\right)M_S^2 + K_G \text{ [22]}$$

The first expression is for films grown in the (111) orientation and the second expression is for films grown in the (001) orientation. Here, K is an effective uniaxial anisotropy constant. Generally, if K is positive, the film will have PMA; if K is negative, the film will have in-plane anisotropy. All of the variables have been previously defined in this section except for β, the apex angle of the unit cell (a stand-in for shear strain). Growth-induced anisotropy K_G is included for cases where growth-induced ordering is active (e.g. mixed garnets such as the $Y_xTm_{3-x}Fe_5O_{12}$ studied in Chapter 4). The next natural question is: what behaviors can we predict for garnet films as a function of K? A wide variety of analytical and experimental studies have shown that saying "K positive (negative) means that the magnetization lies out of (in) the plane" is an oversimplification. The different cases can be classified by introducing the quality factor ratio Q[29]:

$$Q = \frac{K_u}{2\pi M_S^2} \text{ [23]}$$

This dimensionless quantity can be used to compare the relative importance of the shape and uniaxial anisotropies. K_u, the effective uniaxial anisotropy constant, is the sum of all anisotropies except for shape anisotropy.

Case 1 – $K_u>0$, $Q<1$: In this case, the film supports an in-plane magnetization as mentioned earlier. However, above a critical thickness D_{cr}, stripe domains can form to minimize the anisotropy energy as a pure in-plane magnetization would maximize the energy due to K_u[29]. These so-called "weak stripe domains", which were originally theorized by Muller in 1961[44] by linearizing the zero-torque condition $\boldsymbol{M} \times \boldsymbol{H_{eff}} = 0$, have a short period on the order of the film thickness at zero

field. If in-plane fields are applied, the in-plane state is stabilized with respect to the stripe domains at a given thickness[29]. This case, while interesting due to the small magnetic textures it produces, is not very relevant to this thesis because most of the films considered in later chapter have Q>1. In Figure 1.8, micromagnetic simulations of films with weak stripe domains are presented.

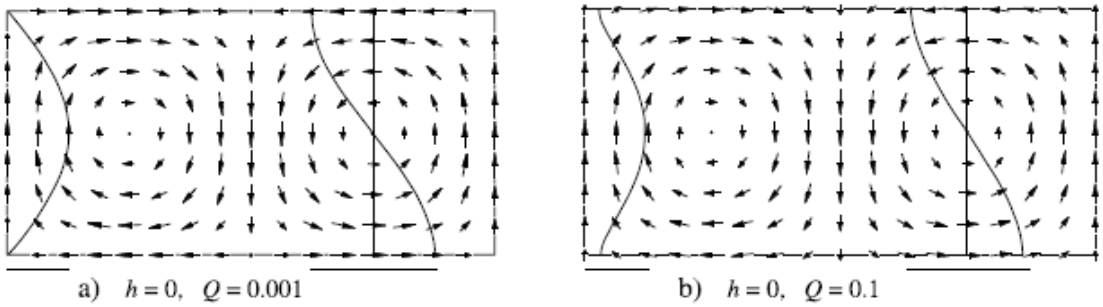

Figure 1.8: Calculated zero-field equilibrium weak stripe domain patterns for various values of Q<1. Partially reproduced from "Magnetic Domains: The Analysis of Magnetic Microstructures"[29]

Case 2 – K_u>0, Q>1: In this case, the film supports a perpendicular magnetization. However, depending on the exact balance of energies in the film, a uniform magnetization texture, stripe domains, or bubbles may be present. This problem was originally solved in its full form by Kooy and Enz in 1960 while looking at barium hexaferrite platelets[45], although a more primitive model was previously solved by Kittel[46]. By using Fourier analysis (assuming a square wave magnetization structure) coupled with a magnetostatic perturbation theory known as the μ*-method[29], Kooy and Enz calculated that the demagnetization energy of a stripe domain array in a PMA thin film is:

$$E_d = K_d \left\{ \frac{Dm^2}{1+\frac{1}{Q}} + \left(\frac{8P}{\pi^3}\right) \sum_{n=1}^{\infty} n^{-3} \sin^2\left[\frac{1}{2}\pi n(1+m)\right] \frac{\sinh(\pi n g)}{\sinh(\pi n g) + \sqrt{1+\frac{1}{Q}}\cosh(\pi n g)} \right\} \quad [24]$$

In this expression, $P = W_1+W_2$ where $W_{1,2}$ are stripe domain widths, D is film thickness and m is the reduced magnetization $(W_1-W_2)/(W_1+W_2)$. By minimizing the total energy (demagnetization, exchange, anisotropy) in the film, quantities such as domain size can be calculated. Various limiting cases have been extracted from this equation; the one that is of most interest to us is due to Kaplan and Gerhing[47], who produced an approximation to the Kooy-Enz theory for the case where the film thickness is much less than the domain size. We will return to this topic in Chapter 5. The main difference between this case and the previously-discussed weak stripe domain case is that a definite critical thickness does not exist – "it can be shown that infinite plates get single domain only for vanishing values of the thickness"[45]. If the domain wall width is explicitly taken into account, this ultrathin film behavior can be modeled. Skomski *et al*. modeled ultrathin films and showed that as thickness increases the reversal mechanism of thin ferromagnetic plates changes from incoherent reversal to domain propagation[48]. Lemesh *et al*. fully modeled the equilibrium domain morphology in ultrathin films and found that as the thickness decreases the equilibrium domain width quickly diverges, meaning that a finite sample can become single-domain[49]. It is also important to keep in mind that, even in a film that can support stripe domains, nucleation barriers and domain wall coercivity may keep the domains from appearing at zero field, giving rise to a nonzero remanence[29].

1.4.6 Dzyaloshinskii Interaction (DMI) and Chiral Domain Walls in REIG Materials

With the introduction of domains, it is natural to ask what kinds of domain walls (boundaries between uniform domains) exist in REIG thin films. The classical theory of domains (considering only those energy terms which have been previously mentioned in this chapter) predicts two types of domain walls in PMA thin films: Bloch walls and Néel walls. These walls are defined by the sense of magnetization rotation with respect to the domain wall normal (see Figure 1.9).

Figure 1.9: Micromagnetic simulations of Néel (top) and Bloch (bottom) domain walls in a magnetic strip. The simulations parameters are the same as those used in Thiaville *et al*.[50]

If only the aforementioned energy terms are taken into account, the crossover from Bloch to Néel occurs due to magnetostatic interactions. For instance, in unpatterned thin films, Bloch walls are the lowest energy state because they contain no free poles[50]. If the film is patterned into strips, free poles (and thus shape anisotropy) arise in the domain wall core, causing Néel walls to be preferred[50].

However, another interaction, known as the Dzyaloshinkii-Moriya interaction (DMI) can serve to stabilize Néel walls even in unpatterned films. The DMI is an exchange interaction that causes alignment of adjacent spins, but unlike the superexchange interaction considered earlier, it has the functional form:

$$E_{DMI} = \sum_{i,j} \boldsymbol{d_{ij}} \cdot (\boldsymbol{S_i} \times \boldsymbol{S_j}) \text{[25]}$$

Where $\mathbf{d}_{ij}$. The DMI vector, is perpendicular to **z** and to the bond between sites i and j[51]. Micromagnetic calculations[50] show that the presence of a cross product in this expression tends to stabilize a single chirality of Néel walls in unpatterned films. Figure 1.10 reproduces the DMI-induced crossover from Bloch to Néel walls in a magnetic thin film. It is important to note that the ingredients of the DMI in thin films are inversion symmetry breaking (such as at an interface) and spin-orbit coupling[51]

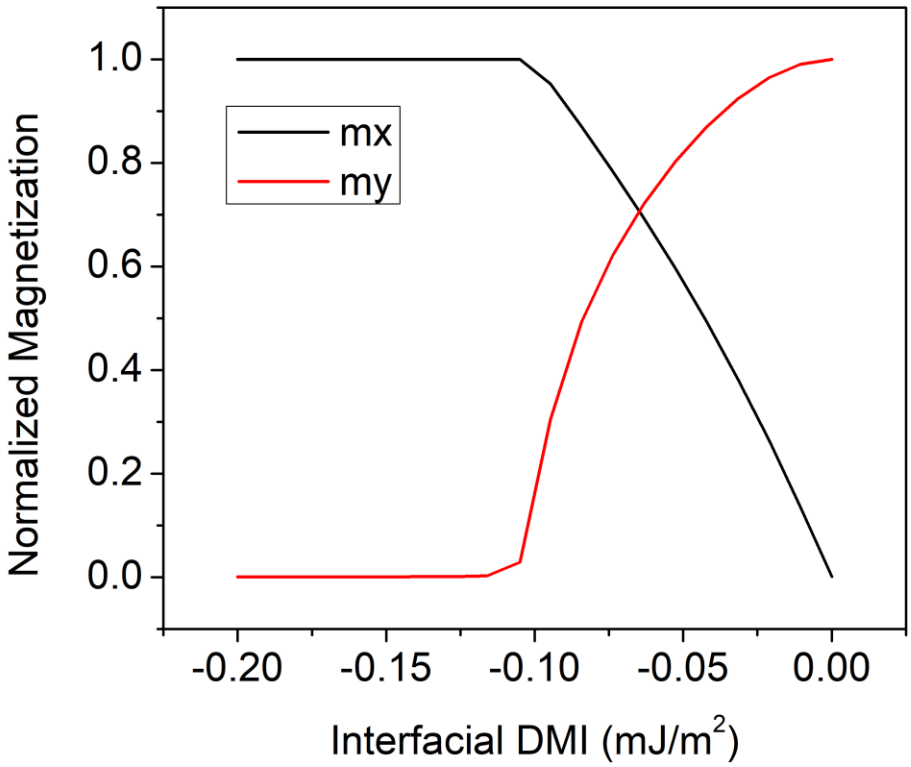

Figure 1.10: Micromagnetic simulation of the x and y components of the domain wall core magnetization as a function of DMI strength. The domain wall normal points in the x direction. The simulation parameters were the same as those used in Thiaville *et al.*[50] For large negative DMI values, the magnetization is aligned with the domain wall normal (Néel wall). As the absolute value of the DMI strength decreases, the magnetization gradually rotates towards the y direction (Bloch wall)

Since the discovery of the DMI in thin films, it has mainly been studied in metallic heterostructures such as Co/Pt which show inversion symmetry breaking and spin-orbit coupling (in this case, in the heavy metal Pt). However, recently the DMI has been discovered to exist in REIG thin films as well. The exact origin of the interaction is still a matter of debate, but as we will see in Chapter 6 the DMI-induced presence of homochiral Néel walls in garnets enables record-breaking domain wall velocities.

1.4.7 Summary and Outlook: Perpendicular Magnetic Anisotropy in Rare-Earth Iron Garnets

The large magnetostriction of certain rare-earth ions – coupled with the correct sign of substrate mismatch – has been leveraged to achieve PMA in rare-earth iron garnet films. The first report was in thulium iron garnet (TmIG) by Kubota *et al.* in 2012[52], which was grown with PMA in a tensile strain state on GGG. After this, a variety of rare-earth iron garnets with PMA have been grown and used in spintronic studies. In this section, an overview of the various REIG materials currently under investigation by the spintronics community will be provided. Spintronic studies will be mentioned in passing, but more detail will be provided later in this chapter.

- TmIG – After the first report of PMA TmIG by Kubota *et al*., this material has become the standard workhorse for spintronic studies in garnet thin films. In 2015, our group successfully grew PMA TmIG on GGG[53] and successfully switched Pt/TmIG/GGG heterostructures with spin-orbit torques (SOT)[10], the first report of SOT switching in a magnetic insulator. Since then, fast switching[14], ultrafast domain wall motion[11,13], and homochiral Néel walls due to the Dzyaloshinskii-Moriya interaction (DMI)[11,13,16,54] have been observed in Pt/TmIG/GGG heterostructures. Magnetic bubbles have also been

imaged by our group in TmIG, although the film was too thick to support homochiral textures[55]. High-quality TmIG has also been grown via off-axis sputtering[56]

- YIG – Under most circumstances, pure YIG cannot be grown with PMA due to its low magnetostriction coefficient. However, by using a paramagnetic buffer later of SmGG to suppress strain relaxation, Fu *et al.* successfully grew YIG with PMA on SGGG[57] (although no damping results were reported). More recently, Ding *et al*. reported the growth of YIG on GSGG with no buffer layer[58]. These YIG films exhibited a damping as low as 4.2E-4, which is about two orders of magnitude lower than previously reported values for EuIG and TmIG[58].
- Bi:YIG – First reported in 2012 by Popova *et al*[59], this material exhibited PMA on (001) GGG for thicknesses below two unit cells. In 2018, Soumah *et al*[41] reported PMA of films up to 50nm when grown in tension on (111) sGGG. Bi:YIG is exceptionally interesting for spin wave studies because of its low damping, which is comparable with the damping of YIG[41]. Since then, our group[12] has reported relativistic dynamics of domain walls in Pt/Bi:YIG/GSGG thin film heterostructures. Bi:YIG with low damping has also been grown with PMA on SGGG by RF sputtering[60].
- TbIG – TbIG can be grown with PMA on (111) GGG (i.e. in a compressive state) due to its large positive λ_{111}[43]. Similar to TmIG, homochiral Néel walls have been found in thin Pt/TbIG/GGG heterostructures[13], and spin transport across the Pt/TbIG interface has been explored[43]. However, it is mainly interesting due to its near-room-temperature compensation point. Bulk terbium iron garnet has a compensation temperature of ~260K while TbIG grown by our group has a compensation temperature of ~330K[43]. In Chapter 4 we will explore this phenomenon through Hartree-Fock analysis of XMCD data.

- EuIG – EuIG is interesting in that it can be grown with PMA on both (111) and (001) GGG due to its large positive λ_{111} and λ_{001}[32,43]. Spin transport across Pt/EuIG/GGG(111,001) interfaces have been explored and found to be similar[43]. Due to both of its magnetostriction coefficients being large and positive, polycrystalline EuIG can also be grown with PMA on Z-cut quartz due to strain induced by thermal mismatch, and Pt/EuIG/ZQ was found to exhibit similar transport properties as single-crystalline Pt/EuIG/GGG[61].
- DyIG – DyIG is similar to EuIG in that both its λ_{111} and its λ_{001} have the same sign[32]. However, it cannot be grown on GGG with PMA due to the strain state being incorrect[62]. DyIG has been grown by our group with PMA on GSGG (epitaxy), SGGG (epitaxy), and Si (polycrystalline)[62], which is promising for future integrated spintronics applications.

1.5 Spintronic Phenomena in Rare-Earth Iron Garnets

Thus far in this chapter, we have explored the structure and static magnetic properties of REIG thin films. Now we will discuss the dynamic properties of REIG materials studied in recent spintronic experiments. The equation describing the motion of a magnetic moment is known as the Landau-Lifshitz-Gilbert (LLG) equation. It can be written as follows[63]:

$$\frac{\partial \boldsymbol{m}}{\partial t} = \gamma_{LL}\left(\frac{1}{1+\alpha^2}\right)\left(\boldsymbol{m} \times \boldsymbol{B_{eff}} + \alpha \boldsymbol{m} \times \boldsymbol{m} \times \boldsymbol{B_{eff}}\right) \text{[26]}$$

In this equation, γ_{LL} is the gyromagnetic ratio (the ratio between the magnetic moment and the angular momentum) and α is the Gilbert damping (a dissipative term taking into account effects such as spin-orbit coupling. $\mathbf{B_{eff}}$ contains the sum of all effective fields in the system, including anisotropy, exchange, and applied fields (which we have covered). A good way to visualize the LLG equation is through so-called macrospin simulations, where a single spin is allowed to move in an applied effective field. Figure 1.11 shows the trajectory of a spin with uniaxial anisotropy

undergoing reversal in an applied field (produced by a custom LLG solver written in Matlab). Spintronics enters the picture when we start to consider other sources for the effective field that can operate within devices. One that will interest us in later chapters is known as the spin-orbit torque (SOT). Understanding it will require some understanding on spin currents in solids.

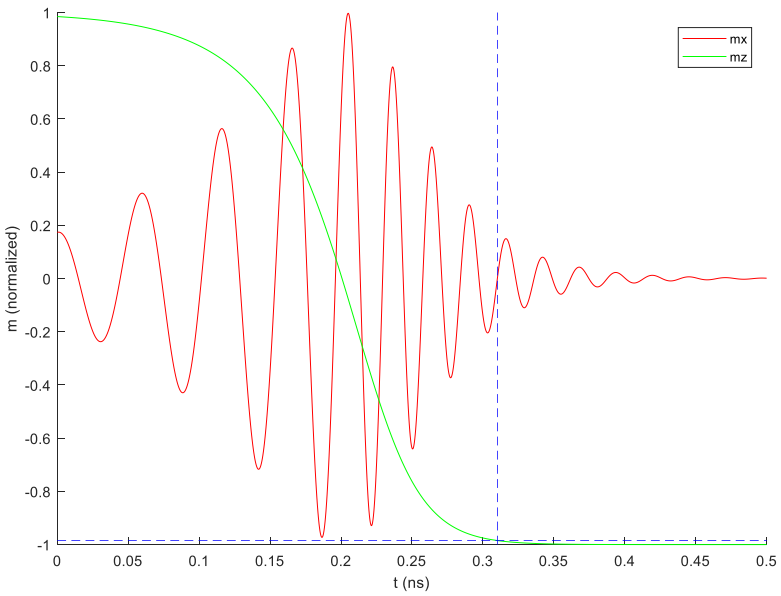

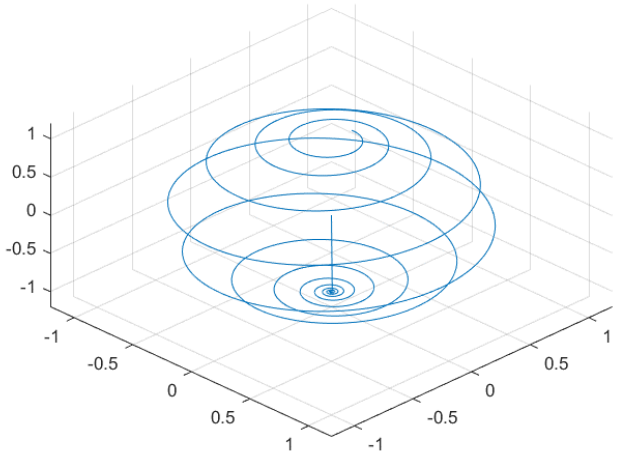

Figure 1.11: Macrospin simulation of field-induced switching (see Appendix A for details). Parameters used: M_s = 1000kA/m, α=0.1, H_K=0.4T. The external field was 1T. In (top), the blue dotted line is the predicted switching time from an analytical model due to Mallinson[64]. (bottom) shows the trajectory taken by the macrospin in 3D.

1.5.1 Description of Spin Current: Drift-Diffusion Model

In addition to charge (a scalar quantity), electrons possess spin angular momentum (a spinor quantity whose expectation value is a vector). Therefore, moving electrons can carry spin current as well as charge current. Understanding these two types of currents are necessary for understanding the phenomena related to SOT.

Unlike charge current, spin current is a 2nd-order tensor property, defined as the expectation value of the quantum-mechanical spin current operator. For an ensemble of spins, this operator is written as[65]:

$$\overleftrightarrow{J_s}(\boldsymbol{r}) = \sum_{i,\sigma,\sigma'} Re[< \psi^*_{i\sigma} | \boldsymbol{S}_{\sigma,\sigma'} \otimes \boldsymbol{v} | \psi_{i\sigma'} >[27]$$

This expression makes intuitive sense due to the fact that both the direction of the electrons' motion and the expectation value of the direction of their spin are vector quantities. Therefore, this expression allows us to describe the ith component of spin angular momentum moving in the j-direction.

However, this purely quantum-mechanical formalism is unwieldly to use. A more user-friendly one is the drift-diffusion formalism developed by Valet and Fert to describe giant magnetoresistance[66]. Under this formalism, two coupled currents – the spin and the charge current – are described by drift-diffusion equations which are governed by chemical potentials for both charge and spin accumulation. The charge and spin accumulations obey:

$$\nabla^2 \mu_{s,i} = \frac{\mu_{s,i}}{\lambda^2}$$

$$\nabla^2 \mu_c = 0 \text{ [28]}$$

where $\mu_{s,i}$ is the ith component of the spin chemical potential vector (that is, the chemical potential of the i^{ith} spin component) and λ is the spin diffusion length $\sqrt{D\tau_{sf}}$, which is the characteristic length over which a spin accumulation decays to zero in the nonmagnetic metal[65]. D is a spin diffusion coefficient and τ_{sf} is the spin-flip scattering time – the time that it takes for a spin in a given spin state to scatter to another spin state[65]. Then, the corresponding currents in a material with a conductivity of σ are described by[67]:

$$\boldsymbol{j_c} = -\frac{\sigma}{e}\nabla\mu_c$$

$$\boldsymbol{j}_{s,i} = -\frac{\sigma}{2e}\nabla\mu_{s,i} \text{ [29]}$$

As we will see later, the spin Hall effect in certain metals couples spin and charge currents. This phenomenon can by represented in matrix form as:

$$\begin{pmatrix} \boldsymbol{j_c} \\ \boldsymbol{j_{s,x}} \\ \boldsymbol{j_{s,y}} \\ \boldsymbol{j_{s,z}} \end{pmatrix} = \sigma \begin{pmatrix} 1 & \theta_{SHE}\hat{x}\times & \theta_{SHE}\hat{y}\times & \theta_{SHE}z\times \\ \theta_{SHE}\hat{x}\times & 1 & 0 & 0 \\ \theta_{SHE}\hat{y}\times & 0 & 1 & 0 \\ \theta_{SHE}\hat{z}\times & 0 & 0 & 1 \end{pmatrix} \begin{pmatrix} -\nabla\mu_c/e \\ -\nabla\mu_{s,x}/2e \\ -\nabla\mu_{s,y}/2e \\ -\nabla\mu_{s,z}/2e \end{pmatrix} \text{ [30]}$$

where θ_{SHE} is the spin Hall angle (defined in the next section)[67]. This equation summarizes charge currents due to charge accumulation and pure spin currents (inverse spin Hall effect) as well as spin currents due to spin accumulation and pure charge currents (spin Hall effect). This is useful to explain one of the possible origins of SOT[68,69] as well as measurement techniques such as spin Hall magnetoresistance[67].

In bilayers composed of ferromagnetic insulators and nonmagnetic metals, charge currents can only flow parallel to the FMI film. However, spin currents can still flow through the structure in the transverse direction. In order to describe this current flow, it is necessary to consider what is taking place at the interface between the metal and the insulator. To do this, we appeal to magnetoelectronic circuit theory.

Magnetoelectronic circuit theory is a formalism developed by Brataas in order to describe spin transfer between magnetic and nonmagnetic layers[70]. Originally, it was based on Boltzmann transport theory, but this is unnecessary to understand its phenomenological consequences. According to magnetoelectronic circuit theory, the spin current through a NM/FMI interface is composed of two components[67]:

$$e\boldsymbol{j}_{\boldsymbol{s}}^{(\boldsymbol{N}|\boldsymbol{F})}(\hat{\boldsymbol{m}}) = -G_r\hat{m} \times \hat{m} \times \boldsymbol{\mu_s} - G_i(\hat{m} \times \boldsymbol{\mu_s}) \text{ [31]}$$

In this equation, G_r and G_i are the real and imaginary parts of a magnetoelectronic circuit theory parameter known as spin mixing conductance $G_{\uparrow\downarrow}$. They describe the passage of spin currents that are transverse to the magnetization of the FMI layer[65,67]. The various symmetries of spin currents are summarized in Figure 1.12. The spin mixing conductance will be used in Chapter 3 to characterize the quality of a garnet-Pt interface as a function of crystallographic orientation and RE ion.

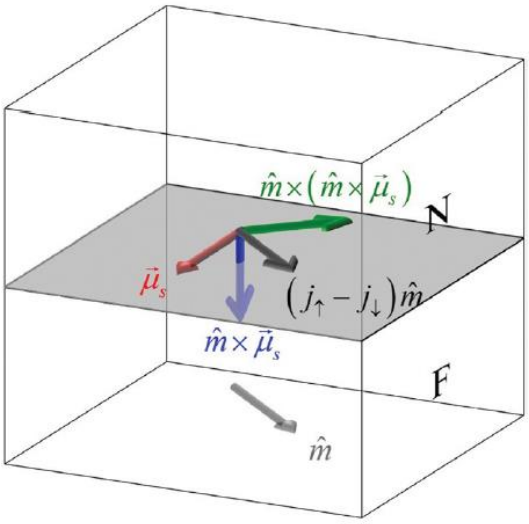

Figure 1.12: Schematic of the various spin currents present at the interface between a ferromagnet (F) and a nonmagnet (N). The component parallel to the magnetization vanishes for FMI layers. The two other (transverse) components are controlled by $G_{\uparrow\downarrow}$. Reprinted with permission from Chen *et al.* (2016)[67].

1.5.2 Spin Orbit Torque

Once we have a transverse spin current in a Pt/REIG heterostructure, we can use it to exert effective fields (and thus torques) on the magnetization which are captured in the LLG equation. There are two torque symmetries, corresponding to the two components of the spin mixing conductance. Phenomenologically, these torques can be written as:

$$\boldsymbol{\tau_{DL}} \propto \boldsymbol{m} \times (\boldsymbol{\sigma} \times \boldsymbol{m})$$

$$\boldsymbol{\tau_{FL}} \propto \boldsymbol{\sigma} \times \boldsymbol{m}$$ [32]

where "DL" and "FL" refer to damping-like (related to G_r) and field-like (related to G_i), respectively[10]. In a macrospin picture, these torques can cause magnetization switching if the torque is large enough and an in-plane field is applied along the current direction. The in-plane

field is required to break the symmetry of clockwise versus counterclockwise rotation of the magnetization vector, which stabilizes a single final state (up or down)[69]. A macrospin approximation of the critical switching current is[71]:

$$J_{critical} = \frac{2e}{\hbar}\frac{M_s t_F}{\theta_{SH}}\left(\frac{H_{K,eff}}{2} - \frac{H_x}{\sqrt{2}}\right) \text{ [33]}$$

where M_s and t_F are the saturation moment and thickness of the magnetic layer and θ_{SH} is the spin-Hall angle introduced earlier. $H_{K,eff}$ is the anisotropy field including shape anisotropy and H_x is the applied in-plane field. A visualization of the macrospin SOT switching process above and below the critical switching current is provided in Figure 1.13, using the same macrospin simulation code introduced earlier.

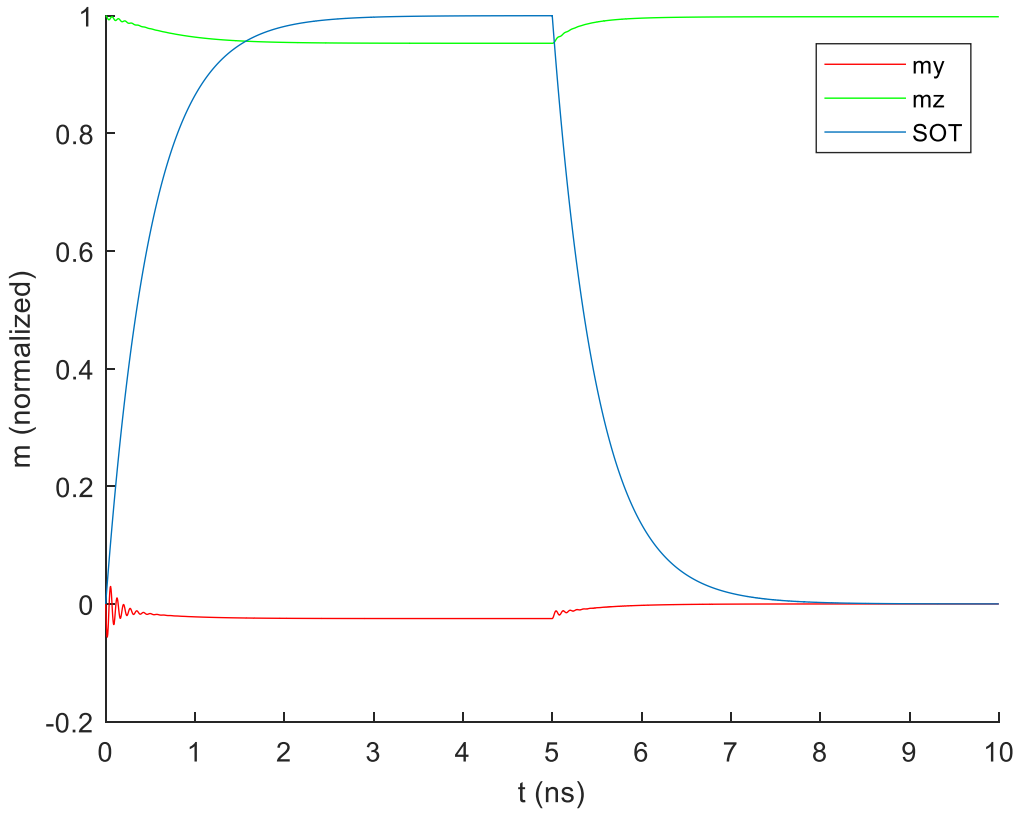

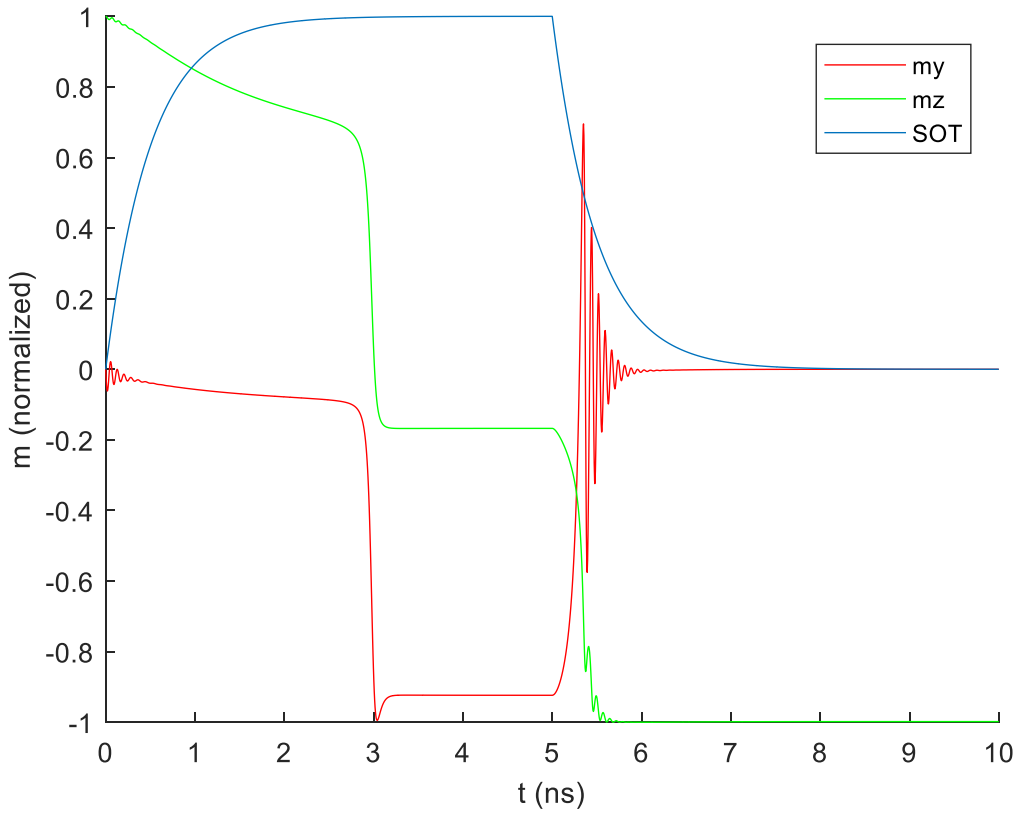

Figure 1.13: Macrospin simulation of SOT switching with and without an applied in-plane field. The parameters used were M_s = 1000kA/m, α = 0.1, H_K=0.5T, I=-100 microamps (maximum), θ_{SH}=0.3. The geometry was the same as used in Lee *et al.*[71] (a) shows the situation without an in-plane field: even though the current density is above the threshold for switching, the symmetry does not allow switching to occur. (b) shows the situation with an in-plane field of 300 Oe along the current direction – the breaking of the rotational symmetry allows switching to occur even though the current density has not changed.

The macrospin picture, while qualitatively useful, does not capture all of the physics included in the SOT switching of real devices. For this, a micromagnetic picture is required, where a magnetic device is discretized and finite-difference methods are used to solve for the time evolution of spatial quantities such as the magnetization (see, for example, the paper introducing Mumax3[63]).

If this is done, it becomes apparent that DMI and domain wall chirality is important for spin-orbit torque switching[72]. The current-induced SOT introduces a tilting of the magnetization at the devices edges which is symmetric on both sides unless an in-plane field is applied to break this symmetry. Thus, the combination of DMI and an applied in-plane field work to stabilize a single chirality of domain wall on one side of the device. Switching proceeds by domain wall propagation induced by the SOT.

SOT has been studied extensively in PMA REIG/Pt heterostructures in recent years. In 2016, the damping-like SOT was used to induce coherent auto-oscillations in YIG microdiscs[73]. SOT-assisted switching was also reported in Pt/$BaFe_{12}O_{19}$ heterostructures in 2016 and, in the same year, the first all-electrical SOT switching of TmIG/Pt was reported by our group[10]. Following this, improvements were made to the efficiency of the SOT switching through advances in PLD growth[14], and switching has been reported in TmIG films up to 15nm thick[74]. Interestingly, discrepancies in the ratio between the field-like and damping-like torques in Pt/TmIG have suggested that other effects such as Rashba spin-orbit coupling may be operating at the interface[75]. Most recently, evidence of very fast-moving DMI-induced homochiral Néel walls has been found in HM/REIG heterostructures[11–13,15]. In Chapter 6, a number of recent spintronics studies (SOT switching and domain wall motion) that the author has contributed to will be reviewed.

Chapter 2: Methods

2.1 Vibrating Sample Magnetometry

The main magnetic characterization tool used in this thesis was vibrating sample magnetometry (VSM), developed in 1956 at Lincoln Laboratory[76]. A schematic of a VSM system is depicted in figure 2.1. In VSM measurements, a magnetic sample is suspended between two pickup coils and is vibrated rapidly. The changing flux through the pickup coils induces an AC voltage (Faraday's law) which is detected by a lock-in amplifier within the VSM system. Electromagnet coils are present to apply magnetic fields to the sample so that M(H) hysteresis loops can be acquired. An oven is also available so that M(T) measurements can be carried out.

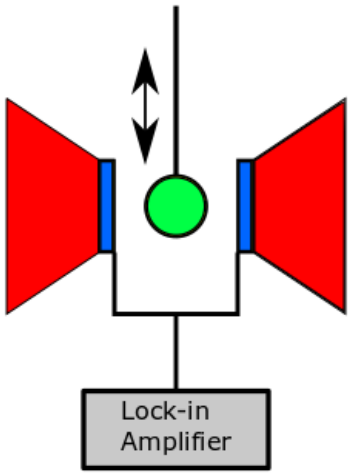

Figure 2.1: Schematic of a VSM system. The sample (green) is vibrated between pickup coils (blue) which are fed into a lock-in amplifier. The electromagnet poles (red) provide a magnetic field for hysteresis loops.

In this thesis, a DMS 880A VSM was used. Prior to each set of measurements, a calibration was carried out with a Ni disc. The pickup coil gain, sample position, and gaussmeter calibrations were

carried out in the software. During the measurements, thin film samples were mounted with nonmagnetic tape to a nonmagnetic Pyrex “lollipop” sample holder. In order to minimize drift due to thermal fluctuations during measurements, the number of points per measurement was kept below 80 (measurement times below 20 minutes).

The main sources of uncertainty in VSM measurements are the determination of sample volume (needed to normalize the measured moment and obtain the saturation magnetization) and the background subtraction. In the experience of the author, a good estimate for the sample volume for a thin film can be obtained by measuring the film area under a microscope and fitting X-Ray Reflectivity (XRR, see below) data to calculate the thickness. The background subtraction, however, provides more of a problem for films grown on GGG. For relatively low fields (below ~100 mT), the GGG background is highly linear and can be easily subtracted. However, for fields higher than 100 mT, the GGG background becomes nonlinear and easily swamps the small film signal. This problem has been observed in the literature and has been solved by, for example, thinning the substrate through polishing[77]. In the appendix to chapter 3, we address this issue in terbium iron garnet and in chapter 4 we sidestep it by using ferromagnetic resonance instead of VSM to determine anisotropy fields. See figure 2.2 for examples of raw and processed VSM data.

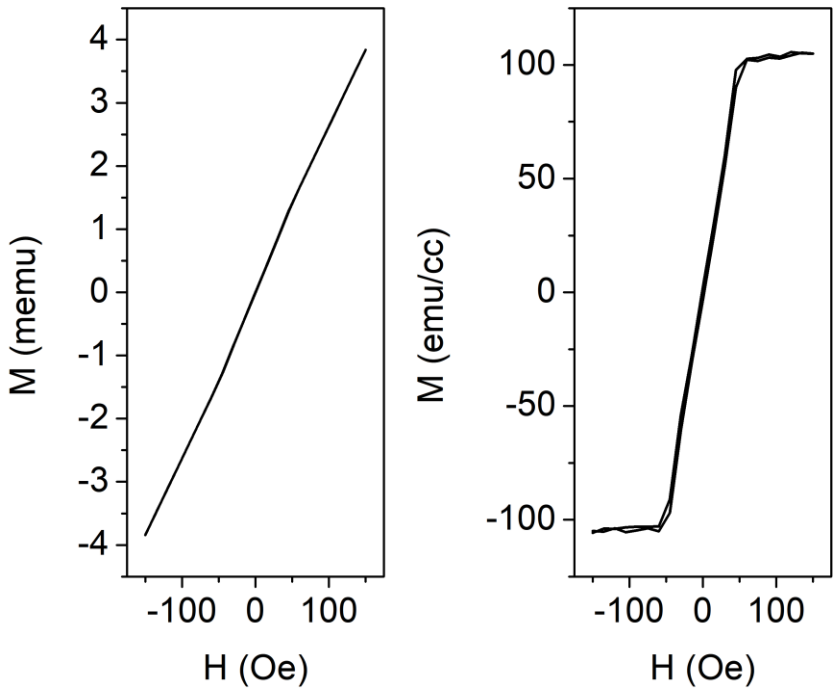

Figure 2.2: Unprocessed (left) and processed (right) VSM data from a $Y_xTm_{3-x}IG$ thin film (see chapter 5). The processed data was normalized to the film volume and underwent linear background subtraction.

2.2 X-Ray Diffraction

The main structural characterization tool used in this thesis was a scattering technique known as X-ray diffraction, or XRD (a Bruker D8 diffractometer was used for high-resolution XRD, and a Rigaku Smartlab diffractometer was used for powder XRD). At a very simple level, X-ray diffraction can be understood to be caused by constructive interference of X-rays scattering off of adjacent atomic planes. The condition for this to occur is the celebrated Bragg's Law:

$$\lambda = 2dsin\theta \text{ [1]}$$

where λ is the wavelength of incoming X-rays, d is the atomic plane spacing, and θ is the incident/scattering angle (see figure 2.3). This simple picture fails at describing many phenomena

in real diffraction experiments (peak intensities, Laue fringes, forbidden reflections) but describing more advanced theories such as kinematical or dynamical diffraction is well beyond the scope of this thesis, and for more information the reader is directed to textbooks on the subject.[78,79]

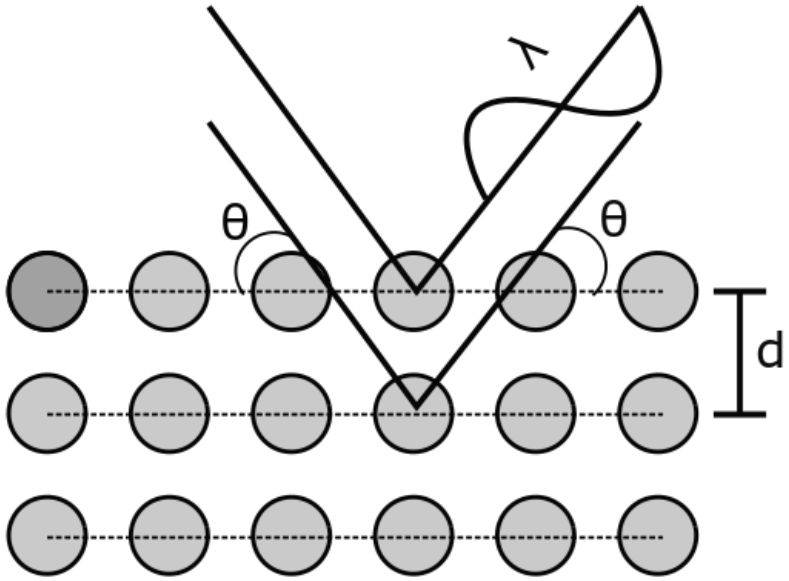

Figure 2.3: Schematic of the simple XRD model captured by Bragg's law

The type of data acquisition and analysis used depends on the type of diffraction measurement:

High Resolution XRD (HRXRD) of Thin Films: To analyze the structure of thin single-crystalline films, high-resolution XRD was used. After manual alignment on a specific substrate peak (i.e. the (444) reflection for (111)-oriented films, scans were taken over a ~3-4 degree range with a 0.001 degree step size and a 0.4 second dwell time. Analysis such as fitting and extraction of film peak positions was carried out using dynamical diffraction packages such as Rigaku Globalfit or Leptos; more details can be found in chapters 3 and 5.

X-Ray Reflectometry (XRR): XRR was used to determine the thickness of every film discussed in this thesis. The theory of XRR can only be understood via dynamical diffraction (i.e. solving

Maxwell's equations for the XRR geometry)[78]. Thickness values were extracted from XRR data by fitting to the film thickness, density, and roughness with Leptos.

Powder XRD: Powder XRD was used to ensure that the homemade targets used in PLD growth processes (see below) were single-phase. After an automated alignment in the Rigaku Smartlab diffractometer, a scan ranging from 10-120 degrees was taken, lasting 1.5 hours. Rietveld refinement in the HighScore Plus software was carried out for phase and defect identification.

2.3 Spin Hall Magnetoresistance

The main technique used to characterize the spintronic properties of Pt/REIG heterostructures in this thesis is spin Hall magnetoresistance (SMR). As we saw in chapter 1, heavy metals (HM) such as Pt exhibit a magnetotransport phenomenon known as the spin Hall effect which causes a spin accumulation σ at the top and bottom interfaces. An adjacent magnetic insulator (MI) can absorb or reflect this spin accumulation depending on the relative directions of the film magnetization and σ. The theory for this phenomenon was first worked out by Chen *et al*. in the mid-2010s[67,80]. Figure 2.4 depicts the spin accumulation and spin current in the Pt layer as a function of depth; as the in-plane angle of the magnetization changes, the magnitude of the spin accumulation and spin currents change. The magnitude of this effect depends on the spin mixing conductance of the interface and the spin Hall angle in the Pt.

This dynamic equilibrium causes a *different* spin accumulation than what is predicted by the spin Hall effect alone, so the Onsager reciprocal process (the inverse spin Hall effect, ISHE) becomes active. The ISHE causes a nonequilibrium spin accumulation to induce a transverse voltage, which is measurable. This interplay between the SHE and the ISHE is known as spin Hall magnetoresistance.

Empirically, the transverse SMR is described by the equations[10]:

$$\rho_{trans}^{PHE} \cong \Delta\rho_1 m_x m_y$$

$$\rho_{trans}^{AHE} \cong -\Delta\rho_2 m_z \text{ [1]}$$

where "AHE" denotes the similarity to the anomalous Hall effect (sensitivity to the z-component of the magnetization) and "PHE" denotes the similarity to the planar Hall effect (sensitivity to $m_x m_y$). The PHE-like SMR is maximized when the magnetization is oriented 45 degrees away from the current direction. By solving the drift-diffusion equations mentioned in chapter 1, Chen *et al*. derive a microscopic model for the SMR coefficients:

$$\frac{\Delta\rho_1}{\rho} = \frac{\theta_{SH}^2\lambda}{d_N}\frac{2\lambda G_r \tanh^2\frac{d_N}{2\lambda}}{\sigma+2\lambda G_r \coth\frac{d_N}{\lambda}} \text{ [3]}$$

$$\frac{\Delta\rho_2}{\rho} \cong \frac{2\lambda^2\theta_{SH}^2}{d_N}\frac{\sigma G_i \tanh^2\frac{d_N}{2\lambda}}{\left(\sigma+2\lambda G_r \coth\frac{d_N}{\lambda}\right)^2} \text{ [4]}$$

where $\rho = \sigma^{-1}$ is the Pt resistivity, d_N is the Pt thickness, λ is the spin diffusion length, and G_r (G_i) are the real (imaginary) parts of the spin mixing conductance. The PHE-like SMR is sensitive to the real part of $G_{\uparrow\downarrow}$ and the AHE-like SMR is sensitive to the imaginary part of $G_{\uparrow\downarrow}$, making SMR a potent tool for characterizing the quality of spintronic interfaces.

The measurement setup used to characterize SMR in chapter 3 is displayed in figure 2.5. A lock-in amplifier (Stanford Research SR830) was used to apply a periodic excitation to the Hall bars, and also to read the Hall signal. A sample-dependent offset (often much larger than the AHE/PHE-like SMR signal) was subtracted by the SR830. The analog output of the SR830 was input into a Measurement Computing analog to digital converter (ADC) which was in turn read by a custom Labview script. The Measurement Computing ADC also contained a DAC which was used to drive

the electromagnet power supply (custom-built). The time constant of the SR830 was set to minimize noise while still providing sufficiently fast response during field sweep experiments, and the gain was set to the maximum possible level while avoiding preamp overload.

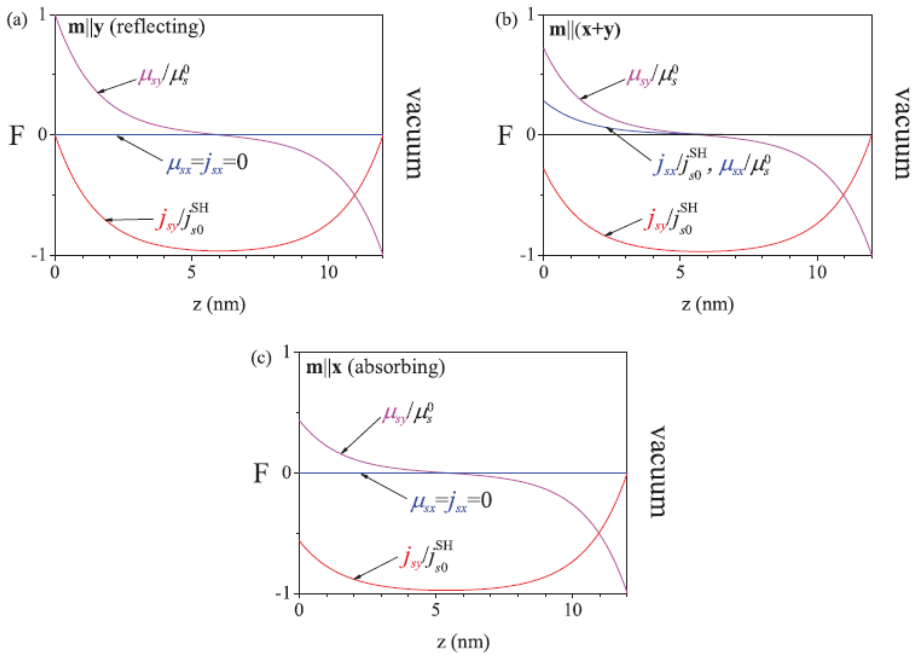

Figure 2.4: Spin accumulations and spin currents in an FI/NM/vacuum heterostructure as a function of magnetization direction. The absorption/reflection of the SHE-induced spin accumulation gives rise to SMR through the ISHE. Reproduced from Chen *et al* (2013) with permission[80]

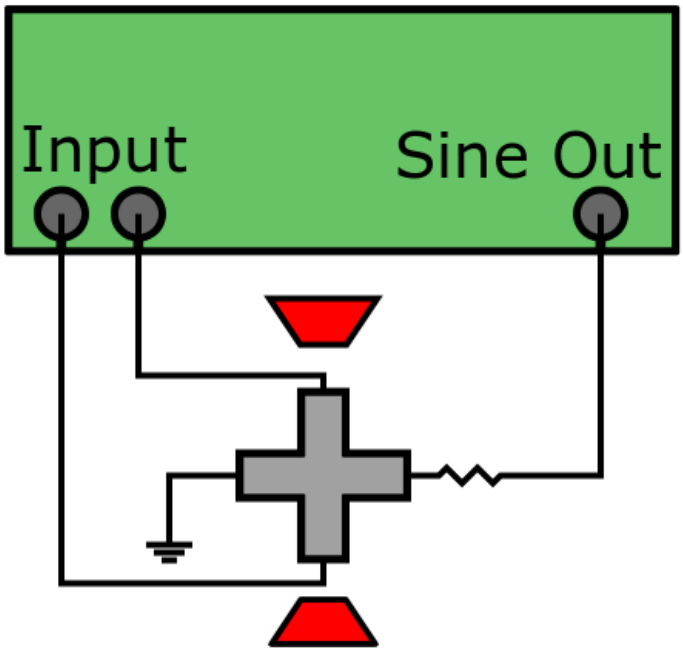

Figure 2.5: Schematic of SMR setup used in Chapter 3. The green box is an SR830 lock-in amplifier, the grey cross is a Hall cross device, and the magnet is shown in red.

2.4 Photolithography

In chapters 3 and 6, Hall bar devices are patterned in order to measure phenomena such as the spin Hall magnetoresistance (SMR). In this section, the fabrication scheme of these devices will be reviewed. As noted in chapter 1, a heavy metal (HM) such as platinum (Pt) is needed to obtain phenomena such as SMR. Past research[81] has shown that the SMR signal is maximized (for a constant current) in Pt/YIG for a sputtered Pt layer 4 nm in thickness, so this is the layer thickness which we used in all devices fabricated for this thesis. This study also showed that sputtered Pt

provides a higher spin-mixing conductance than evaporated Pt, so we used sputtering as well. The process which we used is depicted graphically in figure 2.6.

Hall Bar Fabrication Process:

1. Cover 1x1 cm garnet sample in photoresist and dice into four 5x5 mm pieces in a Disco dicing saw. This is done so that multiple tests can be carried out on a single sample.
2. Sonicate sample in acetone and IPA (5 minutes each) to remove photoresist, then ash in 200 W and 0.75 mT of O_2 (Glow Research AutoGlow) for 3 minutes to ensure a clean surface.
3. Deposit 4 nm of Pt (this was accomplished by graduate students in Professor Geoffrey Beach's and/or Professor Luqiao Liu's research groups)
4. Step 1 of lithography: a positive photolithographic process was used to define the Hall bar structures. First, the samples were cleaned with acetone and IPA and baked for >10 min at 120C to dehydrate the surface. Then, AZ3312 was spun on and the samples were softbaked at 100C for one minute. After exposure (12 seconds) the samples were developed in a dilute TMAH-based developer (AZ 300) for between 1-2 minutes.
5. Dry etching (ion milling) to transfer the photoresist pattern into the film (Intlvac Nanoquest Pico). Profilometry can be used to determine whether the etching has gone "far enough". A slight amount of overetching is fine and is preferable to underetching.
6. Removal of photoresist: in order not to disturb the sensitive garnet/Pt interface, sonication is not used after this point. A bath of warm (60-80˚C) NMP for a few hours with agitation and light mechanical brushing with a cotton bud is generally enough to remove the photoresist from the first lithographic step.

7. Step 2 of lithography: a negative photolithographic process was used to define regions for contact pads. The same process as was used in step 4 was used here.
8. Contact deposition and liftoff: 100 nm of gold is deposited on a thin tantalum adhesion layer to act as contact pads (this was accomplished by graduate students in Professor Geoffrey Beach's and/or Professor Luqiao Liu's research groups). A similar process to that used in step 6 is applied for liftoff of the excess gold.

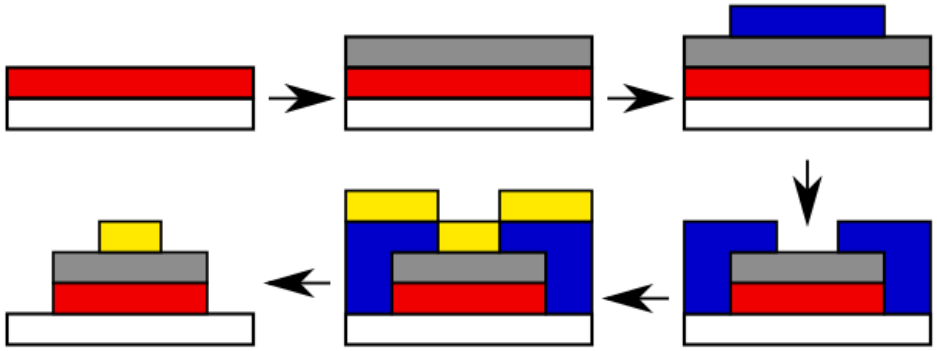

Figure 2.6: Schematic of lithography process used to pattern Hall bars in this thesis. Color legend: White = GGG, Red = REIG, Grey = Pt, Blue = Photoresist, Yellow = Au/Ta

2.5 MOKE Microscopy

In chapters 4 and 5, magneto-optical Kerr effect (MOKE) microscopy is used in order to visualize the effects of composition and temperature on the anisotropy of garnet thin films. For garnet films, MOKE microscopy is preferred over MFM because MFM tips can "drag" domains around due to low domain wall pinning. MOKE microscopy can image domains without disturbing their morphology. The MOKE microscope used was custom-built and programmed by the author in collaboration with Dr. Kai Litzius and David Bono. In this section, the working principle of MOKE

microscopy will first be reviewed. Then, the hardware and software of the custom MOKE microscope will be discussed in detail. It is hoped that through this description other workers will be able to build or troubleshoot their own MOKE systems.

2.5.1 Working Principle

The magneto-optical Kerr effect (MOKE) was first reported by John Kerr in 1877 in his paper, "On rotation of the plane of polarization by reflection from the pole of a magnet"[82]. He summarized the effect as follows:

"When plane-polarized light is reflected perpendicularly from the polar surface of an iron electromagnet, the plane of polarization is turned through a small angle in a direction contrary to the nominal direction of the magnetizing current".

In other words, the sense of the rotation depends on the nominal direction of the "magnetizing current" (magnetization direction). In order to leverage this effect, a polar MOKE microscope uses a polarizer and an analyzer in the light path to cause up and down domains to manifest as bright and dark contrast. In addition, a quarter wave plate is included to remove ellipticity induced by the sample[29]. However, an issue with taking MOKE microscope images of garnet films is that the MOKE contrast is strongly wavelength-dependent – the most important aspect of our home-built MOKE system is the proper choice of the LED wavelength. In order to understand our choice of wavelength, we first review the physical origin of MOKE.

MOKE can be understood on a purely phenomenological level by appealing to Fresnel's equations[29]. For the geometry of our (polar) MOKE microscope with PMA thin films, the ratio of reflected to incident amplitude is:

$$A_{tot} = -R_p \cos(\Psi_p) \sin(\alpha_s) + R_s \sin(\Psi_p) \cos(\alpha_s) + R_K^{pol} \cos(\alpha_s - \Psi_p)\, m_{pol} \quad [5]$$

In this expression, R_p and R_s are the regular reflection coefficients of the material, Ψ_p is the polarizer setting measured from the plane of incidence, and α_s is the analyzer setting measured perpendicular from the plane of incidence. R_K^{pol} is the polar Kerr amplitude of the material under study, and m_{pol} is the polar magnetization of the thin film.

From Eqn. 1, an expression for the Kerr intensity of two antiparallel domains can be derived[29]:

$$I_{\pm} = (A_N sin\alpha_s \pm A_K cos\alpha_s)^2 + I_0 \text{ [6]}$$

where I_0 is the background intensity, A_N is the "regular" reflection intensity, and A_K is the Kerr reflected intensity. Then, the contrast is just I_+-I_-, or:

$$Signal = 2\sin(2\alpha_s)\, A_K A_N \text{ [7]}$$

For a good description of how to optimize the polarizer, analyzer, and quarter wave plate settings for optimum contrast, see "Magnetic Domains: The Analysis of Magnetic Microstructures", Chapter 2[29]. A schematic of the polar MOKE geometry is displayed in Figure 2.7

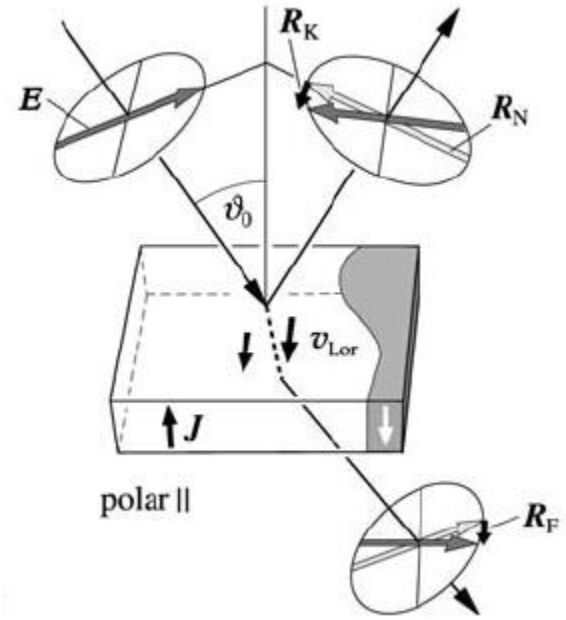

Figure 2.7: Polar MOKE geometry. The transmitted light is rotated through the Faraday effect (a similar magnetooptical effect which operates in transmission rather than reflection). Reprinted from "Magnetic Domains: The Analysis of Magnetic Microstructures" with permission[29].

The term of importance in the A_{tot} equation is the one that involves the polar Kerr amplitude – in garnets, this is strongly wavelength-dependent. To understand the origin of this wavelength dependence, we must examine the microscopic mechanism of Kerr rotation. A full description of MOKE spectra is far beyond the scope of this thesis (see, for instance, the thesis of Lukáš Beran[83]), but a short description will aid in the understanding of the MOKE spectrum of garnets which was used for the selection of our MOKE light source.

In a quantum-mechanical sense, magneto-optical effects are caused by angular momentum selection rules. A magnetic field (either an applied field or an exchange field) removes the degeneracy of previously degenerate atomic term symbols or multiplets and causes left-hand circularly polarized (LHCP) and right-hand circularly polarized (RHCP) to excite different transitions. In particular, (L)RHCP light will only excite transitions with $\Delta J = \pm 1,0$ and $\Delta M = (+1) - 1$[84]. Following Zvezdin and Kotov[84] we can consider the simple transition $^1S \rightarrow {}^1P$ in order to see how this fact gives rise to a MOKE spectrum (The MOKE spectrum of garnets is far more complex and will be presented later, but the same physical intuition holds). ^1P splits its 3-fold degeneracy in a magnetic field while ^1S is nondegenerate (see figure 2.8). Also, LHCP light can only excite a transition to the m=+1 state while RHCP light can only excite a transition to the m=-1 state. In order to obtain the MOKE spectrum of this simple case, the Kramers-Heisenberg formula for polarizability can be used[84]:

$$\alpha_{ij} = -\frac{1}{\hbar}\sum_{ab}\rho_a\left\{\frac{d_{ab}^i d_{ba}^j}{\omega_{ab}+\omega-i\Gamma_{ab}} + \frac{d_{ab}^j d_{ba}^i}{\omega_{ab}-\omega+i\Gamma_{ab}}\right\}$$ [8]

Where a denotes a ground state, b denotes an excited state, ρ_a is the occupation of state a, $d_{ab}^i \equiv \langle a|i|b\rangle$ where i = X,Y,Z (dipole operator), $\hbar\omega_{ab}$ is the transition energy, and Γ_{ab} is the FWHM of the transition. The permittivity ϵ_{ij} is proportional to the polarizability, and the dielectric permeability tensor for an isotropic magnetic medium can be written as:

$$\epsilon = \begin{pmatrix} \epsilon_1 & -ig & 0 \\ ig & \epsilon_1 & 0 \\ 0 & 0 & \epsilon_0 \end{pmatrix}$$ [9]

Therefore, the permittivity tensor can be derived from the quantum-mechanical consideration of atomic term symbols and transition matrix elements. The Kerr angle is then:

$$\Phi_K = -Im\frac{g}{\sqrt{\epsilon_1}(\epsilon_1^2-1)}$$ [10]

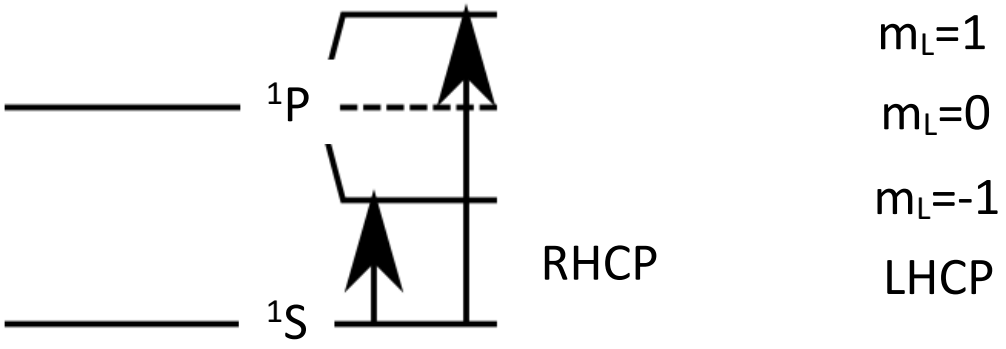

Figure 2.8: Energy level diagram for the ^{1}S→^{1}P transition in a magnetic field

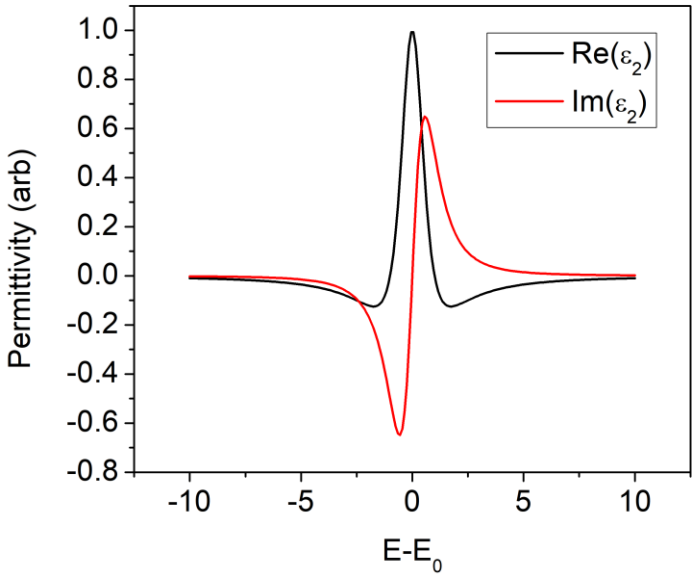

Figure 2.9: Spectral dependence of the off-diagonal components of the permittivity for the $^1S \rightarrow {}^1P$ transition considered in Figure 2.8

For a real material such as a garnet, the situation is much more complex but is still based on the same underlying physics. The spectrum is simply a combination of many transitions such as the one in figure 2.9. In collaboration with Dr. Lukáš Beran, the MOKE spectra of various garnets grown by PLD have been measured (see figure 2.10)[83]. At room temperature, the spectra are dominated by large peaks around 4.0 and 4.5 eV (270 and 300nm). This corresponds to transitions due to the octahedrally and tetrahedrally coordinated iron ions and thus is independent of the particular rare-earth ion. Thus, a light source chosen in this region has a good chance of providing strong MOKE contrast. **The exact color isn't as important as not using white light, because the positive and negative deviations from zero in the MOKE spectrum cause the MOKE microscope contrast from white light to vanish.** A blue light source of 457 nm was chosen for our custom MOKE microscope.

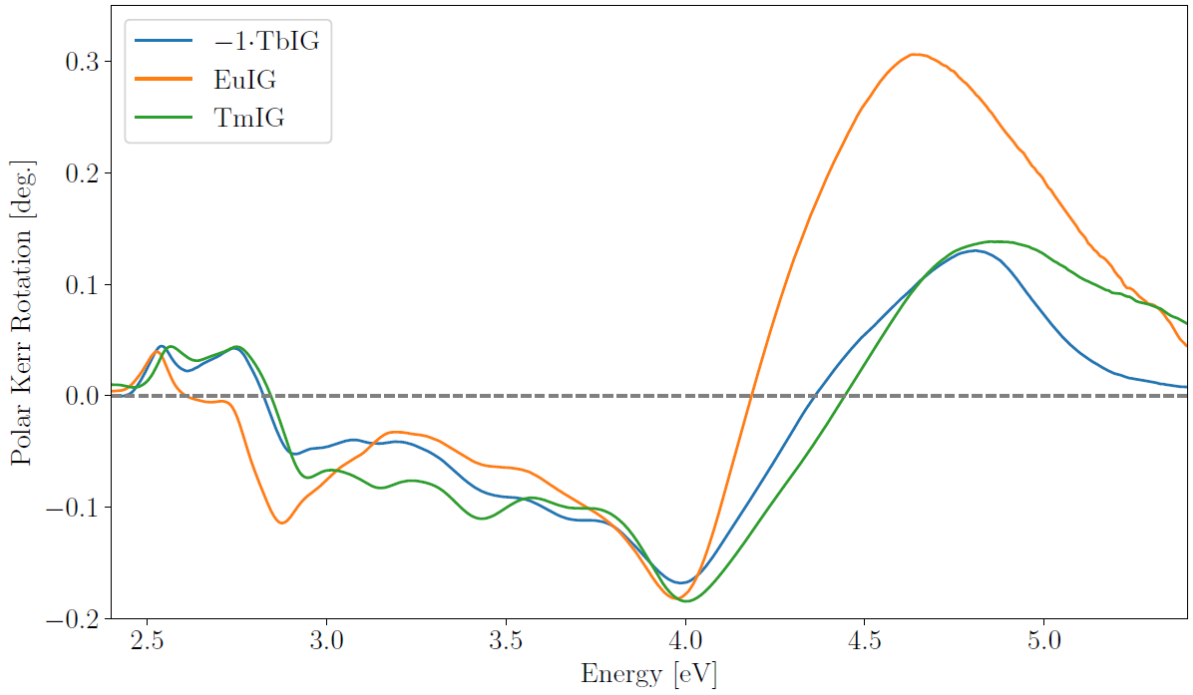

Figure 2.10: Polar MOKE spectra from TbIG, EuIG, and TmIG thin films, courtesy of Dr. L. Beran.

2.5.2 Hardware Construction

A photograph of our MOKE microscope is shown in figure 2.11. The main optical components (light source, illumination optics, polarizer, analyzer, quarter wave plate, and camera) are all shown. For our camera, we used an inexpensive Blackfly S USB3 CMOS camera. Two objectives – 10x and 100x – are available, providing 500nm/px and 80nm/px resolutions respectively. Portability, rigidity, and vibration isolation are ensured by building the entire system on a single granite slab with rubber feet. A motorized stepper stage allows for repeatable sample positioning and remote control. A Peltier sample stage allows for temperature control in the range 273K-350K. For diagnostic purposes, an additional photodetector is available for incident light intensity measurements.

Magnetic field control is accomplished by using a Measurement Computing DAC as input to a Crown audio amplifier. Our magnet design went through a process of iteration. The first magnet we used was a simple coil with a straight iron pole piece. However, this magnet had issues with heating and divergence of the magnetic field in the in-plane direction (see figure 2.12, top). In order to solve these issues, we constructed another magnet using a potted electromagnet with iron pole pieces in a magnetic circuit (see figure 2.12, bottom). The magnetic circuit served to pull the magnetic field out of plane, causing far better uniformity, stronger out-of-plane fields at the same drive current, and lower in-plane fields over our sample size of ~1cm x 1cm. In addition, the new magnet has a tilt table that allows the compensation of sample tilt with respect to the objective.

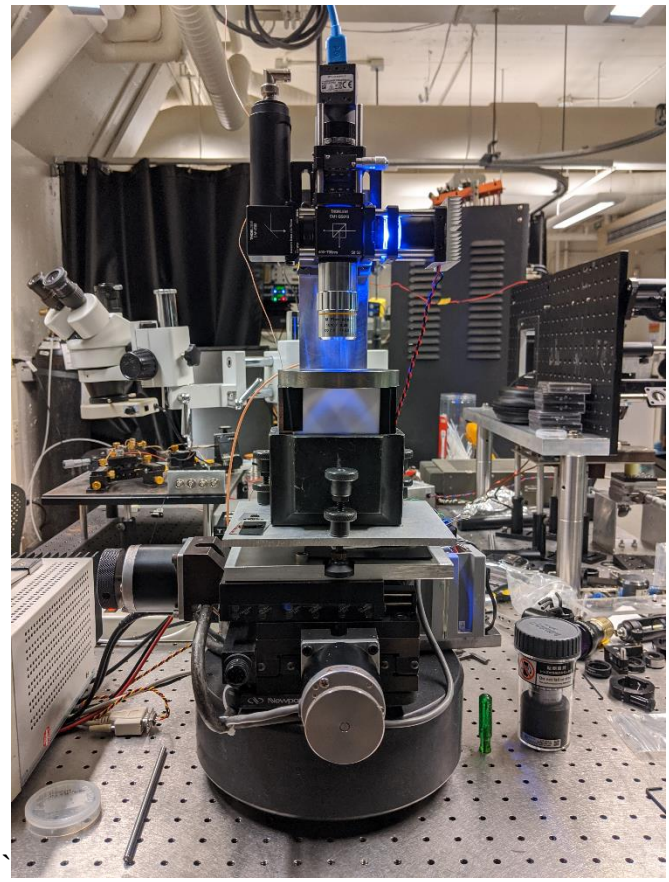

Figure 2.11: Photograph of custom-built MOKE system discussed in this section

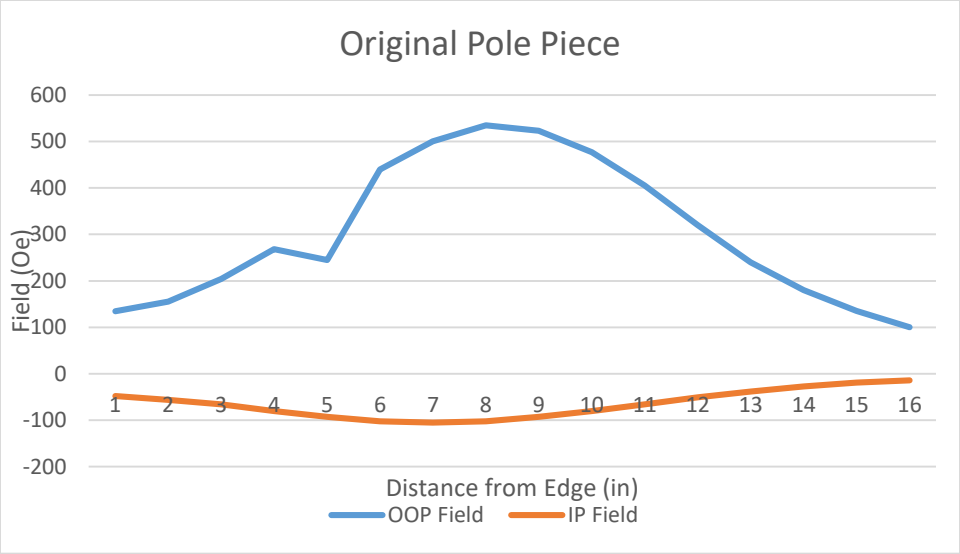

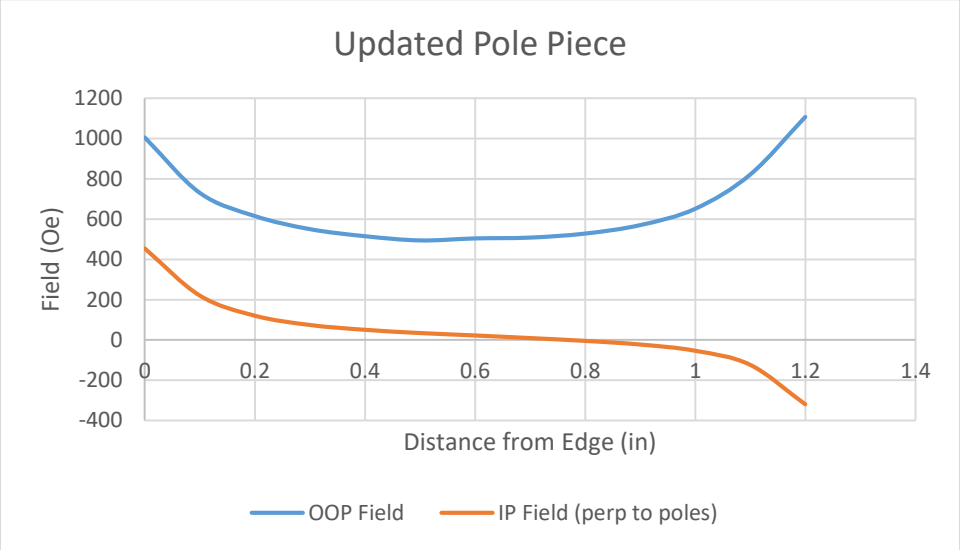

Figure 2.12: Comparison of field uniformity (in- and out-of-plane) for the original and updated pole pieces

There is further room for improvement in the hardware construction of the MOKE microscope. Most significantly, the illumination optics can be improved by the addition of an additional lens

and an adjustable aperture. Although the resolution and SNR of the existing hardware were adequate for the present thesis, further gains can be made by improving the illumination optics.

2.5.3 Software Design

After years of using Labview to control laboratory equipment, the author finally decided to jump ship and try his hand at Python. He discovered that, by using the Python Tkinter library, instrument control software such as that which was used in the MOKE microscope can be easily and quickly written. Camera control was accomplished by using the library “simple-pyspin” developed by the Kleckner lab at UC Merced.

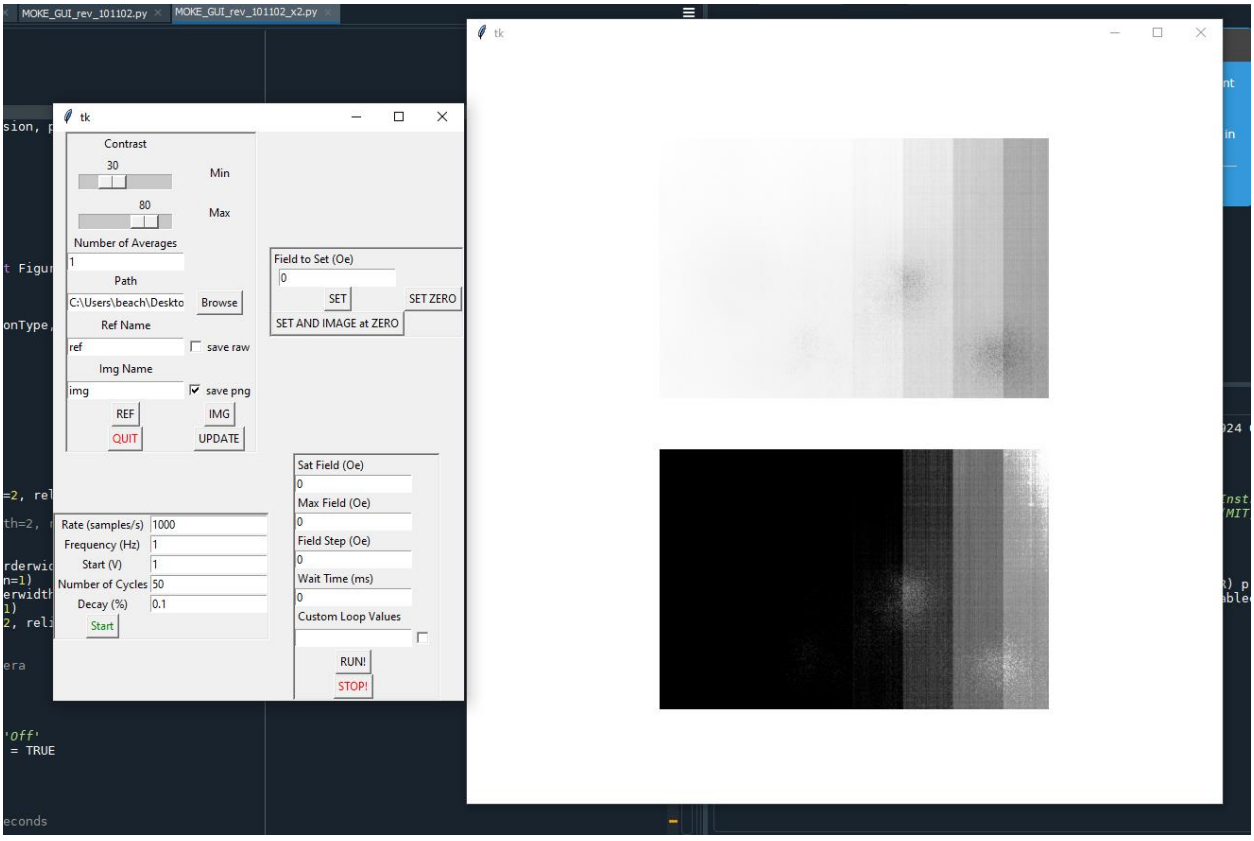

Figure 2.13: Graphical User Interface (GUI) of our MOKE system, written in Python. The control panel is the window on the left, and the images are displayed in the window on the right.

The GUI is displayed in figure 13. In order to take an image, the number of averages must be set (good values are 30-50 if time resolution is not required) and a reference image must be taken using the REF button. A reference image can either be taken at saturation or in an AC demagnetized state (accomplished by using the field control or AC demagnetization widgets). After a reference has been acquired, an image can be taken by pressing the IMG button. The reference and the last acquired image are displayed in a separate window, and the reference is automatically subtracted from the image (the raw images can be acquired by clicking the "raw" checkbox). Sliders at the top of the window allow the contrast to be set by reducing the maximum and minimum allowed pixel intensities. Simple hysteresis loops can be acquired with a single reference image either by choosing a maximum field and a field step or by inputting field waypoints. Finally, video capabilities are not implemented at this point but videos (actually frames acquired at the camera's native frame rate) can be taken by hitting the video button. The number of frames will be equal to the number of averages.

At this point, real-time camera control is accomplished through the FLIR Spinview software. Upon connection of the camera, all automatic controls must be turned off to increase camera sensitivity (automatic gain control, gamma, white balance, etc). The image size is reduced by ¾ to maximize frame rate, and the exposure is set so that the CMOS camera sensor is almost (but not quite) saturated. In future iterations of the software, these capabilities can be offloaded onto the Python script.

2.6 Pulsed Laser Deposition

All garnet films in this thesis were grown using pulsed laser deposition (PLD). As an alternative to MBE (in fact, PLD is sometimes known as laser MBE), PLD is well-suited to the rapid prototyping and growth of complex, multicomponent oxide thin films. PLD was originally developed to grow high-temperature superconductors in the 1980s and now has achieved widespread acceptance in the perovskite and garnet communities. Prior to the present work, PLD was used by our group to grow magneto-optical materials such as Ce:YIG for applications such as optical isolators. The author has optimized PLD growth recipes for rare-earth garnet films with PMA and explored the effects of various growth parameters on their properties. In this section, the operating principles of PLD will be reviewed. Details about reoptimizing PLD process parameters will be given. Finally, the specific process used to grow garnets in this thesis will be discussed.

2.6.1 Operating Principle of PLD and Process Parameters

A schematic of a prototypical PLD growth system is presented below (figure 2.14). During PLD growth, an excimer laser (Lambda Physik Compex Pro, wavelength = 248nm) is fired repeatedly at a target – a sintered ceramic puck made of the desired material. When the laser hits the target, it interacts with the target by ionizing the surface and causing a plume of plasma to travel towards the substrate holder, which is heated to allow for epitaxial growth (see below). A background gas can be present – this can be used to modulate the composition of the film and to change properties of the plasma plume.

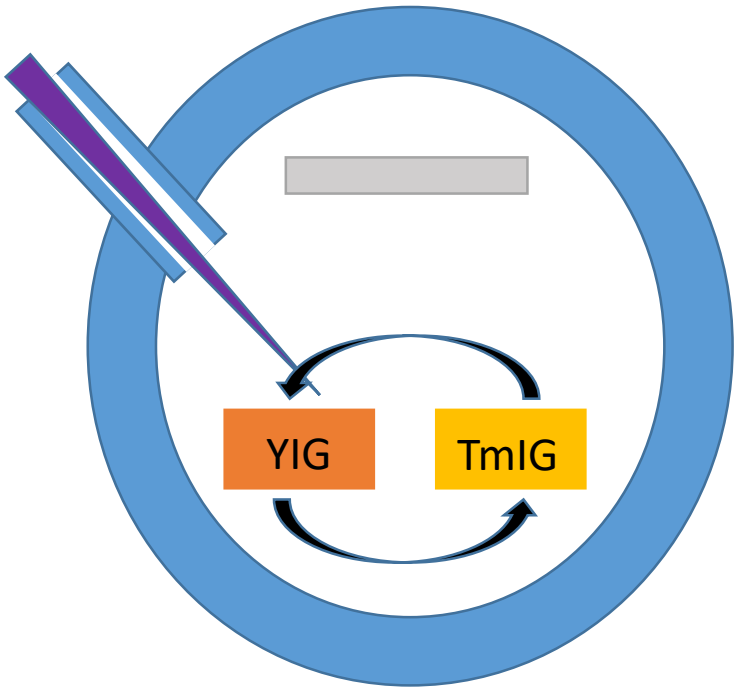

Figure 2.14: Schematic of a PLD system. The laser enters from the top left and impinges on a target (in this example, YIG and TmIG targets are loaded). A plume then forms and travels towards the substrate holder/heater (top grey block)

In this process, there are various parameters which can be tuned in order to vary film properties. These parameters are temperature, O_2 pressure, laser fluence, laser repetition rate and substrate-target distance. These properties all affect the PLD growth process in an inter-dependent way. Therefore, in practice all are kept constant except for one or two which are varied in order to achieve a desired result.

2.6.2 PLD Kinetics

Classically, for growth processes near equilibrium (such as MBE), the growth mode of a film is controlled by the balance of surface tensions γ between the substrate, the growing film nuclei, and the gas phase. We can identify two common cases[85]:

$$\gamma_{substrate-vapor} < \gamma_{substrate-film} + \gamma_{film-vapor} \rightarrow Island\ Growth$$

$$\gamma_{substrate-vapor} \geq \gamma_{substrate-film} + \gamma_{film-vapor} \rightarrow Layer\ by\ Layer\ Growth$$

In island growth, the nuclei do not wet the surface and grow outwards in 3 dimensions[86]. In other words, if the surface tension between substrate and film is too high, the nuclei will tend to ball up and form islands rather than a continuous film. In layer-by-layer growth, the nuclei wet the surface completely and grow outwards in two dimensions, resulting in a single planar layer being completed before the next layer begins.

Another important aspect of thin-film growth is the nucleation rate, or the rate at which clusters of adatoms group become stable against dissolution on the surface. This is, in general, process-dependent but a simplified classical expression for the nucleation rate on a surface is[85]:

$$\frac{dN}{dt} \propto \frac{P}{\sqrt{T}} n_s \exp\left(\frac{(E_{des} - E_s - \Delta G^*)}{kT}\right) \quad [11]$$

In this expression, n_s is the nucleation site density, E_{des} is the energy required to desorb an adatom back into the vapor, E_s is the activation energy for surface diffusion, and ΔG^* is the Gibbs free energy change for the coalescence of a critical nucleus. From this expression it is possible to see that if the temperature is reduced or the atom flux (here captured by the pressure P), the nucleation rate will increase. If the nucleation rate is too high, polycrystalline or amorphous films can result. In fact, it is even possible to calculate an "epitaxial temperature" which separates the regions of epitaxial and polycrystalline growth[86].

In pulsed-laser deposition processes, many of the same considerations still hold. However, the situation is somewhat different than the near-equilibrium case just discussed because:

1. Laser pulses lead to extremely high supersaturations on the surface, which lead to low critical cluster sizes[87]
2. Impinging atoms have very high kinetic energies on the order of 1000x higher than MBE growth processes[88].

These facts cause PLD to be a strongly nonequilibrium process in which kinetic effects dominate the observed growth mode. A comparative study on homoepitaxial Ge grown by MBE and PLD found that the higher kinetic energies of the impinging species in PLD leads to a substantial delay in epitaxial breakdown (that is, a transition from epitaxy to amorphous film growth at a critical thickness)[88]. Simulations of PLD processes[89] and experiments[90,91] have also found that high-KE PLD processes tend to produce smoother film surfaces than MBE under identical conditions (background pressure, temperature, etc). The high supersaturation on the surface has also been seen to cause a kinetic crossover from island growth to layer-by-layer growth[91].

In PLD-grown garnet thin films, very few growth mode studies have been carried out. In most studies of garnet, magnetic and spintronic properties are quoted with no reference to the specific growth regime used. In the present thesis, AFM images generally show hillocks - a hallmark of island growth (see figure 2.15). Despite this, our garnet films generally exhibit an rms surface roughness of <1nm. Krichevtsov *et al.*[92] report layer-by-layer growth of YIG by in-situ RHEED diagnostics of the growing film in the temperature range 700˚C-850˚C. To achieve this, annealing of the substrates at 1000˚C in O_2 was utilized to "heal" the substrate surface and expose atomic terraces. This was not carried out in the present work (nor in most other PLD garnet work in the literature). A similar study by Aldosary *et al.*[93] reported atomically smooth

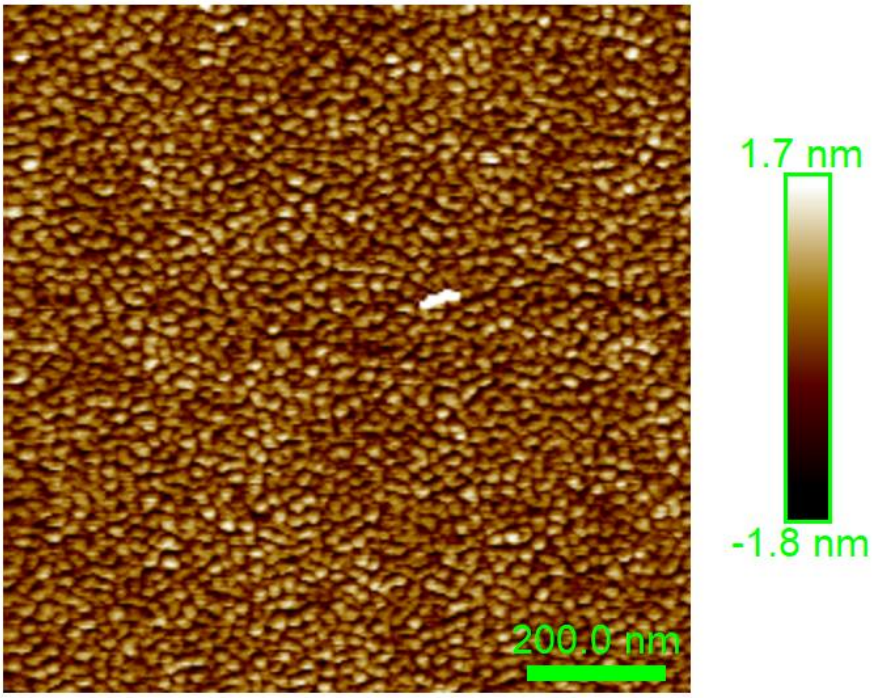

Figure 2.15: AFM image of a EuIG film grown at 30 mTorr O_2. The characteristic hillock pattern of an island growth process is visible (RMS roughness: 0.525nm)

YIG after a substrate annealing step. Krockenberger *et al*. reported layer-by-layer growth (confirmed by RHEED) with a high repetition rate of 40Hz and a substrate temperature of 800˚C[94]. No substrate treatment was reported, but it is possible that the substrates already had an atomic termination. However, they also reported that a laser repetition rate of <20Hz led to amorphous YIG films – an observation not supported by the present work. A study on Yb-doped YAG showed that pulsed laser interval deposition (PLiD) could be used to enforce layer-by-layer growth on annealed YAG substrates[95]. In this process, short bursts of pulses – exactly enough to grow one monolayer – are used with pulse-free relaxation times. This type of process allows for full recovery of a vicinal surface during deposition as evidenced by full recovery of the RHEED intensity.

Perhaps the most important process parameter for PLD growth of garnet thin films in the present work was found to be the laser fluence. Over the course of the research, fluence was optimized multiple times to achieve good magnetic properties. Fluence – energy per unit area – can be varied by tuning the laser pulse energy and by refocusing the laser spot using the optics outside the chamber. Below a certain threshold energy E_{thr} (the energy required to vaporize the target plus any absorption losses in the plasma layer adjacent to the target), ablation of the target does not occur effectively[96]. This threshold energy is material-specific: for instance, a fluence of $0.1 J/cm^2$ is required to grow STO[97] while Si requires $3.5\text{-}4.0 J/cm^2$ [96]. If the laser fluence is too high, however, the film quality can become compromised as the growth rate increases. As a case study for diagnosing PLD growth problems, the reoptimization of the PLD growth process following a laser realignment will now be discussed.

After a laser service, it was noted that the growth rate of TmIG thin films increased by a factor of 4. This coincided with a loss of uniaxial PMA – the TmIG films exhibited switching behavior in in-plane VSM hysteresis loops. Two changes in process parameters caused this behavior: a large increase in laser energy and a change in laser focal position. In order to correct the laser focus, the lens closest to the window was moved and the laser spot was imaged with photosensitive paper (see figure 2.16).

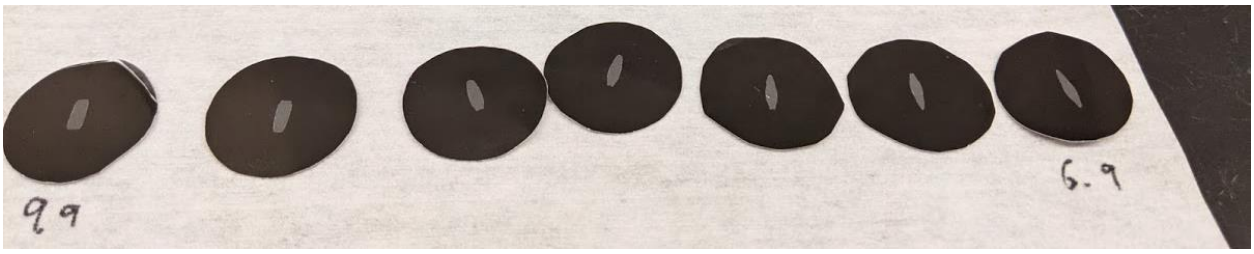

Figure 2.16: Laser spot shapes as a function of lens position.

The lens position was optimized for a sharp-edged rectangular spot similar to that seen in Ohnishi *et* al[97]. Once the optics optimization was complete, the laser energy was decreased until the fluence roughly matched the pre-service value of ~2 mJ/cm^2. This reduction in fluence led to a decrease in the growth rate and a commensurate increase in film quality as evidenced by the return of uniaxial PMA.

2.6.3 Growth Process and Process Parameters

The process for growing films was as follows:

1. Load desired targets and substrates as depicted in the schematic
2. Clean the inner window with diamond polishing paste and isopropyl alcohol – this was done before each growth to avoid possible contamination, damage to the window, and inconsistencies in growth rate
3. Adjust substrate-target distance: a substrate target distance of 8cm was used for all films in this thesis
4. Pump chamber down to a base pressure of 5.5E-6 torr and adjust O_2 pressure to the desired level (generally 150mTorr)
5. Heat substrates to a backside temperature of 900˚C. The frontside temperature was determined to be approximately 650˚C through the use of a thermocouple.
6. Pre-ablate each target with 10,000 shots of the laser in order to remove any possible surface contamination
7. Grow the film by shooting the laser at the target with the shutter open. In order to keep the target surface uniform, the targets were translated and rotated during both preablation and deposition. At a fluence of ~2mJ/cm^2, a deposition rate of ~2nm/1000 shots is achieved.

8. Cool down to room temperature at 10˚C/min at the same O_2 ambient that was used during the deposition process

2.6.4 Target Preparation

Targets for YIG and TmIG were purchased from the Furuuchi Chemical Company. Targets were prepared for TbIG, and EuIG following a modified version of the recipe given in Ibhrahim *el al*[98]. Stoichiometric mixtures of oxide powders (Y_2O_3, Fe_2O_3, Tb_4O_7, Eu_2O_3) were ground in a mortar and pestle and in a ball mill, then pressed into a pellet and calcined at 1150˚C in a tube furnace. This pellet was then re-ground with the mortar and pestle, pressed into a 1" diameter pellet, and sintered at 1350˚C. After this final step, the targets were ground in a dry-grinding process with silicon carbide paper until a mirror-like finish was achieved. The targets were found to be single-phase by powder XRD (see chapter 3). After the initial grinding, the targets were not ground again. In the literature, some authors prefer to grind the surface of their targets before each deposition. This is due to the formation of cone-like structures on the target surface which can exhibit off-stoichiometry[99,100]. These "laser cones" were observed on our targets. However, it was our choice to instead let the target surface reach steady state and instead control film quality through other process parameters.

Chapter 3

Magnetism and Spin Transport in Rare-Earth-Rich Epitaxial Terbium and Europium Iron Garnet Films

This work is adapted from a publication which the author wrote and published in Physical Review Materials[43]*. It is presented mostly in unaltered form, with appendices added as errata on some of the published results*.

3.1 Introduction

Spin transport across heavy metal/ferrimagnetic insulator (HM/FMI) interfaces has attracted a great deal of interest over the past decade. Magnon-mediated spin currents in $Y_3Fe_5O_{12}$ (YIG) were observed by the inverse spin Hall effect in a Pt overlayer,[101,102] and conversely a spin orbit torque (SOT) produced by the Pt layer was used for the propagation and subsequent detection of magnons in YIG.[101,103] These results suggested the possible manipulation of the magnetization of insulating materials with an electric current. SOT-assisted reversal was reported in barium hexaferrite[9], but the first reported switching of a HM/FMI structure by SOT utilized $Tm_3Fe_5O_{12}$ (TmIG or thulium iron garnet) as the FMI layer.[10] Electrical switching of magnetization has applications in SOT-magnetic random access memory and other emerging memory technologies. Materials with perpendicular magnetic anisotropy (PMA) are desirable for such devices because they allow for higher bit densities.[1,2] There has been extensive work on SOT switching of PMA ferromagnetic metals such as Co and CoFeB,[4,68,69,104] but FMIs have two advantages over metals: a more favorable scaling behavior, because the PMA originates from bulk rather than interface anisotropy; and prevention of current shunting from the SOT-producing HM layer.[9]

The best studied FMI is YIG, which is a good insulator with exceptionally low damping, as well as a low magnetostriction and magnetocrystalline anisotropy. YIG films typically exhibit an in-plane easy axis dominated by shape anisotropy, although there are reports of thin YIG films

showing PMA.[57,105,106] Other FMI films have been grown with PMA, notably barium hexaferrite ($BaFe_{12}O_{19}$, BaM) grown epitaxially on sapphire with anisotropy field of 17 kOe[9,107]; EuS, with a Curie temperature of 16.6 K[108]; and Co ferrite ($CoFe_2O_4$) grown epitaxially on substrates such as $SrTiO_3$ or MgO.[109,110] Rare earth iron garnets (REIG) with PMA have also been developed, in which the PMA originates from magnetoelastic anisotropy due to the epitaxial mismatch strain of the REIG on the gadolinium iron garnet (GGG) substrate[52,105]. TmIG,[10,52,53] SmIG ($Sm_3Fe_5O_{12}$)[111] and TbIG ($Tb_3Fe_5O_{12}$)[112] films, as well as Ce- or Bi-substituted YIG[59,113,114], exhibit strain-induced PMA. Other thin film RE garnets include GdIG ($Gd_3Fe_5O_{12}$)[115] and LuIG ($Lu_3Fe_5O_{12}$)[116] with in plane easy axis. Out of the PMA RE garnets, TmIG is the most extensively studied in terms of the spintronic properties of the FMI/HM interface[14,53,75,117,118]. TmIG/HM devices exhibited SOT-driven reversal with applied fields as low as 2 Oe and domain wall velocities of order 1000 m/s at a current density of 2.5×10^{12} A/m^2 in the Pt.[14] TmIG/Pt heterostructures were also recently used to study the validity of the bulk spin Hall effect model for SOT.[75]

In this article, we describe the growth, structure, and the magnetic and spintronic properties of two rare-earth iron garnets: TbIG and EuIG ($Eu_3Fe_5O_{12}$). These materials were selected based on their bulk magnetostriction values and their lattice mismatch with respect to GGG, which lead to a magnetoelastic anisotropy contribution that determines the net anisotropy of the film.[32,33] For TbIG and TmIG, the two magnetostriction coefficients λ_{111} and λ_{100} have opposite sign and PMA is expected in films grown epitaxially on (111) GGG but not on (001) GGG.[32] In contrast, the two magnetostriction coefficients of EuIG are of the same sign and EuIG/GGG is expected to exhibit PMA in both the (111) and (001) orientations. EuIG and TbIG were grown by pulsed laser deposition and the composition is enriched in RE compared with the target. We demonstrate efficient spin transport through Pt/TbIG and Pt/EuIG interfaces through anomalous Hall effect-

like spin Hall magnetoresistance (AHE-like SMR) measurements and show that the spin-mixing conductance of Pt/EuIG is approximately orientation-independent, in contrast to what has been observed in Pt/cobalt ferrite heterostructures[109]. We demonstrate by magnetometry, magnetoresistance and optical measurements the presence of a compensation temperature[32] near room temperature in TbIG, and report the damping coefficient of the EuIG films.

3.2 Structural and Magnetic Characterization

EuIG and TbIG thin films of thicknesses varying from 10 to 90 nm were grown on GGG (lattice parameter a = 1.2376Å) and substituted GGG (SGGG, a = 1.2497Å) using pulsed laser deposition (PLD) in an oxygen pressure of 150 mTorr. In all cases, the substrate was placed on a sample holder heated to a backside temperature of 900˚C. The frontside (substrate) temperature was not measured but was ~250˚C lower. The targets used in these depositions were prepared by sintering.[53] Further information on the film and target preparation is presented in the Methods section.

The high crystalline quality of these films is evident from the Laue fringes present in each symmetric (444) scan in Figure 3.1a-d, which were taken from representative thin films of each type. Figure 3.1e-f show reciprocal space maps of the (642) reflection of 52 nm thick TbIG films grown on GGG and SGGG substrates. In both cases, the substrate peak is vertically aligned with the film peak, indicating that the films are fully strained to the substrate. This pseudomorphic growth was seen in all of the films prepared for this study.

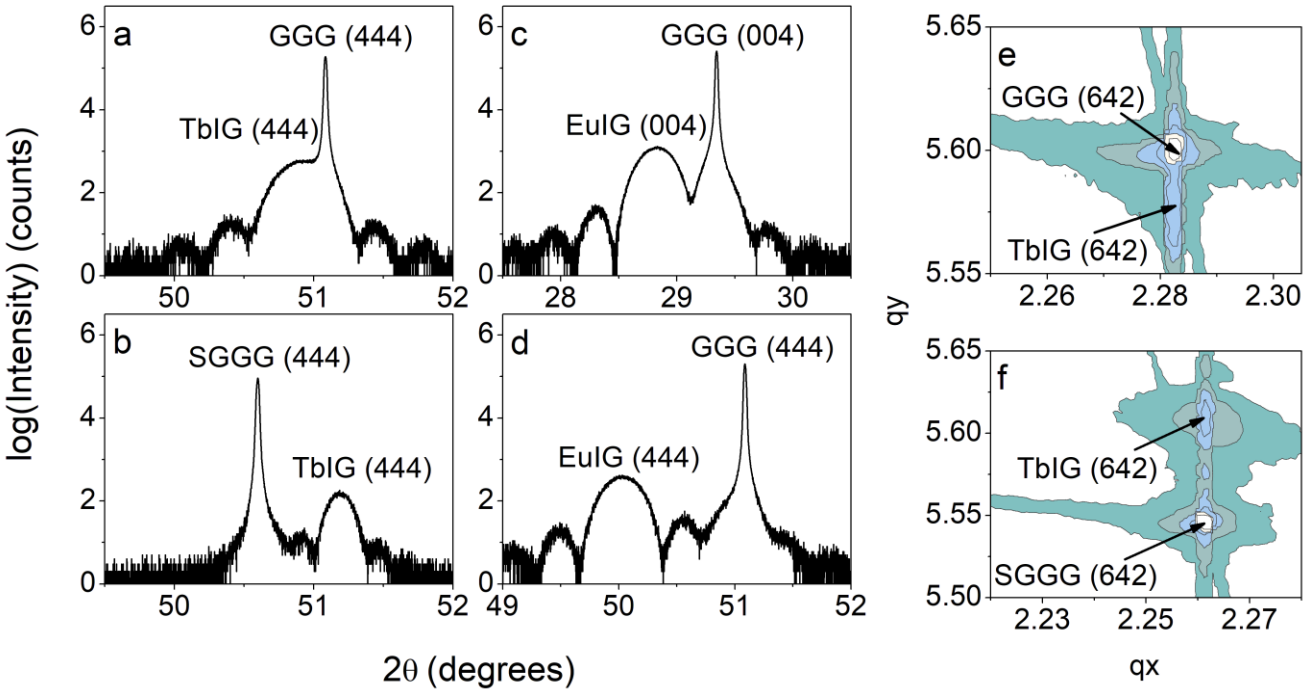

Figure 3.1 (a)-(d) High-resolution XRD ω-2θ scans of representative EuIG and TbIG thin films (e)-(f) High-resolution XRD reciprocal space maps of TbIG/GGG and TbIG/SGGG thin films

Compositional analysis was carried using x-ray The RE:Fe ratio exceeds 0.6 in both cases, with values of 0.72 for EuIG (001) and 0.70 for TbIG. This iron deficiency is consistent with similar XPS analyses of sputtered TmIG films and PLD-grown YIG films which showed Y:Fe ratios as large as 1.37.[117,119]

The XRD did not indicate any non-garnet peaks suggesting that the excess RE is incorporated into the garnet lattice. Although the RE ions have a larger ionic radius than the Fe^{3+}, RE ions including Eu^{3+} and Eu^{2+} can be present within octahedral sites of oxides such as $BaTiO_3$.[120] Tb^{3+}, on the other hand, transitions to Tb^{4+} (a stable $4f^7$ ion) in order to enter octahedral sites.[121]

Indeed, the high resolution XPS spectra (Figure 3.3) indicate the presence of Tb^{3+}, Tb^{4+}, Eu^{3+}, and Eu^{2+} in our films.[122,123] Considering the smaller size of the tetrahedral site, we assume that the RE ions preferentially occupy the octahedral sites. The ability for the RE ions to enter octahedral sites can explain why the garnets are able to crystallize even when the RE:Fe ratio substantially exceeds 0.6. The presence of octahedral RE ions has profound implications for the sublattice magnetization and compensation temperature since the magnetic moment of the RE ions differs from that of the Fe^{3+} which they replace. Furthermore, in order to maintain charge neutrality when the RE valence state differs from +3, Fe^{2+} or Fe^{4+} ions as well as oxygen vacancies may be present in the films. The valence states of the Fe could not be resolved in the XPS data.

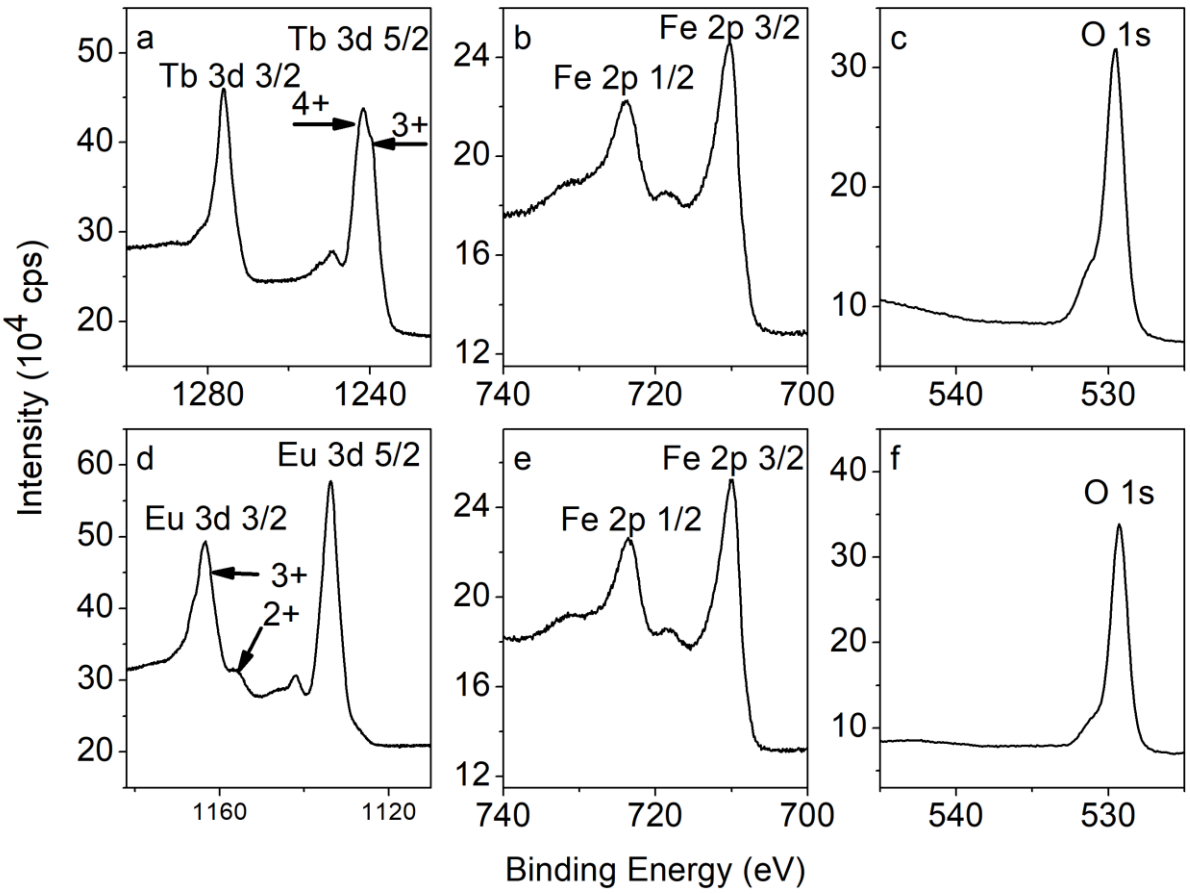

Figure 3.2 (Tb,Eu) 3d, Fe 2p, and O 1s spectra of representative TbIG and EuIG thin films. In the RE spectra, peaks belonging to each oxidation state are marked.

The magnetic properties of the thin films were characterized using vibrating sample magnetometry (VSM). Easy- and hard-axis hysteresis loops for representative TbIG and EuIG films are displayed in Figure 3.3. The net anisotropy of the films is determined by the magnetocrystalline, shape and magnetoelastic anisotropy contributions. The magnetocrystalline anisotropy K_1 is small but negative, and favors PMA for (111) films, whereas the shape anisotropy favors an in plane magnetization. The PMA is primarily driven by magnetoelastic anisotropy overcoming the shape anisotropy. We write the uniaxial anisotropy K_u as the difference between the magnetic energy for magnetization oriented in-plane and the energy for magnetization oriented out-of-plane, where the three terms on the right represent the magnetocrystalline, magnetoelastic and shape anisotropies:

$$K_u = E_{IP} - E_{OP} = -\frac{K_1}{12} - \frac{9}{4}\lambda_{111}c_{44}\left(\frac{\pi}{2} - \beta\right) + \left(\frac{\mu_0}{2}\right)M_s^2 \qquad [1]$$

λ_{111} is the relevant magnetostriction coefficient for the (111) films, c_{44} is the shear modulus, β is the corner angle of the rhombohedrally-distorted unit cell, and M_s is the saturation magnetization.[21,53,124]

From this equation and from the list of bulk garnet properties in Table 1[32], we expect PMA (i.e. a negative K_u) in (111) TbIG under sufficient in-plane compressive strain. The dominant effect of the magnetoelastic contribution is illustrated by a comparison of the net anisotropy of (111) TbIG/GGG and TbIG/SGGG films. Based on the bulk lattice parameters of TbIG, GGG and SGGG, we expect an epitaxial TbIG film to be under in-plane compression on GGG and in-plane tension on SGGG, which is verified by the x-ray data in Figure 1. The VSM hysteresis loops in

Figure 3 indeed show an out-of-plane square loop for TbIG/GGG(111) (Figure 3.3a; compressive strain) while the TbIG/SGGG(111) sample (Figure 3.3b; tensile strain) shows a square in-plane hysteresis loop. Hard-axis loops for TbIG are not shown because the saturation field is higher than the maximum field of 10 kOe available in the VSM.

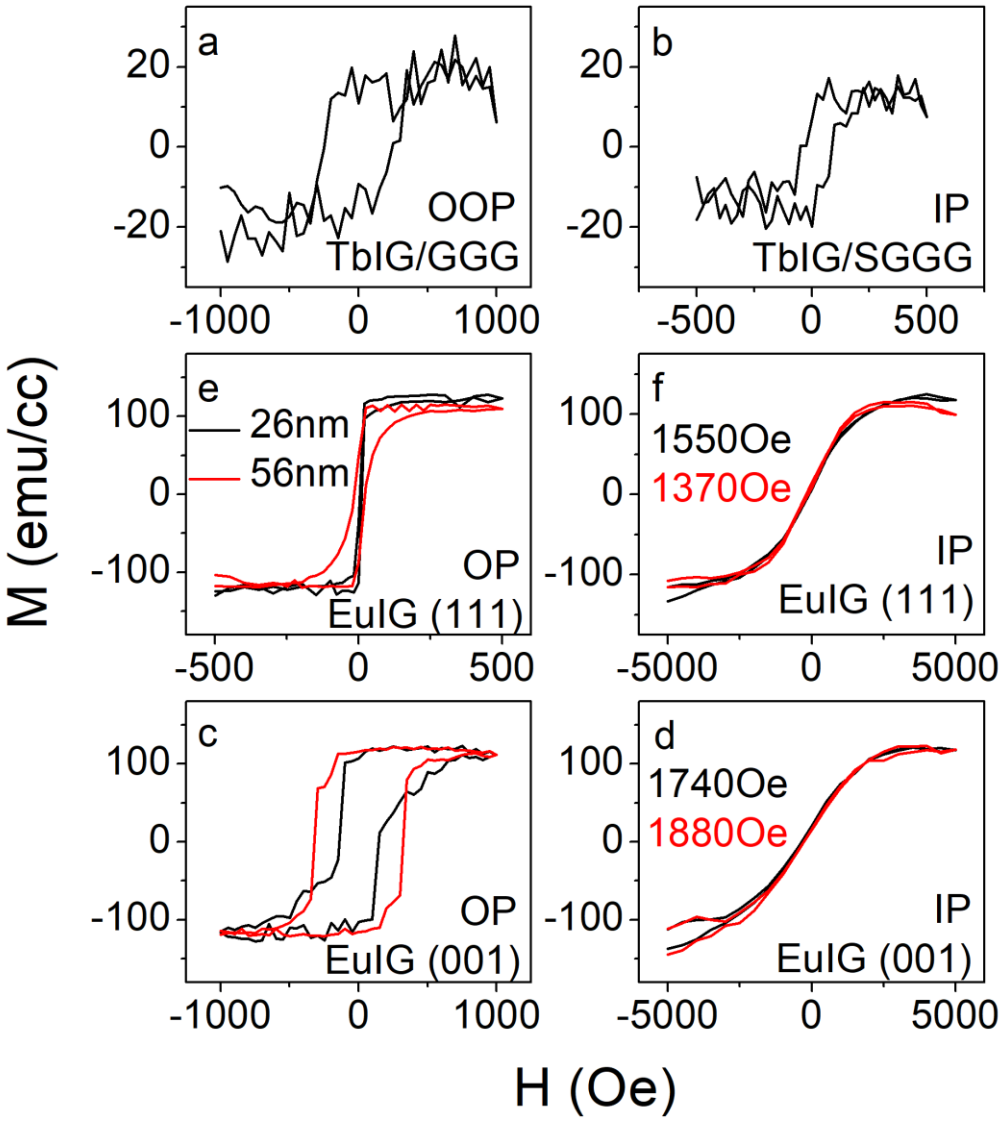

Figure 3.3 In-plane (IP) and out-of-plane (OOP) VSM hysteresis loops of representative TbIG and EuIG thin films. In the IP EuIG hysteresis loops, the estimated anisotropy fields are presented and are color-coded (color online) in the same manner as the loops.

A similar calculation for EuIG films indicates that compressively-strained films on both (001) and (111) GGG are expected to show PMA. This is verified by the in- and out-of-plane VSM hysteresis loops in Figures 3.3c-f, together with the coupled XRD scans in Figure 3.1c-d. PMA is retained up to 56 nm thickness, which is consistent with the X-ray data showing little or no strain relaxation. The saturation magnetization, whose measured values range from 110-118 emu cm^{-3}, is higher than the bulk value of 93 emu cm^{-3} [32], which may be a result of the excess Eu. For both the (111) and the (001) films, the coercivity increased with increasing thickness. The anisotropy field was determined from the hard-axis loops by fitting a straight line to the M(H) curve near zero field and extrapolating to the saturation magnetization. The saturation magnetization was obtained from the easy axis hysteresis loops.

By measuring the strain state from the x-ray data and the anisotropy field from VSM, the thin-film values of λ_{111} and λ_{100} may be found. For the (111) case, a cubic unit cell distorted along one of its [111] directions becomes rhombohedral, and we use a rhombohedral-to-hexagonal transformation to greatly simplify the calculation of strain[79]. The transformation from rhombohedral to hexagonal Miller indices ((hkl) to (HK.L)) is given by:

$$\begin{pmatrix} H \\ K \\ L \end{pmatrix} = \begin{pmatrix} 1 & -1 & 0 \\ 0 & 1 & -1 \\ 1 & 1 & 1 \end{pmatrix} \begin{pmatrix} h \\ k \\ l \end{pmatrix} \qquad [2]$$

The in-plane lattice parameter of the hexagonal unit cell is given by[79]:

$$a_H = \sqrt{12 d_{11\bar{2}}^2} \qquad [3]$$

where $d_{11\bar{2}}$ is the $(11\bar{2})$ plane spacing in the rhombohedral unit cell, assumed to be equal to the $(11\bar{2})$ spacing in the substrate. Finally, the corner angle of the unit cell α is given by[79]:

$$\sin\left(\frac{\alpha}{2}\right) = \frac{3}{2\sqrt{3+\left(\frac{c}{a_H}\right)^2}} \qquad [4]$$

where *c* is the long body diagonal of the rhombohedral cell (or the c-axis lattice parameter of the hexagonal cell). The (001) case proceeds in a simpler manner due to the preservation of the orthogonality of the unit cell axes even after strain. For the (001) films the uniaxial magnetoelastic anisotropy is given by[21,124]:

$$K_u = -\frac{3}{2}\lambda_{100}(c_{11}-c_{12})(\varepsilon_{zz}-\varepsilon_{xx}) + \frac{\mu_0}{2}M_s^2 \qquad [5]$$

where ε_{ii} is the i^{th} axial strain component.

Table 1 shows the values of λ_{100} and λ_{111} for the EuIG films, derived from the total anisotropy measured from the hard axis loops, compared to published bulk values of the magnetostriction parameters.[32] K_1 was neglected in the calculations as it is much smaller than the magnetoelastic and shape anisotropy terms. Also listed in Table 3.1 are the lattice strain determined from the X-ray data and the calculated and literature values[32] for unit cell volume for both EuIG and TbIG. It is interesting to note that, despite the iron deficiency, the unit cell volumes in our films are close to the bulk values.

The calculated magnetostriction in the EuIG films differed from bulk values, and for TbIG, the high anisotropy field suggests that λ_{111} of the film exceeded the bulk value. The difference in

film magnetostriction compared to bulk values may be an effect of the excess RE, or of Jahn-Teller Fe ions. For example Fe^{2+} ions in EuIG may cause an enhancement of λ_{111}.[23] However, the XPS contributions from Fe^{3+} and Fe^{2+} cannot easily be separated.[125,126] It is also possible that growth-induced anisotropy is responsible for the enhancement in λ_{111}; for more information see Chapter 5.

Broadband FMR measurements of EuIG/GGG (111) with thicknesses of 26 nm and 56 nm were carried out at frequencies of $f = 3 – 6$ GHz in fields up to 4.5 kOe to determine the resonance frequency H_{res} and the linewidth ΔH. H_{res} values were averaged for two perpendicular in-plane directions of H. The Gilbert damping parameter α was obtained from the slope of ΔH vs. f. The data gave a linear plot in which the slope is given by $2\alpha/\gamma$, where γ is the gyromagnetic ratio. This yielded $\alpha = 25.7 \times 10^{-3}$ (4% error) for the 26 nm thick film and $\alpha = 24.2 \times 10^{-3}$ (17% error) for the 56 nm thick film. These values are two orders of magnitude greater than the damping of YIG films, and are attributed to the presence of RE, especially in the RE-rich films. Studies on RE-doped YIG have shown that increasing the RE concentration greatly increases the damping parameter.[127,128]

Material	β (degrees)	ε_{xx}	ε_{zz}	H_k (Oe)	M_s (300K) (emu/cc)	λ_{ijk} (10^{-6}) (calculated)	λ_{ijk}(10^{-6}) (literature)	V_{cell} (nm^3) (calculated)	V_{cell} (nm^3) (literature)
EuIG/GGG (111)	89.25	n/a	n/a	1370	110	λ_{111} =7.0	λ_{111} = 1.8	1.93	1.95
EuIG/GGG (001)	90	0.00796	-0.00934	1880	120	λ_{100} =5.0	λ_{100} = 21	1.89	1.95
TbIG/GGG (111)	89.88	n/a	n/a	n/a	19	n/a	λ_{111} = 12	1.90	1.92

Table 3.1. Results of the structural and magnetic characterization of representative EuIG and TbIG films. Experimental values of H_k and λ_{111} are not listed for TbIG because it was not saturated in-plane. Errors in H_k and M_s values are ~5%. The EuIG/GGG H_k values in the table are lower bounds (see Appendix)

3.3 Spintronic Interface Properties

In order to characterize the room-temperature spintronic properties of the FMI/HM interface, we measured the spin-mixing conductance of Pt/(Tb,Eu)IG heterostructures, which is an indicator of the efficiency of spin transport through the interface.[80,129] Hall bar structures (see Figure 3.4d) were fabricated on Pt(4nm)/(Tb,Eu)IG(10nm)/GGG multilayers using photolithography and ion milling techniques, and a lock-in technique[10] was used to collect anomalous Hall effect (AHE)-like spin Hall magnetoresistance (SMR) hysteresis loops. All garnet films used for Hall bar fabrication had <1nm rms roughness as characterized by atomic force microscopy. A sample-dependent offset and a linear background due to the ordinary Hall effect (OHE) in Pt was subtracted, and the results are displayed in Figure 3.4a-c. The square shape of these hysteresis loops matches the out-of-plane magnetometry data. However, the coercivity of the Hall cross is higher than that of the unpatterned film due to the effects of edge roughness on domain nucleation and pinning.[10] In-plane SMR was not measured because the probe station could not supply large enough in-plane fields to saturate the Hall cross devices.

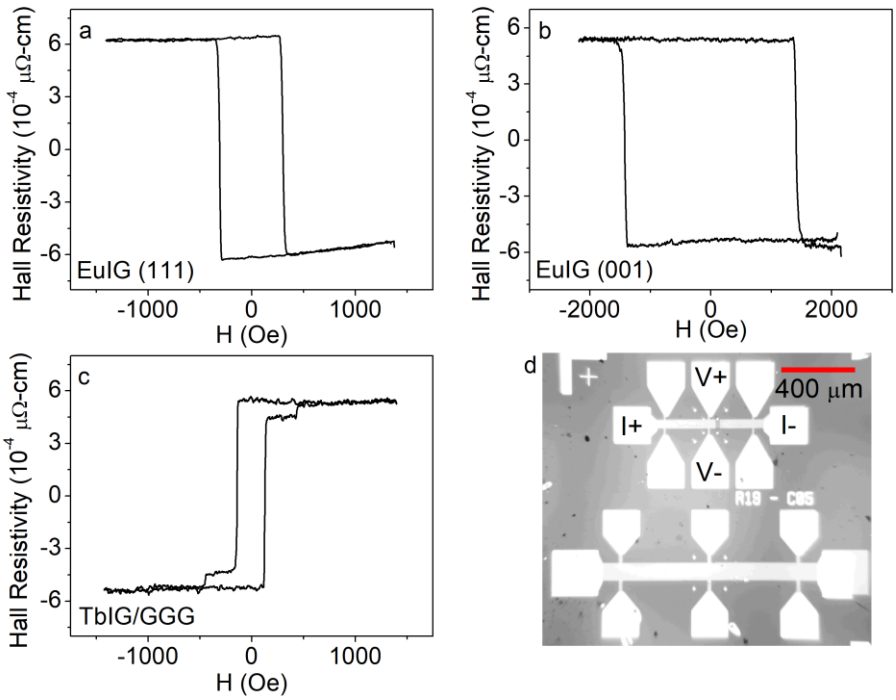

Figure 3.4 (a)-(c) Anomalous-Hall-like SMR hysteresis loops for Pt(4)/REIG(10) heterostructures (d) Optical micrograph of representative Hall crosses used for data acquisition

The origin of the AHE in Pt/ferrite interfaces is a hotly debated topic, with some arguing that it is at least partly due to the magnetic proximity effect (MPE) [118,130] while others maintain that it is fully due to a spin Hall magnetoresistance (SMR) effect.[10,131] Meanwhile, measurements of the magnetic polarization of Pt in direct contact with a magnetic insulator using x-ray methods indicate that the MPE is negligibly small at room temperature.[132–135]In the following discussion, we will assume that the AHE is predominantly due to SMR, as was posited by Avci *et* al. for the similar Pt/TmIG system, and consistent with the lack of MPE at room temperature in other studies.[10,136] The model of Chen et al. for spin mixing conductance[80] leads to:

$$\frac{\Delta\rho_1}{\rho} = \frac{\theta_{SH}^2 \lambda}{d_N} \frac{2\lambda G_r \tanh^2 \frac{d_N}{2\lambda}}{\sigma + 2\lambda G_r \coth \frac{d_N}{2\lambda}}$$
$$\frac{\Delta\rho_2}{\rho} \approx \frac{2\theta_{SH}^2 \lambda^2}{d_N} \frac{\sigma G_i \tanh^2 \frac{d_N}{2\lambda}}{(\sigma + 2\lambda G_r \coth \frac{d_N}{2\lambda})^2} \quad [6]$$

where $\Delta\rho_1$ is the amplitude of an in-plane SMR loop, $\Delta\rho_2$ is the amplitude of an AHE-like SMR loop, ρ is the resistivity of the Pt layer, λ is the spin diffusion length of the Pt layer, θ_{SH} is the spin Hall angle, d_N is the Pt thickness, and $\sigma=1/\rho$ is the Pt conductivity. G_r and G_i are the real and imaginary parts of the spin mixing conductance, respectively. While G_r can be calculated directly from a measurement of $\Delta\rho_1$, it is necessary to know G_r to calculate G_i from a measurement of $\Delta\rho_2$. Without being able to saturate the film in plane during the electrical measurement, $\Delta\rho_1$ and hence G_r could not be determined. However, previous results for similarly constructed Pt/TmIG Hall bars have values for λG_r that are an order of magnitude lower than σ ($2.07 \times 10^6\ \Omega^{-1}m^{-1}$ for our Hall bars).[10,14] Thus we can obtain a lower bound for G_i by dropping the G_r term in the denominator. By substituting values used in a previous study on TmIG[10] for λ and θ_{SH}, we calculate the lower bounds for G_i displayed in Table 3.2.

These data lead to several conclusions about the spintronic properties of EuIG/Pt and TbIG/Pt heterostructures. First, even the lower bound of G_i for Pt/EuIG/GGG and Pt/TbIG/GGG is on the same order of magnitude as G_i in Pt/TmIG/GGG(111)[10], indicating a similar interfacial spin transparency in these materials. Also, G_i for Pt/EuIG/GGG(001) is almost identical to that of Pt/EuIG/GGG(111). The effect of crystal orientation on G_i at metal/ferrimagnetic insulator interfaces has received little study. However, Isasa *et al.*[109] characterized Pt/CFO by fabricating Pt Hall bars on epitaxial CFO(001)/STO and CFO(111)/STO thin films and found G_r^{111} to be

significantly lower than G_r^{001}, especially in devices made using an *ex situ* process similar to ours. This observation was related to a difference in surface termination between the two orientations. A recent theoretical study by Cahaya *et al.* which considered the effects of crystal field splitting on spin mixing conductance supports this claim.[137] A study of the orientation dependence of G_r in Pt/EuIG would provide an interesting comparison to Pt/CFO[109].

Material	Lower Bound of G_i
Pt/EuIG (111)	$4.6\times10^{12}\ \Omega^{-1}m^{-2}$
Pt/EuIG (001)	$5.4\times10^{12}\ \Omega^{-1}m^{-2}$
Pt/TbIG/GGG (111)	$4.6\times10^{12}\ \Omega^{-1}m^{-2}$
Pt/TmIG/GGG (111) [Ref 5]	$7.1\times10^{12}\ \Omega^{-1}m^{-2}$

Table 3.2: Lower bounds of G_i for Pt/REIG heterostructures, calculated in the manner described above

3.4 Temperature-Dependent Properties of TbIG Films

Bulk TbIG has a compensation temperature T_{comp} of 248.6 K[32], making it a convenient system for measuring spintronic phenomena near compensation. (GdIG also has a near-RT T_{comp}, but its weak magnetostriction limits its magnetoelastic anisotropy.) T_{comp} of the TbIG films was measured using three different temperature-dependent techniques. The simplest of these was a temperature-dependent magnetization measurement using VSM (Figure 3.5a), in which a minimum in the magnetic moment is clearly present near 330 K. The VSM data yield a value for T_{comp} in the range of 320 K to 340 K, indicated by a dashed line.

Temperature-dependent AHE-like SMR and Faraday rotation measurements are shown in Figure 3.5b,d. Instead of going to zero, both datasets exhibit a sign change at T_{comp} due to the reorientation of the three magnetic sublattices. Below T_{comp}, the octahedral Fe^{3+} and the Tb^{3+} moments are oriented parallel to the field and the tetrahedral Fe^{3+} moments are antiparallel, while above T_{comp} the orientation is reversed.[84] Because the Faraday effect and the SMR are sensitive to one of the magnetic sublattices rather than to the net magnetization, they exhibit a sign change at T_{comp}.[84,138] These measurements show a compensation point of around 335 K, agreeing with the VSM result in Figure 3.5a. There is an additional sign change seen in the SMR data at 110 K (not shown in Figure 5) which is attributed to the temperature dependence of the magnetic proximity effect in Pt.[136] In addition, the coercivity of the TbIG film as a function of temperature measured from the Faraday rotation hysteresis loops is depicted in Figure 3.5c. As expected for a compensated ferrimagnet, the coercivity diverges approaching the compensation point.

The T_{comp} in our TbIG thin films is higher than that of bulk TbIG by 85 K, which is attributed to the Fe deficient composition. The compensation point is determined by the difference in magnitude of the magnetic moment on the sublattices and therefore depends on the composition[28,138]. The TbIG is expected to accommodate the excess Tb as Tb^{4+} ions (magnetic moment of $7\mu_B$) on octahedral sites normally occupied by Fe^{3+} ($5\mu_B$). Fe^{2+} ions ($4\mu_B$), which have a preference for octahedral sites over tetrahedral sites as seen in the inverse spinel magnetite, may also be present. The structure can then be described as consisting of one sublattice of dodecahedral sites containing Tb^{3+} plus octahedral sites with a mixture of Fe^{3+}, Tb^{4+}, and possibly Fe^{2+}, and the other sublattice of tetrahedral sites containing Fe^{3+}. The dodecahedral plus octahedral sublattice moment exceeds that in stoichiometric TbIG, which explains the increase in T_{comp}. This is consistent with previous measurements of the Bi:TbIG system where it was found that reducing

the Tb:Fe ratio to 0.48 through the addition of Bi caused a reduction in T_{comp} to 183K[139] because the magnetization of the dodecahedral plus octahedral sublattice was reduced with respect to that of the tetrahedral sublattice.

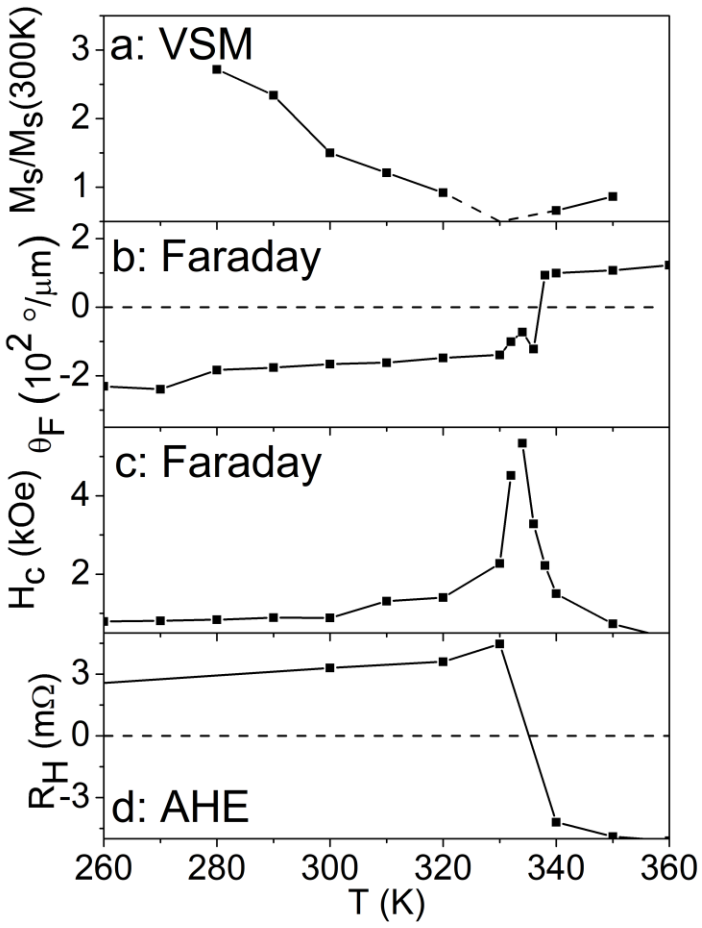

Figure 3.5. Temperature-dependent measurements of (a) magnetic moment, (b) Faraday rotation, (c) coercivity, and (d) AHE-like SMR amplitude. All of these techniques agree on a magnetic compensation point of ~335K.

3.5 Conclusion

Epitaxial EuIG and TbIG thin films were grown using PLD on GGG and SGGG substrates. All films (from 10-60nm thickness) were fully strained to the substrate lattice parameter, with the TbIG film exhibiting in-plane compressive strain on GGG and in-plane tension on SGGG, and the EuIG exhibiting in-plane compression on GGG. The EuIG/GGG (111) and (100) and the TbIG/GGG (111) films exhibit PMA. XRD indicates high crystal quality although the films were deficient in Fe, and the excess RE cations are believed to be accommodated in the octahedral sites. For TbIG, the increase in average magnetic moment of the octahedral sites is responsible for the increase in compensation temperature of the films compared to bulk, measured by magnetometry, Faraday rotation and SMR. This composition-dependent compensation temperature provides a method for adjusting the properties of the film to enable the temperature-dependence of spintronic properties to be characterized.

Pt/(Tb,Eu)IG heterostructure Hall bars showed the existence of SMR at the metal/garnet interface. The imaginary part of the spin mixing conductance of these heterostructures was of the same order of magnitude as that of the previously-studied Pt/TmIG system, with values ranging from 4.6 to 5.4×10^{12} $\Omega^{-1}m^{-2}$. Also, G_i was similar between Pt/EuIG (001) and Pt/EuIG (111), in contrast to past work on Pt/CFO. FMR measurements of EuIG (111) were also performed, giving the first measurement of the Gilbert damping parameter. These RE garnets exhibit promise for future spintronic experiments and applications that require ferrimagnetic insulators with PMA for different crystal orientations or with both PMA and a magnetic compensation point.

3.6 Methods

Thin Film Fabrication and Characterization: All thin films were deposited using pulsed laser deposition (PLD) on single-crystal GGG and SGGG substrates. The EuIG and TbIG targets used were fabricated in-house by mixing Eu_2O_3, Tb_4O_7, and Fe_2O_3 powders in the proper weight ratios with a ball mill, calcining the green body at 1150˚C for 5 hours, re-grinding the powders, and sintering at 1350˚C for 10 hours. The single-phase iron-garnet nature of the targets were confirmed with X-ray diffraction. The growth conditions used were a substrate backside temperature of 900˚C, a laser fluence of 1.3 J/cm^2, a laser repetition rate of 10 Hz, and an O_2 pressure of 150 mTorr. After the deposition, the samples were cooled back to room temperature at a rate of 20˚C per minute in 150 mTorr O_2 (slower cooling was not found to be necessary to increase sample quality). AFM RMS roughness measurements were carried out in a Digital Instruments Nanoscope IV with a 1μm x 1μm scan size, XRD measurements were carried out in a Bruker D8 Discover HRXRD, and VSM measurements were carried out in an ADE 1660 VSM.

Compositional Characterization: A Thermo Scientific K-Alpha+ system was used to take high-resolution XPS spectra for compositional analysis. Prior to data acquisition, a mild argon cluster cleaning procedure was used to remove adventitious carbon without affecting film stoichiometry. High-resolution data was acquired with a 50 eV pass energy. Data analysis was accomplished by comparing integrated peak areas in CasaXPS. The ALTHERMO1 relative sensitivity factor database was used to correctly weight the atomic ratios.

Hall Cross Fabrication: Hall crosses of two different sizes (100 μm and 50μm widths) were fabricated in a two-step lithography process. This process is the same as that described in Chapter 2, except that a negative resist (AZ5214) was used instead a positive resist.

FMR: Broadband FMR measurements were performed using a NanoOsc Phase FMR spectrometer and 200 μm wide coplanar waveguide. The sample is subjected to a DC magnetic field H along the film plane, in addition to a small time-varying microwave excitation field perpendicular to it. The frequency f varies from 3 to 6 GHz in steps of 0.5 GHz. For each value of f, H is swept from 4500 Oe to 0 Oe in order to saturate the sample and then find the resonance value H_{res} and the linewidth ΔH, by fitting the detected voltage with the derivative of the sum of a symmetric and an antisymmetric Lorentzian:

$$P = \frac{d}{dH}\left[\frac{S\Delta H^2 + A_S(H - H_{res})}{4(H - H_{res})^2 + \Delta H^2}\right] \qquad [7]$$

S and A_S are arbitrary fitting constants. In order to minimize systematic errors arising from miscalibration of Hall sensor the values of H_{res} were averaged with H in opposite directions.[140]

3.7 Appendix

1. Extraction of Anisotropy Field for Magnetically Hard Garnets

   While this work was under revision, one of the reviewers commented that we should try saturating the TbIG sample in our SQUID magnetometer (max field = 7 T) because it could produce a higher field than our VSM (max field ~ 1 T). We did this and it became apparent that the GGG background signal made extraction of the anisotropy field impossible.

   Room temperature data is given in Figure 3.A1 which shows a large signal that is linear up to about 50 kOe. To clarify whether the apparent saturation originates from the TbIG film or the substrate, we also measured the film and a bare substrate at 70K as shown in Figure 3.A2. These curves exhibit the same “saturation” behavior at ~50 kOe as the film did at 300K. When the substrate curve is subtracted from the film plus substrate curve, the

resulting M(H) is approximately linear though with increasing noise at high field. From this, it is difficult to obtain the in plane saturation field of the TbIG to correctly ascertain the anisotropy field of the TbIG film.

Since the TbIG properties are determined by the lattice mismatch with the GGG, it is not practical to measure a representative anisotropy field on a TbIG sample grown on a different substrate with lower paramagnetic signal such as YAG. Alternatively, an in-plane electrical measurement could be done at high fields, but our system does not enable high fields to be applied.

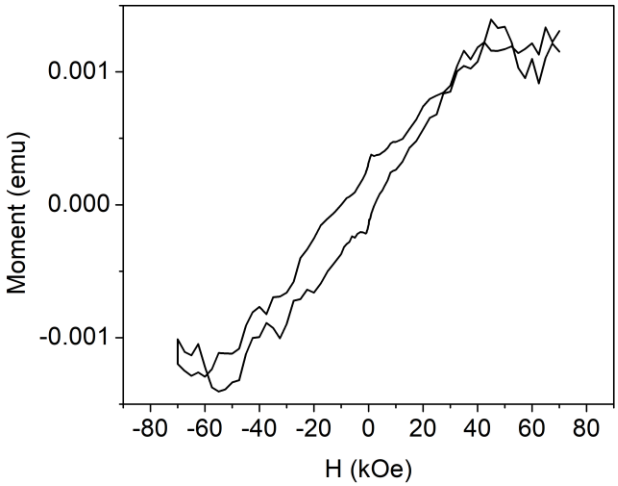

Figure 3.A1: In-plane hysteresis loop (300K) of TbIG/GGG film analyzed in manuscript

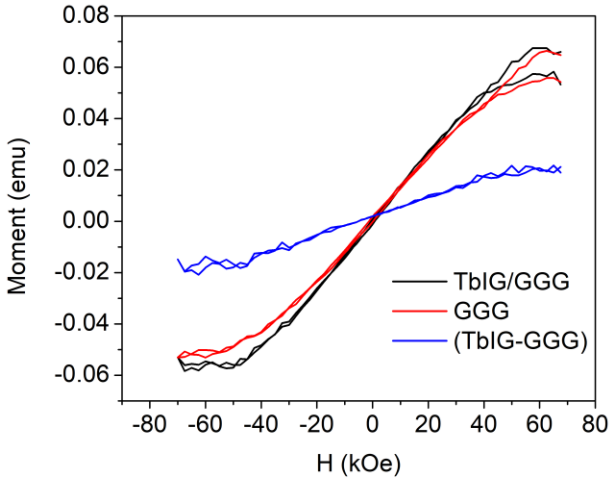

Figure 3.A2: Representative in-plane hysteresis loops conducted at 70K

2. Macrospin Fitting of EuIG (111) SMR Data

As the author continued his thesis work, it became apparent that the estimates of H_K given in Table 1 were in fact lower bounds due to the GGG substrate signal's nonlinearity. To obtain a better estimate, in-plane SMR measurements of a Hall cross on a (111) Pt/EuIG/GGG Hall cross were carried out. A macrospin model was coded in Python (adapted from http://ferroelectronicslab.com/2016/10/14/useful-programs/) in which the equation

$$0 = \sin\big(2(\theta - \theta_0)\big) + \frac{BM_s}{2K_u}\sin(\theta) \text{ [A1]}$$

was solved for every field point. In this equation, θ is the angle between the magnetization and the applied field, θ_0 is the angle between the easy axis and the applied field, B is the magnetic flux density, and K_u is the uniaxial anisotropy *including shape anisotropy*. To pre-process the data, the ordinary Hall effect and the Hanle magnetoresistance[10] were removed by fitting to a linear and a parabolic function, respectively. Also, the forward and reverse branches of the data and the fit were averaged together to eliminate hysteretic behavior. The results of the fit are presented in Figure 3.A3.

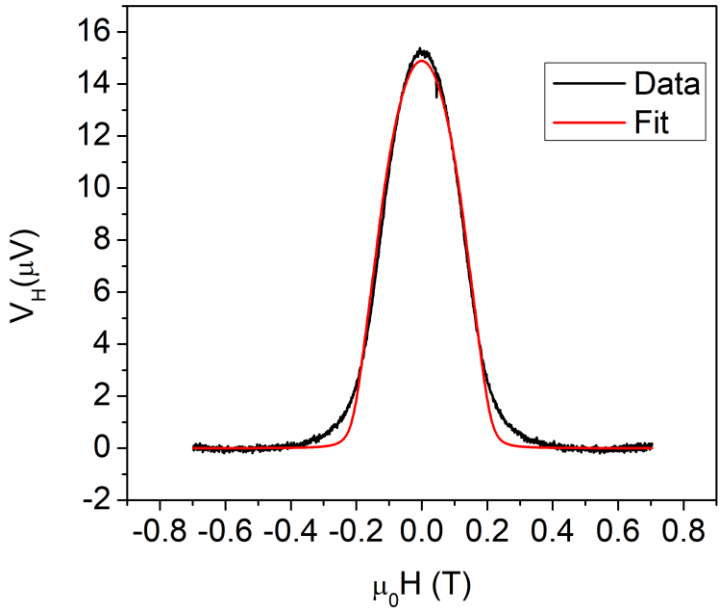

Figure A3: Macrospin fit of SMR data taken from a (111)-oriented Pt/EuIG/GGG Hall cross

The fit to the data gives a $K_{u,eff}$ value of 10637 J/m^3. When the shape anisotropy contribution is subtracted, we get K_u = 18240 J/m^3. This yields a new estimated λ_{111} of 8.085E-6. This is still higher than the bulk λ_{111} of EuIG, so the main conclusions of this chapter remain unchanged. Also, the new saturation field of the (001)-oriented EuIG was greater than the 10 kOe maximum field of our SMR setup, meaning that λ_{001} is actually far greater than what was reported in Table 1. Again, this does not change the main conclusions of this chapter.

3. Quantification of Tb $3d_{5/2}$ XPS peak

In order to get a rough idea of the charge defects present within our TbIG, we performed a quantification of the Tb $3d_{5/2}$ XPS peak in Figure 3.2 of the main text. Quantifying Tb XPS is made difficult by the dearth of good references in the literature. The reference used in the main text was Balaguer *et al*[122]; however, this reference included an extra peak within

the main $3d_{5/2}$ peak without explaining its origin or constraining its FWHM. In our fit we opted to include a single Tb^{4+} component and a single Tb^{3+} component as well as their corresponding satellites. This was supported by a recent thesis dealing with multivalent Tb XPS[141]. Fitting was done in the Thermo Scientific AVANTAGE software with a "Smart" background. The satellite peaks and main peaks were constrained to have FWHMs within 0.1eV of each other, respectively. The peak area ratio calculated by this method was Tb^{4+}:Tb^{3+} = 1:0.9.

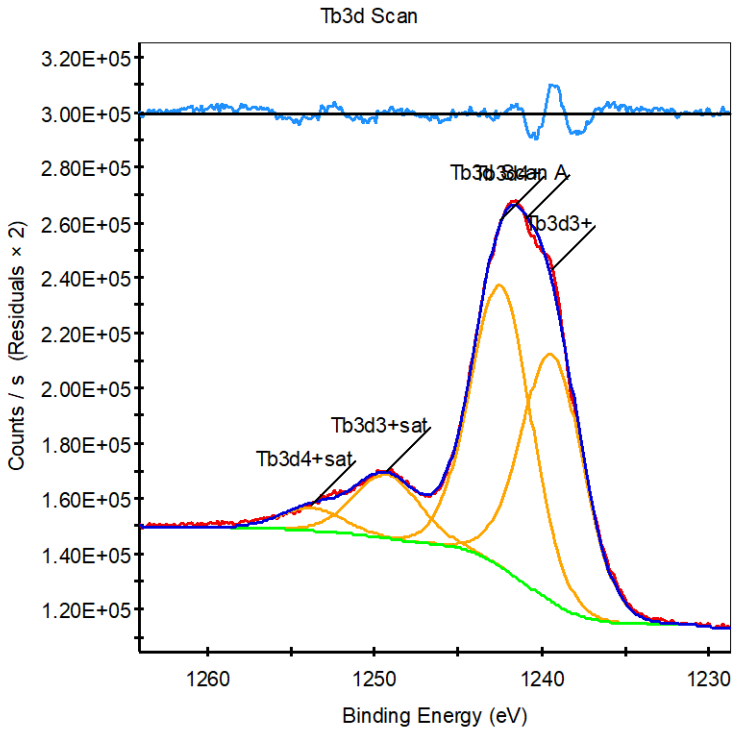

Figure 3.A4: Quantification of $3d_{5/2}$ peak from main text.

Peak	Binding Energy (eV)	FWHM (eV)
Tb^{3+}	1239.34	4.56
Tb^{4+}	1242.42	4.46
Tb^{3+} satellite	1249.28	4.76
Tb^{4+} satellite	1242.42	4.66

Table 3.A1: Tb XPS quantification results

Chapter 4

The Effects of Point Defects on the Compensation Temperature of TbIG

This chapter follows up on the unexpected result from Chapter 3 which found that the T_{comp} of TbIG thin films was ~80 K higher than its value in bulk TbIG. Here we propose a model involving point defects which explains this result. E.R. Rosenberg synthesized the TbIG thin film sample, analyzed the XMCD data (with the help of Dr. J. Freeland, J. Bauer, Dr. J. Pelliciari, and C. Occhialini), collected and analyzed the XPS data (with the help of L. Shaw), and collected the T_{Curie} data. J. Bauer synthesized the TbIG thin film sample, wrote and executed the molecular field model, and collected the TbIG bulk T_{comp} data.

4.1 Introduction

The higher-than-bulk compensation temperature of the TbIG thin films in the previous chapter presents a puzzle – what causes it to be so drastically elevated? Interestingly, TbIG is not the only PLD-grown garnet for which T_{comp} is different than previously reported bulk values. In 2019, TmIG was reported to exhibit a compensation temperature of 75K[142]. This contradicts previous reports of bulk and thin-film TmIG with no compensation temperature[32,53]. A similar discrepancy in compensation temperature was discovered in DyIG: bulk DyIG has a compensation temperature of 220K[32] while PLD-grown single-crystal DyIG has been reported with a compensation temperature of 190K[62]. PLD-grown polycrystalline GdIG shows a T_{comp} of 377K, approximately 100K higher than bulk GdIG[143]. However, other recent studies have reported PLD garnets *with* bulk-like compensation points, such as polycrystalline DyIG[62] and even TbIG (in contradiction to our results)[144].

It would be useful to know why these discrepancies occur in order to better control the compensation temperature of materials such as TbIG. This is technologically important because compensated metallic ferrimagnets have shown ultrasmall and ultrafast spin textures[27] and efficient spin orbit torque switching[28]. More recently, compensated insulator ferrimagnets have shown ultrafast domain wall velocities[145], enhanced magnon-magnon coupling[146], and noncollinear magnetism[147]. In ideal rare-earth (RE) iron garnets, magnetic RE ions sit on dodecahedral sites while Fe ions sit on octahedral and tetrahedral sites, and the net magnetic moment is due to $(RE+Fe_{oct}) - Fe_{tet}$ (see Chapter 1). Therefore, defects within the material that affect these sublattice magnetizations can cause significant changes in the compensation temperature. For example, diamagnetic substitution of Ga onto the tetrahedral site of YIG has been shown to cause the appearance of a compensation temperature[148], while growth-induced depletion of Gd in GdIG due to the precipitation of a Gd_2O_3 secondary phase in sputtered films caused the already extant T_{comp} of the material to rise[149].

Recalling our hypothesis from the previous chapter – that off-stoichiometry, vacancies, and antisite defects are responsible for the elevated T_{comp} in our TbIG thin films, we must determine how the Fe ions are distributed between the octahedral and tetrahedral sites in the lattice, whether there is any Fe^{2+} present, and whether antisite defects (e.g. Tb^{4+} on octahedral sites) exist. This information is difficult (if not impossible) to answer using the XPS data presented earlier, so a different technique must be used. In this chapter, we use a multi-faceted approach to determine the cause of the elevated compensation temperature of TbIG. First, we extract the site occupancies of bulk and thin-film TbIG by fitting XMCD data with a relativistic Hartree-Fock model augmented by crystal field theory. Then, by feeding the experimentally measured site occupancies into a molecular field

model, we propose a model that synthesizes the experimental data regarding site occupancy and compensation point.

4.2 Extracting Site Occupancies Via XAS/XMCD

In the 1960s, Robert D. Cowan wrote the RCG-RAC ab-initio Hartree-Fock code. This code calculated the energy levels and emission spectra of isolated atoms. Then, in the 1990s, Theo Thole[150] updated it by adding Butler's group theory formalism[151] so that it could be used to calculate the XAS spectra of ions in coordinated lattice sites and in an exchange field. This software package, which in its current form is known as TT-Multiplets and is maintained by Prof. Frank de Groot, is able to calculate the XAS and XMCD spectra of transition metals with site and magnetic sublattice specificity.

The method of fitting experimental XMCD data with TT-Multiplets was developed in the 1990s and 2000s. It was successfully applied to the spinel system, with accurate quantifications of iron valence and site occupancies extracted from materials such as magnetite and cobalt ferrite[152–154]. The power of this technique is that the Fe XMCD L edge contains three main peaks which can be uniquely mapped back to the spectral fingerprints of different Fe species such as Fe^{3+} Oh, Fe^{2+} Oh, and Fe^{3+} Td (see Figure 1). By adding these component spectra together, a linear combination fit to an experimental spectrum can be accomplished through the method of nonlinear least squares. In this section, we will describe how this method may be applied to garnet materials such as terbium iron garnet.

Circularly polarized XAS TEY data from a terbium iron garnet thin film (comparable to the one described in previous sections) and from a bulk terbium iron garnet polycrystal was taken at the 4-ID-C beamline at the Advanced Photon Source in Argonne National Laboratory and is displayed

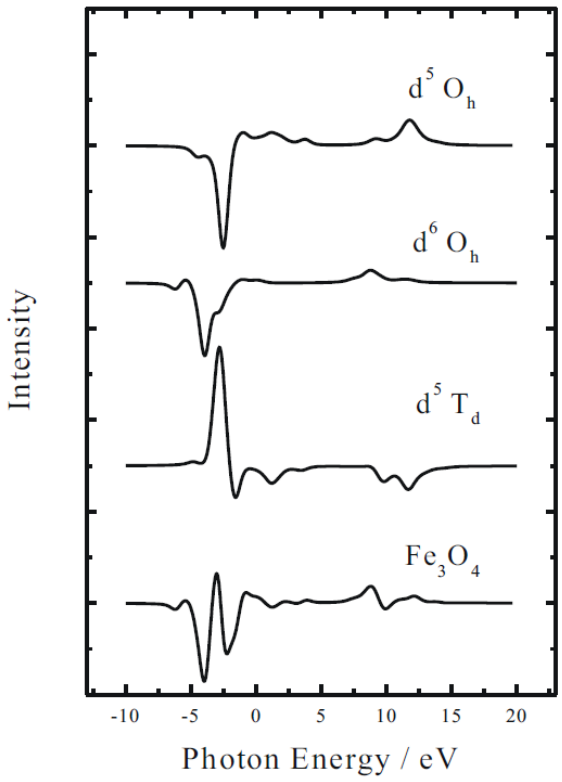

Figure 4.1: Example of fingerprinting an iron oxide sample using TT-Multiplet simulations of XMCD spectra. Reprinted from Pattrick *et al* 2002[155]

in Figure 2. The bulk-like compensation temperature of the polycrystal was confirmed using VSM (see Figure 3). Also, the defect-free nature of the bulk polycrystal was verified by powder XRD and subsequent Rietveld refinement (see Appendix). The data was shifted to match an internal Fe foil reference so that the energy scales for the bulk and thin film data would agree. The bulk sample was a sintered ceramic synthesized by the method cited in chapter 3, and the TbIG thin film was a 52nm thick film grown by the method cited in chapter 3.

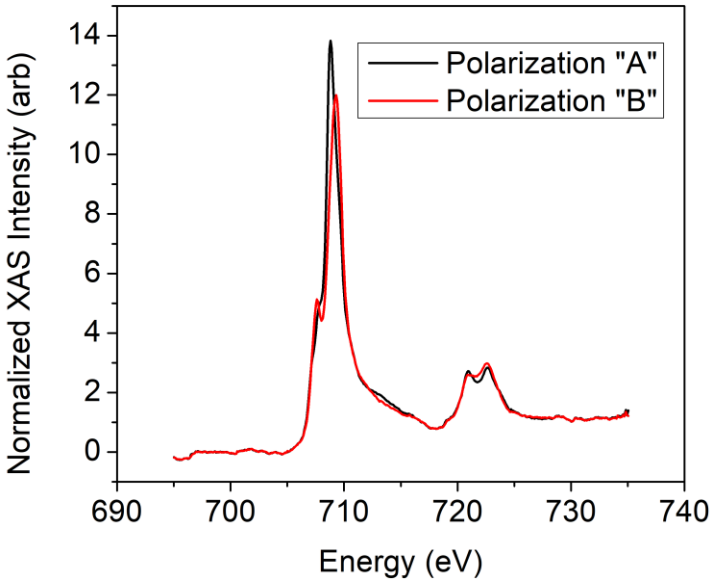

Figure 4.2: Normalized XAS data from LHCP and RHCP light, taken from a TbIG thin film similar to what was studied in the previous chapter. The difference in the spectra is the origin of XMCD.

The XAS data was normalized using Athena and the LHCP and RHCP spectra from data collected at remanence from positive and negative fields were subtracted using the formula:

$$XMCD = \frac{(\sigma_{\downarrow\uparrow} + \sigma_{\uparrow\downarrow}) - (\sigma_{\uparrow\uparrow} + \sigma_{\downarrow\downarrow})}{2} \quad [1]$$

in order to eliminate any nonmagnetic artifacts (see Figure 4). In [1], σ_{ij} is the data collected with the i^{th} polarization and the j^{th} magnetic field direction. Then, the data was fitted using a custom interface to the TT-Multiplets Hartree-Fock package. To accomplish this fitting, the experimental XMCD L_3 edge (between approximately 705 and 713 eV) was fit using nonlinear least squares to the expression:

$$XMCD_{exp} = a(f_1 XMCD_{Fe^{3+}Oh} + f_2 XMCD_{Fe^{3+}Td} + f_3 XMCD_{Fe^{2+}Oh}) \quad [2]$$

where a is an overall scaling parameter, f_i is the fraction of the i^{th} spectral component, $XMCD_{exp}$ is the experimental XMCD spectrum, and $XMCD_{Fe^{3+}Oh}$ (for example) is the simulated XMCD spectrum, calculated using TT-Multiplets, for Fe^{3+} ions sitting on an octahedral site. It is important to note that the f_i are not necessarily the true site occupancies of the Fe ions. However, because we have a bulk reference standard, we can *compare* the f_i of our thin film sample to a "perfect" TbIG crystal with a 2:3 octahedral:tetrahedral Fe ratio (confirmed with Rietveld refinement; see Appendix).

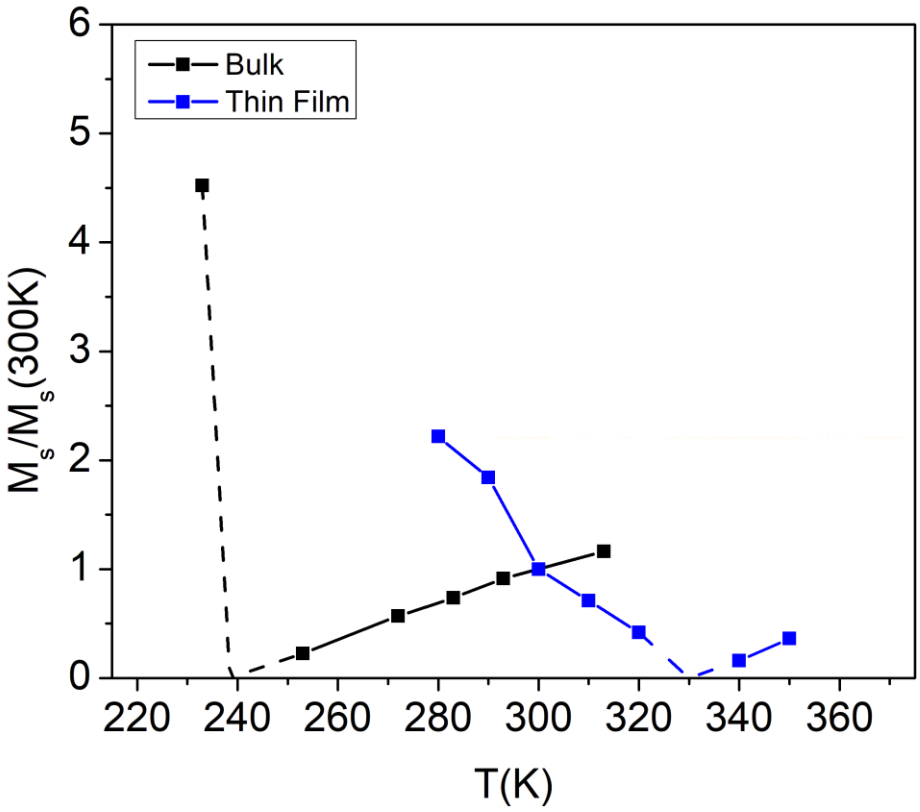

Figure 4.3: Comparison of bulk and thin-film compensation temperature, measured by VSM. The bulk sample shows a similar compensation temperature to what has been reported in the literature.

The important fitting parameters are the Gaussian and Lorentzian broadening, the crystal field, the chemical shift, the Slater Integral reduction, and the exchange energy. The author is indebted to Prof. Frank de Groot and Dr. Johnny Pelliciari for their help in deciding on physical values for these parameters.

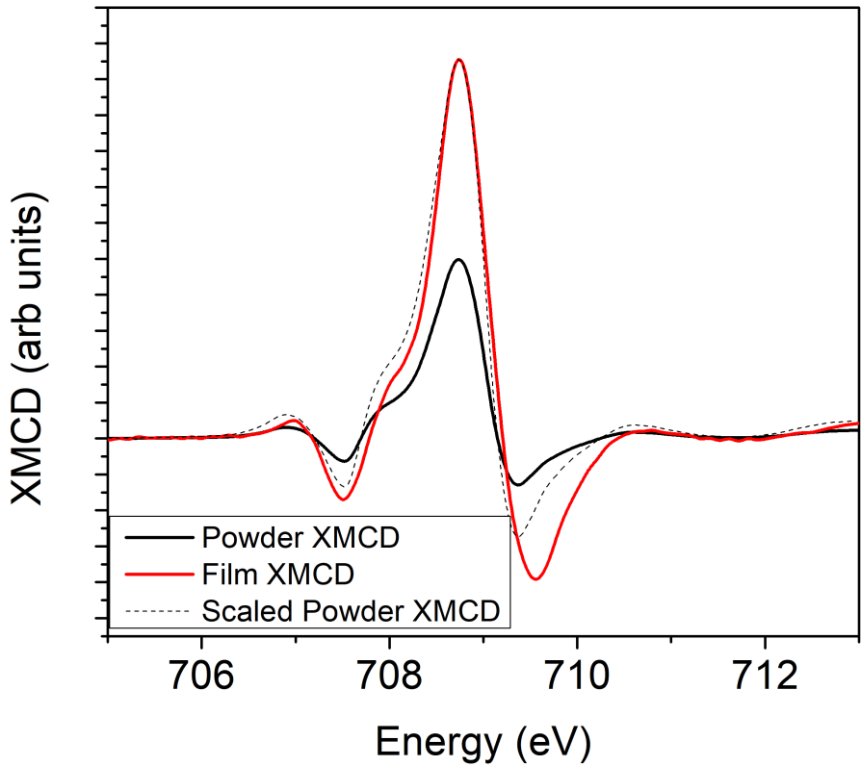

Figure 4.4: Normalized XMCD data (zoomed in to the region that was fitted with TT-Multiplets) from the bulk (powder) and thin film TbIG samples. The dotted line is the powder XMCD spectrum, scaled to show differences between the thin film and powder spectra on the same axes.

Gaussian and Lorentzian Broadening: The Gaussian broadening is due to the energy resolution of the synchrotron, which is known to be 0.1eV for the APS [private communication with Johnny]. The Lorentzian broadening is somewhat more complex, as it is due to fundamental relaxation

processes in the material[156]. Some groups have noted that an energy-dependent broadening may be appropriate[157], while others use 0.2eV for the entire L3 edge. We chose to use the latter method so as not to overfit the data[158].

Crystal Field: The crystal field is the Coulomb interaction due to the oxygen ions nearest to the Fe ion in question. In terbium iron garnet, two crystal field symmetries are possible: octahedral (Oh) and tetrahedral (Td). These two symmetries are parametrized by the same crystal field parameter, known as 10Dq. An octahedral/tetrahedral crystal field causes the five Fe 3d states to split into a doublet e_g and a triplet t_{2g}, and the energy between these two degenerate sets is 10Dq[23]. In a tetrahedral symmetry, 10Dq is negative while it is positive for an octahedral symmetry. In materials for which the bond lengths between the two types of polyhedra are identical, it is possible to derive that 10Dq(oct)/10Dq(tet) = -9/4[159]. However, in garnets this is not necessarily true so this cannot be used as a good constraint[159]. Ballpark values were extracted from Liu 2017[160] and final values were obtained by least squares fitting. The exact values of 10Dq are not crucial, as the spectral shape varies slowly with 10Dq[158].

Slater Integral Reduction: The original Cowan codes calculate spectra for isolated ions (that is, systems with perfectly flat bands). Part of this complex many-body calculation is the calculation of direct and exchange interactions between electrons. These matrix elements are known as Slater integrals[161]. For instance, in a $1s^1 2s^1$ configuration, the Coulomb energy of the ^1S configuration is $\langle {}^1S|e^2/\mathbf{r}_{12}|{}^1S\rangle = F^0(1s2s) + G^0(1s2s)$ where F^0 and G^0 are the direct and exchange Slater integrals. When the atoms are embedded in a coordination structure, the overall effect is to reduce the Slater integrals. Often, a reduction to 80% of atomic values are used. However, in this work values optimized for garnets from a recent study on Ce:YIG were used[162].

Exchange Energy: The exchange energy is not a crucial fitting parameter and is only included as an additional symmetry breaking to allow the simulation of the XMCD. If the simulations are carried out at elevated temperature the exchange energy value affects the lineshape, but all simulations in this chapter were carried out at 0K[158].

The final fitting parameter values are displayed in Table 4.1. The fit curves obtained with these values are displayed in Figure 5. With this choice, the thin film and bulk site occupancies were extracted (Table 4.2).

Parameter	Value	Source
10Dq [Fe^{3+}Oh]	1.8 (thin film), 1.7 (bulk)	Fitting
10Dq [Fe^{3+} Td]	-0.8 (thin film), -0.7 (bulk)	Fitting
10Dq [Fe^{2+} Oh]	1.0	Fitting
M [Fe Oh]	-12meV	Vasili *et al*[162]
M [Fe Td]	18meV	Vasili *et al*[162]
Fdd	0.85 [Oh], 0.75 [Td]	Vasili *et al*[162]
Fpd	0.9625	Vasili *et al*[162]
Gpd	0.975	Vasili *et al*[162]

Table 4.1: Fitting parameters used in Hartree-Fock simulations of TbIG thin film and bulk samples

Species	TbIG Thin Film	TbIG Bulk
Fe^{3+} Oh	0.29820+/-2E-5	0.28265+/2E-5
Fe^{3+} Td	0.67124 +/-1E-5	0.69131+/-1E-5
Fe^{2+} Oh	0.03067 +/-1E-5	0.02605+/-1E-5
Oh:Td Ratio	0.602	0.66

Table 4.2: Best-fit site occupancies of TbIG thin film and bulk samples, extracted via TT-Multiplets fitting. The bottom row is the corrected Oh:Td ratio taking into account that the bulk TbIG has a 2:3 ratio (confirmed by Rietveld refinement)

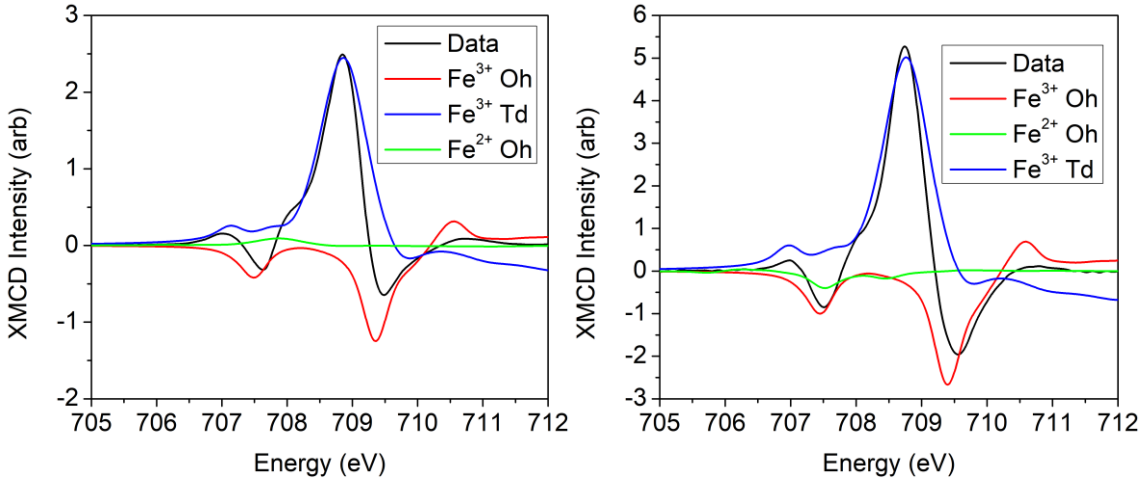

Figure 5: Best fit calculated XMCD spectra (left is bulk, right is thin film), broken up into spectral components. The simulation parameters used are displayed in Tables 1 and 2.

The fitting of the XMCD data suggests that the TbIG thin film has a similar site occupancy ratio to the TbIG bulk sample, although it has a 10% lower Oh:Td ratio. This can also be seen by visually inspecting the XMCD spectra, as the octahedral peak is larger in the thin film than in the bulk. This implies that, even though the TbIG film is iron-deficient, the iron vacancies are not overwhelmingly on a single type of site but rather are distributed evenly between the octahedral and tetrahedral sites. Also, our analysis reveals that there is a relatively small amount of Fe^{2+} present – between 2 and 3% of the total iron content. However, XPS peak deconvolution reveals that a large fraction of the Tb present is in the 4+ state. The fitted XPS peak area ratio of Tb^{4+}:Tb^{3+} is 1:0.9, implying that 52.6% of the Tb is in the 4+ state (see Appendix of chapter 3) This implies that iron vacancies are necessary to maintain electroneutrality with the large amount of Tb^{4+} present. Interestingly, high-resolution XPS measurements on the bulk TbIG sample reveal that the Tb 4d peak shape is identical to that of the thin film, implying comparable levels of Tb^{4+}. The best-fit XMCD results also show low levels of Fe^{2+} in the bulk sample, raising questions about how charge is compensated in this sample.

4.3 Molecular Field Simulations of TbIG with Point Defects

In order to form a hypothesis about how these point defects impact the magnetic compensation point, molecular field simulations were carried out following the formalism originally developed by Dionne (See chapter 1)[23]. Two classes of simulations were performed. In the first class, the Tb:Fe ratio was varied by introducing Fe vacancies without allowing Tb to sit on Fe sites. In the second class, the Tb:Fe ratio was varied by introducing Fe vacancies and Tb was allowed to sit on octahedral Fe sites. XMCD cannot distinguish between octahedrally and dodecahedrally coordinated terbium ions due to lifetime broadening[158], so the simulations of the second class were

repeated assuming that 15%, 25% and 50% of the octahedral vacancies were filled by terbium ions. The results of these simulations are shown in Figure 6.

It is apparent from the simulations of the first class that iron vacancies alone are not enough to move the compensation temperature to our observed value of 335 K – at the XPS-derived composition of Tb:Fe = 0.86 (see Appendix), the calculated compensation temperature is below 330 K.

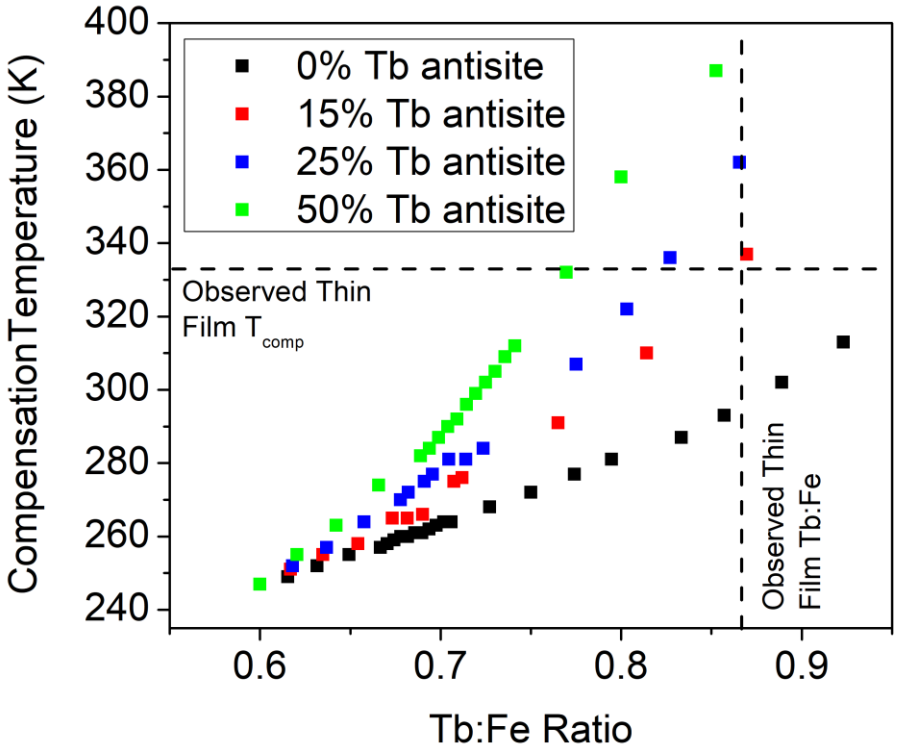

Figure 6: Simulated compensation temperatures for terbium iron garnet with different Tb:Fe ratios and Tb antisite defect concentrations.

The simulations of the second class show higher compensation temperatures at our observed composition, with the true level of substitution likely lying around 15%. However, it is important to note that if terbium antisite defects exist, it is unclear what their superexchange interaction

strength would be, as this has not been studied in the literature. Our assumption was that the exchange interaction for Tb(oct) was the same as for Tb(dod), but this is not necessarily true. Changing J_{ij} for terbium antisite defects would further impact the compensation temperature.

With this caveat in mind, we conclude that a good hypothesis for the elevated compensation temperature of our TbIG thin films is a combination of tetrahedral iron vacancies and octahedral terbium antisite defects. Quantification of the octahedral Tb superexchange interaction and direct observation of these point defects with a technique such as resonant x-ray diffraction would aid in the acceptance or rejection of this hypothesis.

4.4 Curie Temperatures of Bulk and Thin Film TbIG

Our current hypothesis is that tetrahedral vacancies are partly responsible for the elevated compensation temperature of our TbIG thin films. An additional piece of evidence for the existence of cation vacancies can be provided by Curie temperature (T_{Curie}) measurements. In the past, T_{Curie} measurements were used to determine the effects of nonmagnetic substitution onto the iron sites of YIG[23], as dilution of YIG by nonmagnetic elements causes a reduction in T_{Curie}[23,163,164]. We therefore collected magnetometry data between 358 K (above the compensation temperature of the thin film) and T_{Curie} for the thin film and bulk samples discussed earlier. These results are displayed in Figure 7. The thin film sample exhibits a Curie temperature approximately 40 K lower than the bulk sample, lending more credence to the existence of cation vacancies in the film.

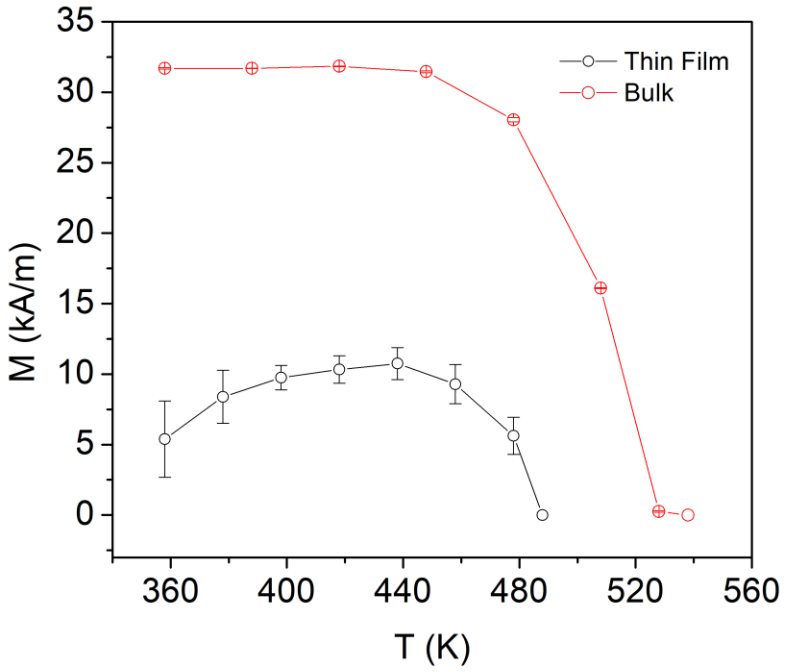

Figure 7: M(T) data taken in the vicinity of the Curie temperatures of the TbIG thin film and bulk samples considered in this chapter. The T_{Curie} of the thin film sample is approximately 40 K lower than the T_{Curie} of the bulk sample.

However, the T_{Curie} of the bulk sample is also lower than the reported T_{Curie} of ~550 K[23]. Therefore, some level of iron vacancies may exist within the bulk sample, even though the Rietveld refinement was unable to detect them. This may explain the mechanism by which Tb^{4+} in the bulk sample is charge-compensated. More sensitive methods such as resonant x-ray diffraction may shed light on this question.

4.4 Conclusion

In this chapter, we have proposed a model that explains the higher-than-bulk compensation temperature of TbIG that was observed in chapter 3. By performing XMCD measurements on thin film and bulk samples of TbIG, we concluded that the octahedral-to-tetrahedral iron ratio was

similar between the two samples. XPS survey scans showed that the composition of the TbIG thin film was strongly iron-deficient (Tb:Fe = 0.86), so we proposed that the nonstoichiometry was accommodated through some combination of Tb antisite defects and Fe vacancies. By using molecular field models and the assumption (derived from XMCD and Rietveld refinement) that the oct:tet iron ratio was 2:3, we determined that incorporating Tb antisite defects (i.e. Tb sitting on octahedral sites) was sufficient to explain the observed compensation temperature trend while simply incorporating iron vacancies was not sufficient. The T_{Curie} of the thin film was found to be lower than the bulk, providing more support for the hypothesis that iron vacancies exist in the film.

The question of charge neutrality still remains somewhat open. In order for TbIG to remain charge-neutral with large amounts of Tb^{4+}, either Fe^{2+} or Fe vacancies must be present. For the thin film this is consistent with our hypothesis: XMCD did not find significant levels of Fe^{2+}, and the lowered T_{Curie} provides support for vacancies. However, high-resolution XPS scans of the Tb 4d edge showed identical peak shapes between the thin film and bulk samples, implying that our bulk TbIG also contains a large fraction of Tb^{4+} ions. This is despite XMCD not finding a significant Fe^{2+} content and the Rietveld refinement finding no significant vacancy content. So the question remains: how is charge balanced in the bulk TbIG sample? A technique more sensitive to point defects, such as resonant x-ray diffraction, could answer this question and provide direct evidence for the existence of Tb antisite defects.

Appendices

1. Verification of Quality of Polycrystalline Bulk TbIG

   In order to ensure that the polycrystalline bulk TbIG sample used in this chapter was of good quality, a Rietveld refinement was carried out using the Panalytical HighScore Plus software. A piece of the sample was ground in a mortar and pestle, mounted on a glass slide, and measured in a Rigaku Smartlab XRD system. The XRD scan is depicted in Figure 4.A1.

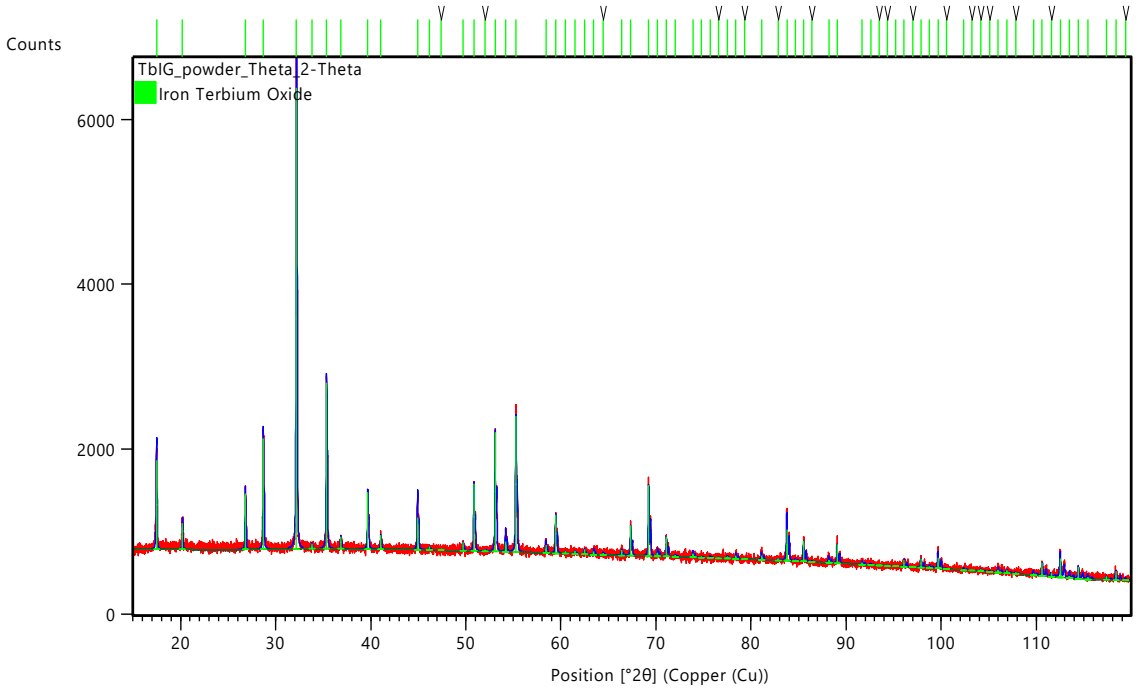

Figure 4.A1: Rietveld profile fit from polycrystalline bulk TbIG powder sample

The Rietveld refinement of the XRD spectrum showed that, within a 1% uncertainty, the iron site occupancies of the TbIG bulk sample were those of a perfect bulk TbIG crystal (i.e. 2:3 Oh:Td). Therefore, we are justified in using it as a reference in the XMCD section of this chapter.

2. XPS of Thin Film and Bulk TbIG Samples

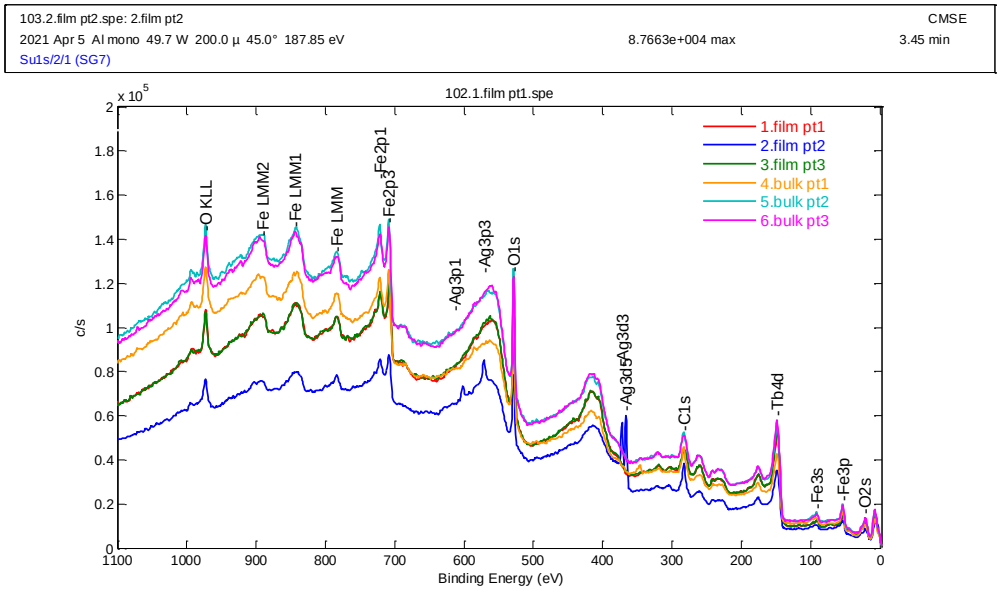

Figure 4.A2: XPS survey scan from thin film and bulk TbIG samples. The Ag peak from film point 2 is due to silver paste used to make contact during XAS measurements

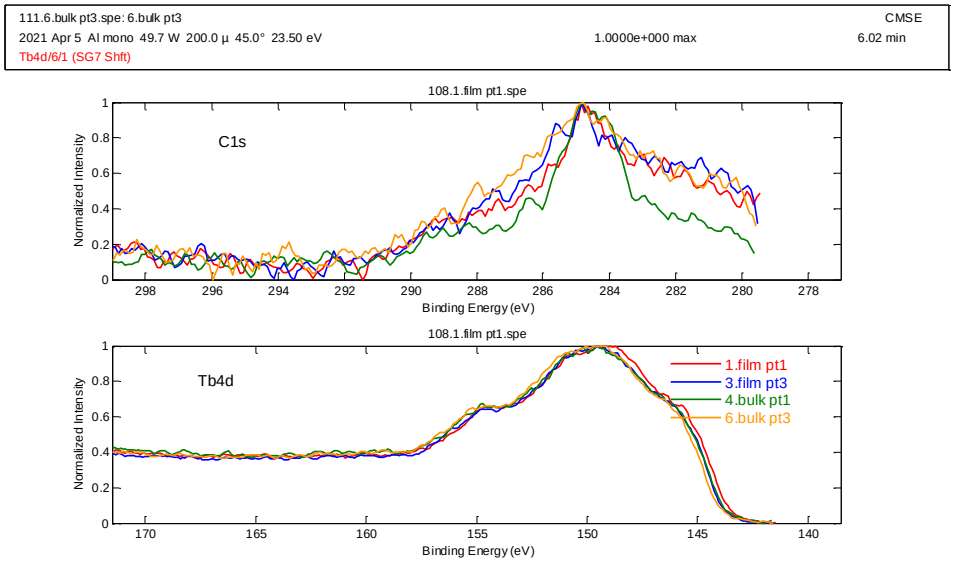

Figure 4.A3: High-resolution XPS of the Tb 4d peak in bulk and thin film TbIG samples. The identical peak shapes imply similar Tb^{4+}:Tb^{3+} ratios in both samples

Chapter 5

Magnetic Properties and Growth-Induced Anisotropy in Yttrium Thulium Iron Garnet Thin Films

This chapter is taken from an article which, at the time of writing, has been submitted to Physical Review Materials. It has been reprinted here in its entirety. E.R. Rosenberg wrote the manuscript, grew the films, collected/analyzed the XRD, VSM, and MOKE data, and developed the g-factor model. K. Litzius and E.R. Rosenberg built the MOKE microscope. G. A. Reilly and J.M. Shaw collected and analyzed the FMR data. H. T. Nembach, G. S. Beach, and C. A. Ross supervised the research.

5.1 Introduction

With the advent of vapor-phase growth methods for preparing thin epitaxial oxide films, including pulsed laser deposition (PLD) and sputtering, thin films of rare earth (RE) iron garnet materials (REIG, formula unit $RE_3Fe_5O_{12}$) have been developed with desirable properties for spintronic applications, including thulium (TmIG), terbium, europium, samarium and other REIG films with perpendicular magnetic anisotropy (PMA). Spin-orbit torque switching,[10,14] chiral spin textures[11,13,16], and a relativistic domain wall velocity approaching the magnon group velocity have been reported in Pt/TmIG and Pt/Bi:YIG heterostructures, making these materials promising candidates for memory or logic devices[11–13,15].

REIG materials are well-characterized, with studies having been performed from the 1950s to the present day. REIG materials have three magnetic sublattices, comprised of 3 RE^{3+} ions per formula unit (FU) on dodecahedral (*c*) sites, 2 Fe^{3+}/FU ions on octahedral (*a*) sites, and 3 Fe^{3+}/FU ions on tetrahedral (*d*) sites[32]. The strongest superexchange coupling is an antiferromagnetic interaction between the tetrahedral and octahedral iron. The dodecahedral moments are also coupled antiparallel to the tetrahedral iron, and hence the three sublattices form a collinear ferrimagnet, with the Fe^{3+} d ions opposing the combined moment of the RE^{3+} *c* and the Fe^{3+} *a* ions[32], though noncollinear ordering can occur at low temperatures by canting of the RE moments[165].

Substitution of other cations has been explored extensively, with many cations exhibiting a site preference, for instance, Sc^{3+} on the *a* sites, Si on the *d* sites, and almost any RE element as well as yttrium (Y) on the *c* sites[166]. Tuning the magnetic properties of REIG thin films, including the magnetization, anisotropy, coercivity, magnetostriction, compensation temperature and damping, has been investigated through control of the RE ion, the RE:Fe ratio, oxygen content, and substrate strain[43,105,117]. In PLD or sputtered garnet films, PMA can be introduced due to magnetoelastic anisotropy,[43,52,53,105] and has been controlled through strain engineering by varying the substrate epitaxial mismatch strain[43,167] or the thermal mismatch strain[61,62] and by altering the magnetostriction coefficients by fully substituting the RE species on the *c*-site[43,168,169]. PMA of magnetoelastic origin has also been achieved in strained YIG[170] and in Bi-substituted YIG[41], which exhibit lower damping than REIGs, and in garnets with multiple substitutions such as $(Dy,Ce)_3(Fe,Al)_5O_{12}$[171].

In contrast to these vapor-grown garnet films, the PMA in the liquid-phase-epitaxy-grown (LPE) REIG thin films of the late 1900s was attributed primarily to growth-induced anisotropy. This additional anisotropy energy was empirically shown to be a function of the difference in ionic radius between the c-site ions, and was believed to be caused by preferential occupation of inequivalent c sites by different species[18]. The perpendicular anisotropy in PLD-grown Bi:YIG was attributed in part to growth-induced anisotropy[41]. Also, iron vacancy ordering in Fe-deficient PLD-grown YIG was found to cause an additional uniaxial anisotropy[172]. Other than these two studies, there have been scant reports of growth-induced anisotropy in vapor-deposited REIG films[41].

In this article, we describe the composition-dependent magnetic properties of yttrium-thulium iron garnet (YTmIG) thin films grown epitaxially on garnet substrates and demonstrate the presence of

growth-induced perpendicular magnetic anisotropy. By varying the yttrium concentration over a limited range, we can tune the magnetic anisotropy energy and obtain a transition from perpendicular to isotropic to in-plane anisotropy. Magnetooptical Kerr effect (MOKE) microscopy is used to determine the equilibrium domain size and the reversal mode of YTmIG thin films with PMA. Broadband ferromagnetic resonance (FMR) measurements show an increase in the damping and a decrease in the g-factor with increasing Tm content, consistent with the Kittel model for bulk RE garnet crystals. These results demonstrate a method for continuously tuning a variety of REIG static and dynamic magnetic properties on a single substrate for spintronic applications.

5.2 Growth and Structural Characterization

For this study, $Y_xTm_{3-x}IG$ (YTmIG) films ranging from 25 nm to 30 nm in thickness were grown by PLD on (111) gadolinium gallium garnet ($Gd_3Ga_5O_{12}$, GGG) substrates. YTmIG films were also grown on (111) substrates with composition $Gd_{2.6}Ca_{0.4}Ga_{4.1}Mg_{0.25}Zr_{0.65}O_{12}$ (substituted GGG or SGGG). The growth conditions (O_2 pressure, temperature, laser fluence) used were similar to those used in our previous work[11,13,27,43], described in Methods. In order to vary the composition x, YIG and TmIG targets were placed in the deposition chamber and the laser was fired alternately at each for a few shots at a time, keeping the total number of shots per cycle at 35 and the total number of shots per film at 10^4. Thus, the total number of cycles was 285 for the co-deposited films. Film thicknesses were obtained by fitting x-ray reflectometry data. To obtain an estimate of the film composition, the growth rates for YIG and TmIG films were measured for calibration. The YIG growth rate is 1.28 times higher than the TmIG growth rate, so the shot ratios were scaled by this factor to yield nominal compositions. A summary of the samples grown, their thicknesses, and their nominal compositions is provided in Table 5.1.

Table 5.1: Ratios of laser shots and nominal film compositions for Y:TmIG Films

Nominal composition $(Y_xTm_{3-x})Fe_5O_{12}$	**Sample Recipe (Shot Ratio)**	**Shots YIG/cycle**	**Shots TmIG/cycle**	**Film Thickness, nm**
TmIG	0:35 Y:TmIG	n/a	n/a	29
$Y_{0.51}Tm_{2.49}IG$	5:30 Y:TmIG	5	30	29
$Y_{0.83}Tm_{2.17}IG$	8:27 Y:TmIG	8	27	26
$Y_{1.2}Tm_{1.8}IG$	12:23 Y:TmIG	12	23	29
YIG	35:0 Y:TmIG	n/a	n/a	37

In order to characterize the structural properties of these films, high resolution x-ray diffraction (HRXRD) $2\theta-\omega$ symmetric scans about the (444) direction were performed (Figure 5.1a). The high crystalline quality of the samples is evident from the Laue fringes present in each scan. For the films with higher Y concentrations, the film peak was too close to the substrate peak to be fitted by a Gaussian function. Therefore, shear strain values were calculated by fitting both the substrate and film peaks with a commercially available dynamical diffraction software. A model was constructed by considering the film to be an alloy between two hypothetical end-members whose (444) reflections were either to the left or to the right of all of the film peaks studied. Then,

Vegard's law was used to calculate the lattice parameter of the films. By using the rhombohedral-to-hexagonal transformation described in our previous work[43] and making the assumptions that the films are fully strained to match the substrate (i.e., the in-plane lattice parameters of the film and the substrate are equal) and that the unit cell side length is not significantly distorted by the shear strain, the unit cell corner angle β (Figure 5.1b) for each film was calculated. The first assumption is well-justified by our previous work which showed that garnet films on GGG remain pseudomorphic (follow the substrate in-plane lattice parameter) up to thicknesses much greater than 30 nm[43]. The second assumption is well-justified because it conserves unit cell volume to within 0.01%. The shear strain is then equal to $\pi/4 - \beta/2$. The shear strain values and unit cell angles are displayed in Figure 5.1c. Error bars were calculated but were excluded from the figure because they are smaller than the size of the displayed data points.

The lattice parameters of bulk TmIG and bulk YIG are 1.2324 nm and 1.2377 nm respectively (with a possible uncertainty of +/- 0.001nm determined from multiple reported measurements)[32]. The lattice parameters of the GGG and SGGG substrates are 1.2376 nm and 1.2480 nm respectively. It has been observed that the lattice parameters of c-site substituted garnets vary linearly between the two end-members[18]. Therefore, YTmIG films grown on either substrate are expected to exhibit tensile in plane strain which decreases with increasing yttrium content. Figure 5.1c shows that as the composition changes from TmIG to YIG, the shear strain for films on GGG decreases from a tensile strain of 0.00153 to a compressive strain of 0.000715, following the predicted trend. Bulk YIG has an excellent lattice match with GGG, but the YIG film in our study is under in-plane compression. This is consistent with reports of larger-than-bulk lattice parameters in YIG, which are often attributed to iron vacancy formation due to non-ideal stoichiometry[173–175] but have also been seen in stoichiometric YIG and are not fully understood[176].

X-ray photoelectron spectroscopy (XPS) measurements of our pure YIG film, when compared to a stoichiometric bulk crystal (See Appendix) show that the film is slightly iron-rich with Y:Fe = 0.511.

For the $Y_{0.83}Tm_{2.17}IG$ and the $Y_{1.2}Tm_{1.8}IG$ films, a good fit to the Laue fringes of the high resolution XRD peaks was obtained using a multilayer model, i.e., relaxing the constraint that the lattice parameter is uniform through the thickness of the film (Appendix 1). The peaks were fitted with a combination of two layers of different lattice parameters. We attribute this behavior to a through-thickness out-of-plane strain gradient that leaves the film pseudomorphic. Strain gradients have been reported in YIG/GGG[77] and do not preclude garnet films from being pseudomorphic[177] – indeed, a reciprocal space map taken on the $Y_{0.83}Tm_{2.17}IG$ film confirmed that it was fully strained in-plane throughout its thickness (Figure 5.1d). Another possible source for the lattice parameter variation is cation segregation. Through-thickness composition gradients have been observed in ultrathin perovskite films grown under strain[178–180], explained as a result of the accommodation of strain energy by the segregation of differently-sized ions during growth. This mechanism may apply in YTmIG if Y^{3+} (the larger ion, Shannon radius 1.019 nm c.f. Tm^{3+}, 0.994 nm)[181] is enriched near the substrate interface to reduce the in-plane tensile strain. However, XPS depth profile analyses on these two films (Appendix 1) did not find any significant gradient in the composition, implying that the gradient in the lattice parameter used to fit the XRD data results from a strain gradient. Regardless of the origin of the lattice parameter gradient, the calculated unit cell angles follow the trend expected from the composition, and the analysis yields the average shear strain through the thickness of the film.

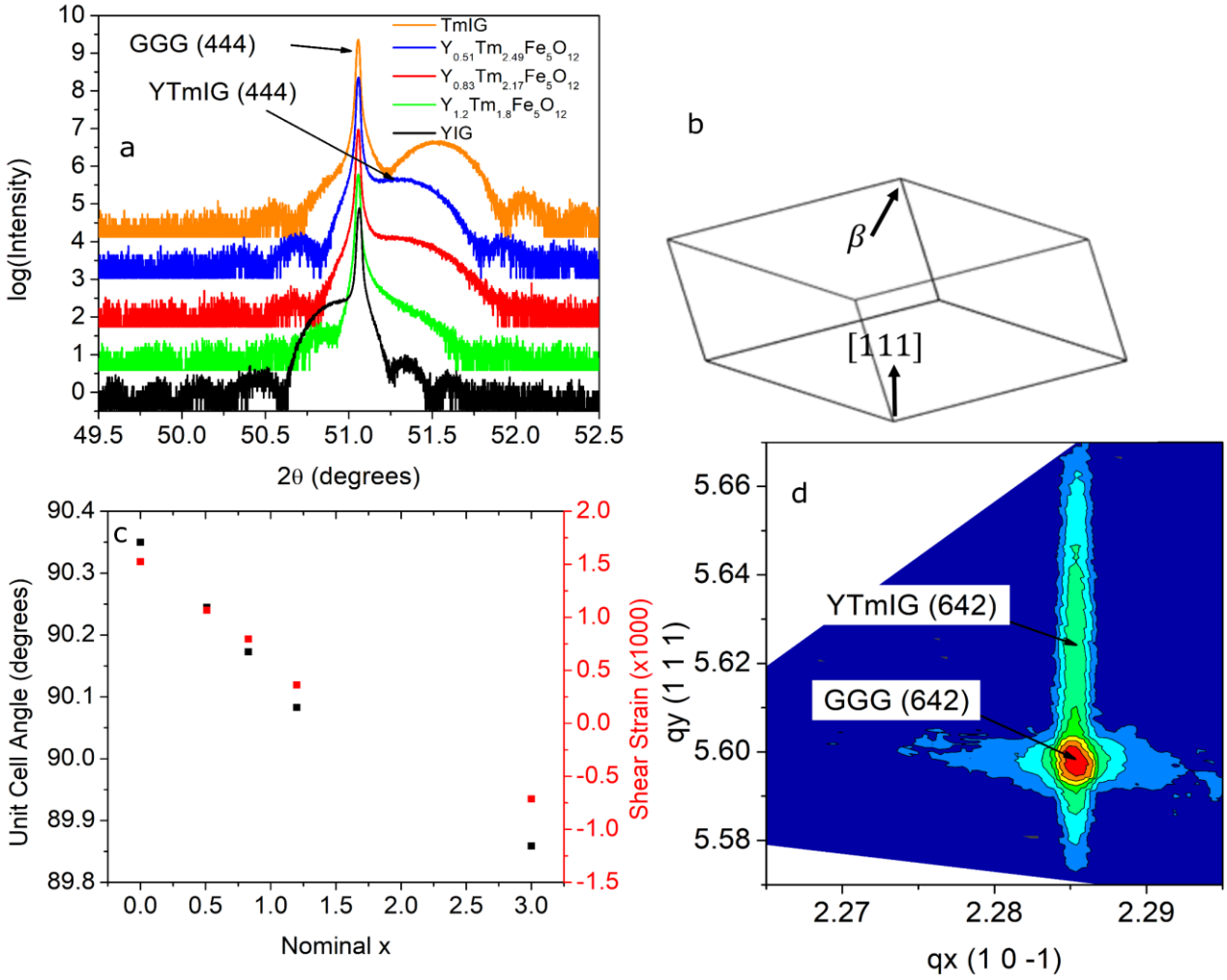

Figure 5.1: Structural Characterization of $Y_xTm_{3-x}IG$ thin films. (a) HRXRD 2θ-ω spectra about the (444) reflection of the five films studied in this chapter. (b) Schematic depicting the geometry of the unit cell used in calculated the shear strain. (c) Unit cell angle β and shear strain (in radians) of the $Y_xTm_{3-x}IG$ thin films under consideration. (d) Reciprocal space map (RSM) of the $Y_{0.83}Tm_{2.17}IG$ (642) reflection. The vertical alignment of the film and substrate peak is indicative of pseudomorphic growth.

5.2 VSM Characterization and Anisotropy Analysis

Vibrating sample magnetometer (VSM) measurements were performed, Figure 5.2a,b, to determine the effect of Y:Tm composition on the magnetic hysteresis loops of films on GGG. As the yttrium content increases, the out-of-plane loops become increasingly sheared and the in-plane saturation field decreases. Figure 5.2c shows the saturation magnetization M_s vs. composition. The saturation magnetization increases with increasing yttrium content consistent with the higher M_s of YIG compared to TmIG. The large paramagnetic background signal of the GGG substrate prevented background subtraction for the out-of-plane (hard axis) hysteresis loop of the YIG/GGG film. The saturation magnetization M_s of YIG was therefore measured from a YIG/SGGG sample that was grown simultaneously with the YIG/GGG. As shown in the Supplementary Information, the films grown on GGG and SGGG have identical saturation magnetizations measured from the in-plane hysteresis loop. The anisotropy energy of all the films was also obtained from FMR measurements (see below).

The Y:Tm ratio has a profound impact on the magnetic anisotropy. TmIG/GGG exhibits PMA, similar to previous reports[53,56,167]. Addition of Y reduces the anisotropy and $Y_{0.83}Tm_{2.17}IG$/GGG is close to isotropic, with similar in-plane and out-of-plane loops. A further increase in Y content (as in $Y_{1.2}Tm_{1.8}IG$) gives rise to an in-plane magnetic anisotropy. To quantitatively extract the magnetic anisotropy energy (MAE) from VSM data, we measure the area enclosed by the H>0 portions of the easy and hard axis loops, after eliminating any hysteresis by averaging the ascending and descending branches[182]. The MAE is plotted in Figure 5.3a, varying from 4.6 kJ/m^3 for TmIG/GGG (PMA) to ~0 for $Y_{0.83}Tm_{2.17}IG$/GGG and -3.1 kJ/m^3 for $Y_{1.2}Tm_{1.8}IG$/GGG (i.e. in-plane easy axis).

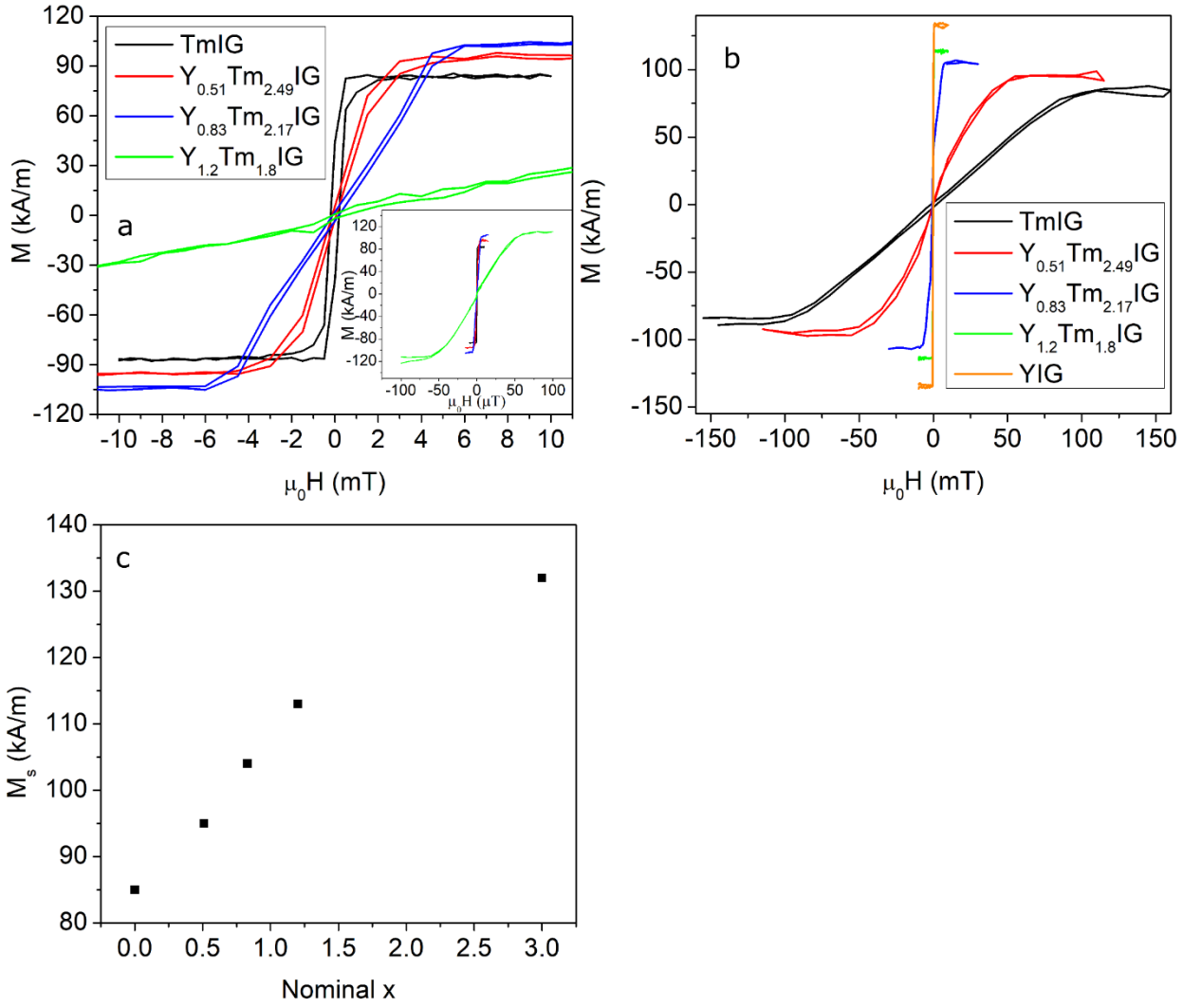

Figure 5.2: Out-of-plane (a) and in-plane (b) VSM hysteresis loops from the $Y_xTm_{3-x}IG$/GGG thin films. To account for a slight difference in VSM sensitivity in the in-plane and out-of-plane geometries, the in-plane M_s was scaled to match the out-of-plane M_s for each film. The YIG out-of-plane hysteresis loop is omitted because its large out-of-plane saturation field made background subtraction unreliable. (c) Saturation magnetization versus Y content

The MAE in the (111)-oriented epitaxial iron garnet films can be written as follows, with E_{IP} and E_{OP} the energy when the magnetization is oriented in plane (IP) or out of plane (OP) respectively:

$$MAE = E_{OP} - E_{IP} = K_u + K_{shape} = -\frac{K_1}{12} + \frac{9}{4}\lambda_{111}c_{44}(\frac{\pi}{2} - \beta) + K_G - (\frac{\mu_0}{2})M_s^2 \quad [1]$$

This expression includes the magnetocrystalline energy K_1, the magnetoelastic energy which is a function of magnetostriction λ_{111}, shear strain $\frac{1}{2}(\frac{\pi}{2} - \beta)$ and shear modulus c_{44}, and the shape anisotropy $\mu_0 M_s^2/2$. The expression is modified from prior work[43,53] by adding a uniaxial growth anisotropy K_G. K_u, which is plotted in Fig. 5.3b, represents the sum of anisotropies that compete with the shape anisotropy to yield PMA when $|K_u| > |K_{shape}|$. The sign convention gives a positive MAE for films with PMA. The magnetocrystalline contribution is small for REIGs at room temperature[32].

The substitution of Y for Tm affects the anisotropy terms in Eq. [1]. First, the M_s of YIG is higher than that of TmIG so substituting Y will increase the shape anisotropy and lower PMA. Second, increasing Y raises the lattice parameter which lowers the tensile shear strain, and Y also lowers the magnetostriction. Bulk YIG has a lower λ_{111} than TmIG, -2.73×10^{-6} for YIG and -5.2×10^{-6} for TmIG[32]. The lower strain and magnetostriction resulting from Y substitution therefore reduces the magnetoelastic contribution to PMA.

In Eq. 1, the shape anisotropy term is obtained from M_s, the unit cell angle β is determined from the XRD analysis, and the shear modulus c_{44} is taken as that of YIG[32], 766 GPa. Reported c_{44} values for YIG, EuIG, and GdIG are within 3% of each other, indicating that c_{44} for iron garnets is weakly dependent on the rare-earth species[32]. The bulk K_1 = -610 J/m^3 for YIG and -580 J/m^3 for TmIG[32] provides a negligible contribution to the total anisotropy of the samples. Taking these bulk values as a reference, $K_1/12$ is approximately 50 J/m^3, two orders of magnitude lower than the observed shape and uniaxial anisotropies. Without considering K_G, we derive effective values

of $\lambda_{111,eff}$ as shown in Figure 5.3c. Two striking features of these data are immediately evident. First, the value of $\lambda_{111,eff}$ for both endmembers TmIG and YIG (based on the anisotropy energy determined by FMR) are larger than the bulk values. Second, there is an increase (rather than a decrease) of $\lambda_{111,eff}$ with Y content for the films containing both Y and Tm. For bulk garnets[32], the magnetostriction follows the rule of mixtures, i.e., a linear interpolation between the two endmembers, but in our films the intermediate compositions have an effective magnetostriction far greater than those of YIG and TmIG.

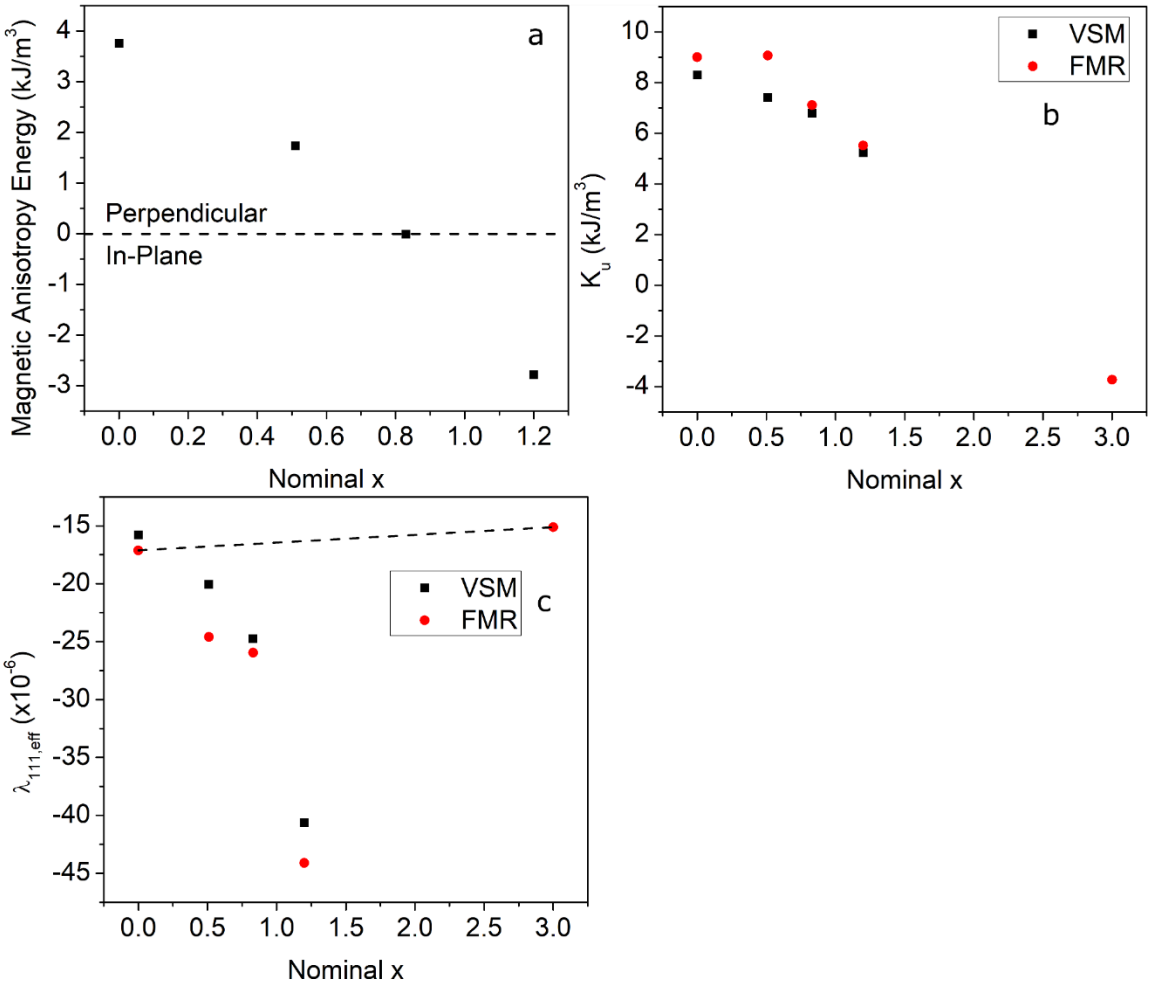

Figure 5.3: Extracted anisotropy and magnetostriction data. (a) Total magnetic anisotropy (including shape anisotropy) calculated by integrating the area between the out-of-plane and

in-plane hysteresis loops in Figure 2. (b) Uniaxial anisotropy (not including shape anisotropy), calculated from both VSM and FMR data (see below). The x=3 point (pure YIG) was accessible via FMR but not VSM. (c) Calculated effective magnetostriction λ_{111} for the $Y_xTm_{3-x}IG$ films (derived from Equation 1 and the FMR K_u values). The dotted line is the interpolated anisotropy from the rule of mixtures.

These observations suggest that there is an additional source of anisotropy beyond the magnetocrystalline, shape, and magnetoelastic anisotropy terms, identified by the term K_G in Eq. [1]. One possible origin of the additional anisotropy is growth-induced ordering of the dodecahedral-site cations, similar to what has been observed in thicker films of mixed-composition garnets grown by liquid phase epitaxy (LPE)[18]. The mechanism for this form of anisotropy is the preferential incorporation of rare-earth cations into inequivalent dodecahedral sites in the crystal lattice on the basis of their size. This broken symmetry yields an additional uniaxial anisotropy term in (111)-oriented films.[18] Growth-induced anisotropy is proportional to $x(3-x)^2$ where x is the yttrium content ($0 \leq x \leq 3$), i.e., the growth-induced anisotropy would be maximized for a Y:Tm = 1:1 composition[18]. On the basis that $K_G = 0$ for the endmembers TmIG and YIG, and that λ_{111} is given by a linear interpolation between the magnetostriction of the endmembers, we determine K_G for the intermediate compositions as shown in Table 2. Note that, for consistency, FMR data was used to derive K_u and the interpolated λ_{111} because the anisotropy field of YIG was not measurable by VSM.

Table 5.2: Interpolated Magnetostriction and Calculated K_G for YTmIG/GGG Films

Sample	Interpolated λ_{111}, $x10^{-6}$ (FMR-derived)	Growth-Induced Anisotropy Energy K_G (J/m^3)
TmIG	-17.12±0.04	0
$Y_{0.51}Tm_{2.49}IG$	-16.78±0.03	2890±20
$Y_{0.83}Tm_{2.17}IG$	-16.56±0.04	2580±10
$Y_{1.2}Tm_{1.8}IG$	-16.32±0.08	3470±10
YIG	-15.11±0.04	0

Growth-induced anisotropy has been studied mainly in LPE-grown garnets[18,42,183,184], but recently its existence was inferred in PLD-grown Bi:YIG thin films[41] through an analysis similar to this work. In LPE growth, YTmIG films would not be expected to exhibit growth-induced anisotropy because the ionic size difference of 2.5 pm between Y^{3+} and Tm^{3+} ions is smaller than the size difference of 5 pm required for the onset of growth-induced anisotropy[18]. This could imply that growth-induced anisotropy appears more readily under the non-equilibrium conditions that prevail during in PLD growth.

However, growth-induced anisotropy from dodecahedral ordering alone cannot explain the large excess magnetostriction in the TmIG and YIG films compared to bulk. EuIG films were also reported to have a magnetostriction exceeding the bulk values[43]. A significant difference in c_{44} values for PLD-grown garnets appears unlikely, because a study on LPE-grown Bi:YIG showed c_{44} very close to bulk[185]. One possibility is the existence of growth-induced anisotropy from

cation ordering on the iron sublattice. Previous work on iron-deficient YIG has shown that vacancies preferentially form on the octahedral sublattice during PLD growth, giving rise to an additional growth induced anisotropy[172]. Our YIG is Fe-rich (see Appendix 3). Therefore, there may be two forms of growth-induced anisotropy operating in the YTmIG films: one induced by ordering of Y and Tm on the dodecahedral sites (observed unequivocally in the non-monotonic variation of $\lambda_{111,eff}$) and one induced by ordering of antisites, vacancies or other point defects resulting from non-ideal stoichiometry (observed in the higher-than-bulk magnetostrictions of the end-member films). However, additional work simultaneously varying the dodecahedral and the octahedral/tetrahedral site occupancies would be necessary to confirm this hypothesis.

5.3 FMR Characterization

The dynamic magnetic properties of the YTmIG films were studied with broadband perpendicular FMR spectroscopy based on the vector network analyzer (VNA) technique[186–189]. A static out-of-plane magnetic field up to $\mu_0 H = 2.2$ T was swept while a fixed microwave field with a frequency as high as 40 GHz was applied via a coplanar waveguide with a 100 μm wide center conductor. For certain positions on the films, multiple closely-spaced resonances were observed (see Appendix 4), which we ascribe to regions with slightly different anisotropy values. As we will show later, such regions were observed via MOKE microscopy. For all samples except for the pure YIG film, regions with a single resonance could be found; fits to the single-peak data were used to calculate the materials parameters as described below. Broad resonances in the spectra originate from the GGG substrates (Appendix 5).

The complex susceptibilities of the films were extracted from the complex transmission parameters S_{21} via the relationships derived in reference Ding *et al*[187] (Figure 5.4a). Then, using the procedure

described in Nembach *et al*[186], the effective magnetization M_{eff} and the Landé g-factor were extracted using the Kittel equation for the perpendicular geometry:

$$H_{res} = \frac{2\pi f}{|\gamma|\mu_0} + M_{eff} \quad [2]$$

In this expression, H_{res} is the resonance field, f is the excitation frequency, and γ is the gyromagnetic ratio $(g\mu_B)/\hbar$ where μ_B is the Bohr magneton and ħ is the reduced Planck constant. In order to confirm the agreement between the VSM measurements and the FMR results, K_u is extracted from M_{eff} from the equation[21,56]

$$M_{eff} = M_s - \frac{2K_u}{\mu_0 M_s} \quad [3]$$

The results of these calculations are presented in Figure 5.3b, where we can see good agreement between the VSM-derived and FMR-derived anisotropy values. This also provides an independent confirmation of the existence of the excess anisotropy discussed in the previous section.

The damping α was extracted using the expression:

$$\Delta H = \frac{4\pi\alpha f}{|\gamma|\mu_0} + \Delta H_0 \quad [4]$$

where ΔH is the experimentally observed linewidth determined from fitting the S_{21} data with the complex susceptibility and ΔH_0 is the inhomogeneous broadening linewidth[190]. Exemplary fits for ΔH and H_{res} are displayed in Figure 5.4b.

The extracted g-factor values (Figure 5.4c) show a monotonic increase from 1.5744±0.0007 for TmIG to 1.7701±0.0004 for x = 1.2. These values are significantly lower than the value of 2 expected for a free electron. In order to explain the values and trends in g-factor with x, we can

apply a simple two-sublattice model based on the Landau-Lifshitz (LL) equation which was originally derived by Kittel[191] to describe g-factors in rare-earth-substituted YIG. The central assumption in this model are that the damping on the rare-earth sublattice is much larger than the damping on the iron sublattice; upon making this assumption and solving the secular equation for the coupled LL equations for the rare earth and the net iron moments we obtain the simple relationship

$$g_{eff} = \frac{g_A(M_A+M_B)}{M_A} = g_A\left(1 - \frac{|M_B|}{|M_A|}\right) \text{ [5]}$$

where M_A and M_B are the saturation moments of the resultant iron and the rare-earth sublattices, respectively (note that in this model M_A and M_B have opposite signs). It is unknown how the M_s is apportioned between the iron and rare earth sublattices. Following Kittel, we make the additional assumption that M_A is identically equal to the M_s of YIG and that M_A+M_B is identically equal to the M_s of a particular YTmIG sample:

$$g_{eff} = g_{YIG}\frac{M_S(YTmIG)}{M_S(YIG)} \text{ [6]}$$

Using the measured values for the M_s of YIG and YTmIG, we obtain the theoretical estimate of g_{eff} which is plotted in Figure 5.4c. Both the model and the experimental values converge for the YIG/GGG film, which possesses a bulk-like g factor of 2.0132±0.0003. However, while the model agrees with the experiment in that both show a linear dependence of g_{eff} on the Y concentration, the slope of the model curve is steeper than that of the experiment. This is likely due to the sublattice contributions to M_s in TmIG being different than in YIG – a possibility discussed in Ref. 49. To investigate this possibility, we can further manipulate the Kittel model by relaxing the assumption that M_A=M_{YIG} and instead allowing M_A to vary. To obtain a linear dependence, we assume instead that $|M_B|/M_A$ varies linearly with x and obtain:

$$g = g_A\left(1 - 3\left(\frac{|M_B|}{M_A}\right)_0\right) + g_A\left(\frac{|M_B|}{M_A}\right)_0 x \text{ [7]}$$

Here, $(|M_B|/M_A)_0$ is the magnetization ratio when x=0. A linear fit of our data to this expression yields the empirical expression:

$$g = (1.584 \pm 0.009) + (0.145 \pm 0.006)x \text{ [8]}$$

By matching slopes and using our experimentally measured value for g_A (the g-factor measured for x=3), we calculate that $(|M_B|/M_A)_0$= 0.0720±0.0006. To check for consistency, we can calculate the new predicted y-intercept of the g-factor using this value; we obtain 1.578±0.002, which is within the error bar for our fit. Therefore, we can conclude that our assumption is correct: $|M_B|/M_A$ varies linearly with x, even though M_A is not a constant equal to M_{YIG}. Interestingly, our results are at odds with a previous report that M_A stays constant in $Y_{2.4-x}Tm_xBi_{0.6}Fe_{5-y}Ga_yO_{12}$ (for constant y)[192]. Sum rule analysis via x-ray absorption spectrometry/x-ray magnetic circular dichroism (XAS/XMCD) may help shed light on this discrepancy.

The damping values extracted from the FMR data are displayed in Figure 5.4d. Due to the multiple resonances mentioned earlier, a value for g was obtained for YIG but α could not be extracted from the data. Therefore, the red data point in Figure 5.4d is from YIG grown previously by our group using a similar PLD growth process[193]. The damping values show a monotonic linear decrease from (1.32 ±0.02) × 10^{-2} for TmIG to the previously reported YIG value of (2.2±0.2) × 10^{-4}. This is expected because rare-earth ions such as Tm^{3+} are known to relax rapidly compared to Fe ions[191]. The TmIG value of α is comparable to previously reported values[194]. This is in good agreement with Kittel's microscopic model of the linewidth in RE-substituted YIG[195] and previous experimental work in Sm-substituted YIG[196]. The linear decrease of damping with Y content

suggests that low-damping YTmIG films with PMA can be grown by leveraging growth-induced and strain-induced anisotropy.

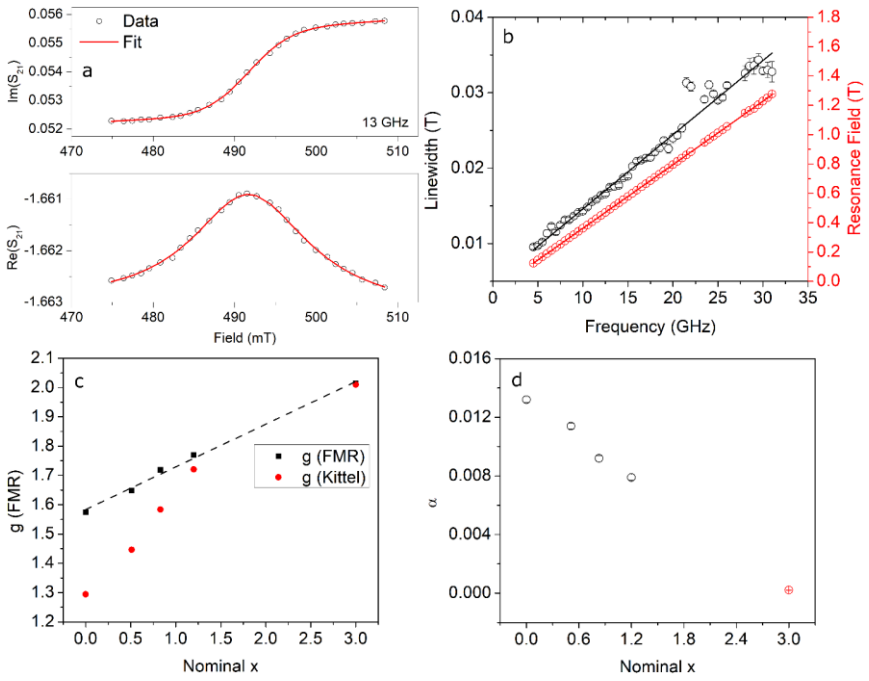

Figure 5.4: (a): Representative fits of FMR spectra from the $Y_{0.51}Tm_{2.49}IG$ thin film. (b) Representative fits of ΔH versus frequency (black) and H_0 versus frequency (red) from the $Y_{0.51}Tm_{2.49}IG$ thin film. (d) g-factor versus x. The red points are calculated by the Kittel model, and the dotted line is the linear fit to the data. (e) Damping versus composition, x. The red point is from a previously reported YIG film[193].

5.4 MOKE Analysis and Domain Characterization

As we have seen, the easy axis loops for the TmIG, $Y_{0.51}Tm_{2.49}IG$ and $Y_{0.83}Tm_{2.17}IG$ samples display increasing amounts of shear as the Y content increases. This is indicative of domain formation in PMA thin films. With decreasing uniaxial anisotropy, thin films with PMA cannot support a uniform out-of-plane magnetization at remanence and instead form stripe domains to reduce magnetostatic energy[29,45,46]. Our recent work on TmIG using scanning transmission x-ray

microscopy[55] showed labyrinthine arrays of stripe domains. According to the seminal work on stripe domains by Kooy and Enz[45], the loop shearing and the saturation field will increase as M_s increases and K_u decreases.

Polar MOKE microscopy was used to image the domain morphologies of the TmIG and the $Y_{0.51}Tm_{2.49}IG$ films. In order to maximize contrast, an LED light source with a wavelength of 457 nm was used. Before imaging, an out of-plane AC demagnetization process with an exponentially decaying oscillating magnetic field was performed to promote a low-energy multidomain state. An image taken at saturation was subtracted to reduce nonmagnetic contrast. Representative images are displayed in Figure 5.5. In order to quantify the domain spacing, two-dimensional fast Fourier transforms (2D FFT) were performed on the MOKE images and radial average intensities were extracted (Figure 5.5c). Gaussian peaks were fitted to these radial intensity distributions to determine the average stripe spacing. In order to account for the effect of nonuniformity in the PLD growth, images were taken at multiple points on the samples and the resulting stripe spacings were averaged. As expected from the Kooy-Enz model, as more yttrium is added to the film, causing M_s to increase and K_u to decrease, the equilibrium stripe spacing decreases. The average equilibrium stripe spacing is 15μm±6μm for TmIG and is 4μm±3μm for $Y_{0.51}Tm_{2.49}IG$. Here, the reported error bars are the sample standard deviations of the extracted domain sizes for these two films. The spread in domain sizes across the films indicates some inhomogeneity in magnetic properties (e.g., uniaxial anisotropy and saturation magnetization) which likely explains the multiple resonances observed in FMR. From these domain size values, we can apply the model of Kaplan and Gehring[47] in order to extract the domain wall energies of these films. This analytical model, which is a limiting case of the more general Kooy-Enz model[45] for the situation where the film thickness is much less than the domain period, can be summarized in the equation:

$$D_s = t \exp\left(\frac{\pi b}{2} + 1\right) \exp\left(\frac{\pi \sigma_w}{2K_d t}\right) \quad [9]$$

Here, D_s is the stripe domain width, t is the film thickness, b is a model-dependent constant approximately equal to -0.666, σ_w is the domain wall energy, and K_d is the dipolar energy constant $\mu_0 M_s^2/2$. From this, we can calculate the domain wall energies of TmIG and $Y_{0.51}Tm_{2.49}IG$ displayed in Table 5.2. These values are well in-line with reported bulk domain wall energies in rare-earth garnets, which are generally between 0.2×10^{-3} and 1×10^{-3} J/m^2. [32]

The TmIG and $Y_{0.51}Tm_{2.49}IG$ films are well above the thickness at which a crossover from Néel to Bloch walls have been observed in TmIG[11]. By assuming that the walls are 180˚ Bloch walls we are able to estimate the exchange stiffness in these films as $A = \frac{\sigma_w^2}{16K_u}$. These estimates are also presented in Table 5.3 (the FMR-derived values for K_u were used). The TmIG film has a slightly lower exchange stiffness than the YTmIG film. Literature values for the exchange stiffness constants of undiluted garnets (i.e. garnets with no diamagnetic substitution on the iron sublattice) are rare. However, the reported value for YIG is lower than the reported value for the undiluted rare-earth garnet $Tb_{2.5}Er_{0.5}Fe_5O_{12}$[32], implying that the addition of Y to rare-earth garnets changes the exchange stiffness.

Table 5.3: Calculated Domain Wall Energy and Exchange Stiffness for TmIG and $Y_{0.51}Tm_{2.49}IG$

Material	Domain Wall Energy (10^{-3} J/m^3)	Exchange Stiffness (10^{-12} J/m)
TmIG	0.527±0.002	2.09±0.002
$Y_{0.51}Tm_{2.49}IG$	0.535±0.002	2.42±0.002

MOKE microscope hysteresis loops were collected to determine the reversal mechanism under DC fields for TmIG (Figure 5.6a) and the $Y_{0.51}Tm_{2.49}IG$ (Figure 5.6b) after saturation at ± 50 mT. For TmIG, low-field domain nucleation occurred at defects such as surface scratches in the substrate and domain growth proceeded outwards from these defects. This process of nucleation on defects is repeatable, with reverse domains appearing at similar locations and applied fields for both the forward and reverse branches. Some regions of the film bounded by surface scratches switched within one field increment without forming domains. Also, the film has a non-zero remanence, as large regions remain un-switched at zero applied field. The surface scratches are present in the substrate prior to deposition, and the film grown at those locations is likely to have a different thickness, strain state and anisotropy from the film on smooth regions, providing a barrier for domain propagation and/or a site for nucleation.

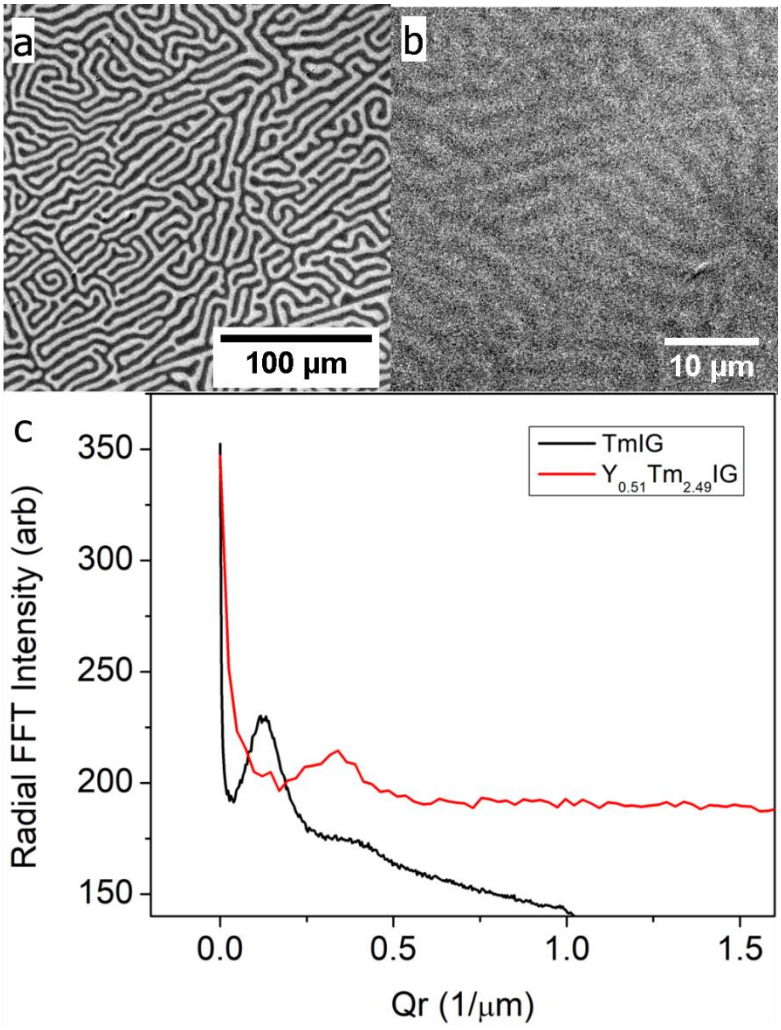

Figure 5.5: (a,b): AC-demagnetized domain structure of TmIG (a) and $Y_{0.51}Tm_{2.49}IG$ (b). Note the different scale bars in each image. (c) Radially averaged FFT spectra of the images in (a,b).

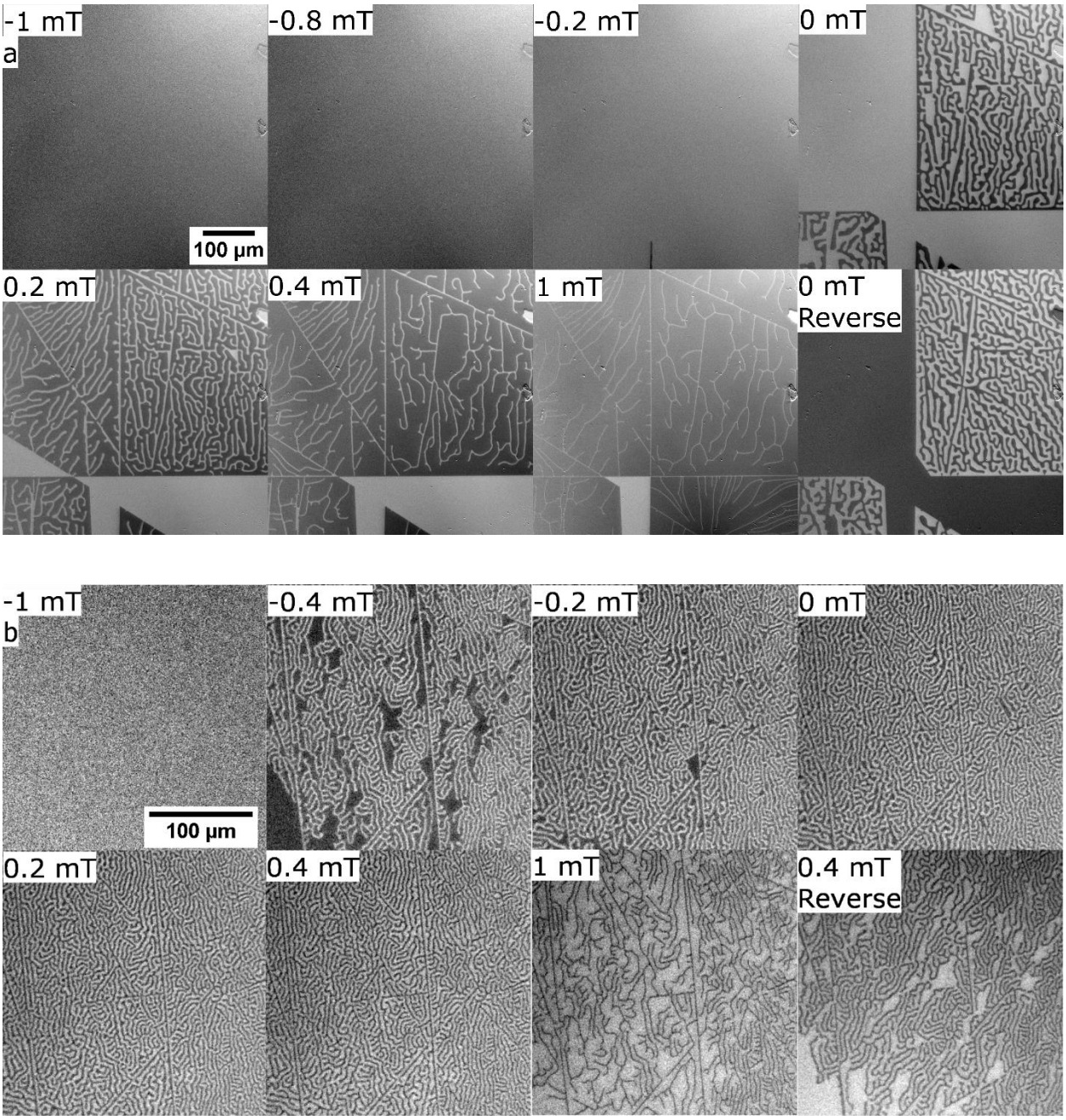

Figure 5.6: MOKE hysteresis loops of TmIG (a) and $Y_{0.51}Fe_{2.49}$IG (b) demonstrating the difference in reversal mechanism for these two films. In each panel, one picture from the "reverse" branch of the hysteresis loops is shown to whether domains occur in the same locations in the ascending and descending branches.

For $Y_{0.51}Tm_{2.49}IG$, magnetic reversal occurs in a more continuous manner, with labyrinthine stripe domains occupying the full area as the field approaches zero. Near zero applied field, domain expansion occurs in a similar manner to that described in the Kooy-Enz model[45], with the majority domains expanding and the minority domains staying the same width but becoming more sparse. The surface scratches in the film perturb the domain structure, with reverse domains tending to nucleate parallel to the scratches before expanding away from the scratches. However, domain nucleation is less clearly defect-mediated than for the TmIG film. The locations at which the domains parallel to the scratches branch into the regions adjacent to the scratches are different for the forward and reverse branches, and the reversal process is more homogeneous. The film has zero remanence at zero applied field corresponding to the presence of labyrinthine stripe domains.

The $Y_{0.83}Tm_{2.17}IG$ sample has a magnetic anisotropy energy about two orders of magnitude lower than that of the other samples, and was expected to have a continuously varying magnetization texture and/or weak stripe domains rather than the strong stripe domains seen in the $Y_{0.51}Tm_{2.49}IG$ sample[29,197]. However, it exhibited no contrast in the MOKE microscope which may indicate a predominantly in plane or uniform magnetization.

5.5 Conclusion

In this study, a systematic exploration of PLD-grown $Y_xTm_{3-x}IG$ films was carried out across the range of substitution x = 0 to 3. All the films are epitaxially matched to GGG and SGGG substrates with good crystalline quality. Films on GGG with x = 0.83 and 1.2 exhibit a through-thickness lattice parameter gradient which is attributed to a variation in strain rather than composition, and the films remain pseudomorphic to the substrate. Y-substitution has dramatic effects on the

anisotropy of YTmIG thin films on GGG, with as little as x = 0.8 causing a reorientation from PMA to an in-plane easy axis. Films containing both Y and Tm exhibit a growth-induced anisotropy which varies non-monotonically with Y content. The observation is among the first reports of a growth-induced anisotropy in PLD-grown garnet films and it occurs with a cation pair, Y:Tm, which is not expected to show this form of anisotropy based on the small difference in their ionic radii. The domain morphologies and DC switching behavior of the TmIG and the $Y_{0.51}Tm_{2.49}IG$ film differed. TmIG has a larger equilibrium domain size than $Y_{0.51}Fe_{2.49}IG$, and it reverses by the movement of domain walls across large (10s μm) regions of the film. In contrast, $Y_{0.51}Fe_{2.49}IG$ exhibits zero remanence (also visible in its sheared hysteresis loop) and reverses through stripe domain growth similar to the classical Kooy-Enz model. FMR measurements showed that the g-factor varied with yttrium content, and the variation was compared with a simple model for RE-substituted YIG films. Damping was also found to vary linearly with Y content, in agreement with previously reported data on LPE-grown films. Through the range of growth-induced and magnetoelastic anisotropy, domain structure, damping, and g-factor on a single substrate, Y-substitution provides an important control parameter for designing PLD-grown garnet thin films for spintronic device applications.

5.6 Appendices

1. HRXRD fitting results and XPS for $Y_{0.83}Tm_{2.17}$ and $Y_{1.2}Tm_{1.8}$ films

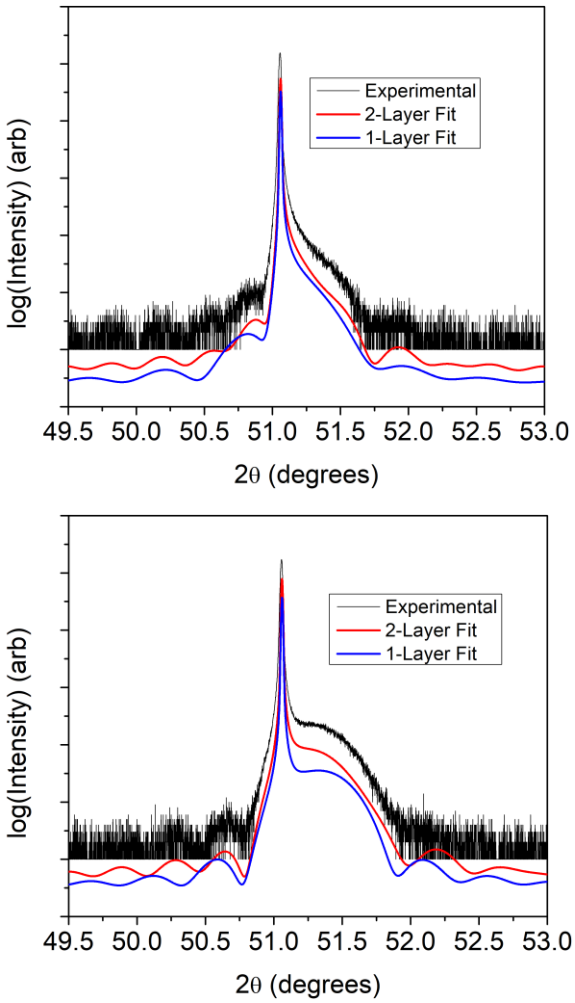

Figure 5.A1: HRXRD fitting results of $Y_{1.2}Tm_{1.8}Fe_5O_{12}$ (a) showing the improved fit when a lattice parameter gradient is introduced through the film thickness. The experimental and fit curves are offset for readability. The one-layer fit was done with a uniform composition model and was unable to accurately reproduce the thickness of the film as seen by the poor fit to the Laue fringes. The two-layer fit was done with the multilayer model described in the main text and was able to reproduce both the film peak shape and its associated Laue fringes. Similar results were found for the $Y_{0.83}Tm_{2.17}Fe_5O_{12}$ (b) film – a homogenous layer model

was unable to reproduce the positions of the strong Laue fringes on the left side of the peak and also underestimates d_{444}. However, the improvement from introducing a multilayer fit was not as dramatic in the $Y_{0.83}Tm_{2.17}$ film as it was in the $Y_{1.2}Tm_{2.3}$ film.

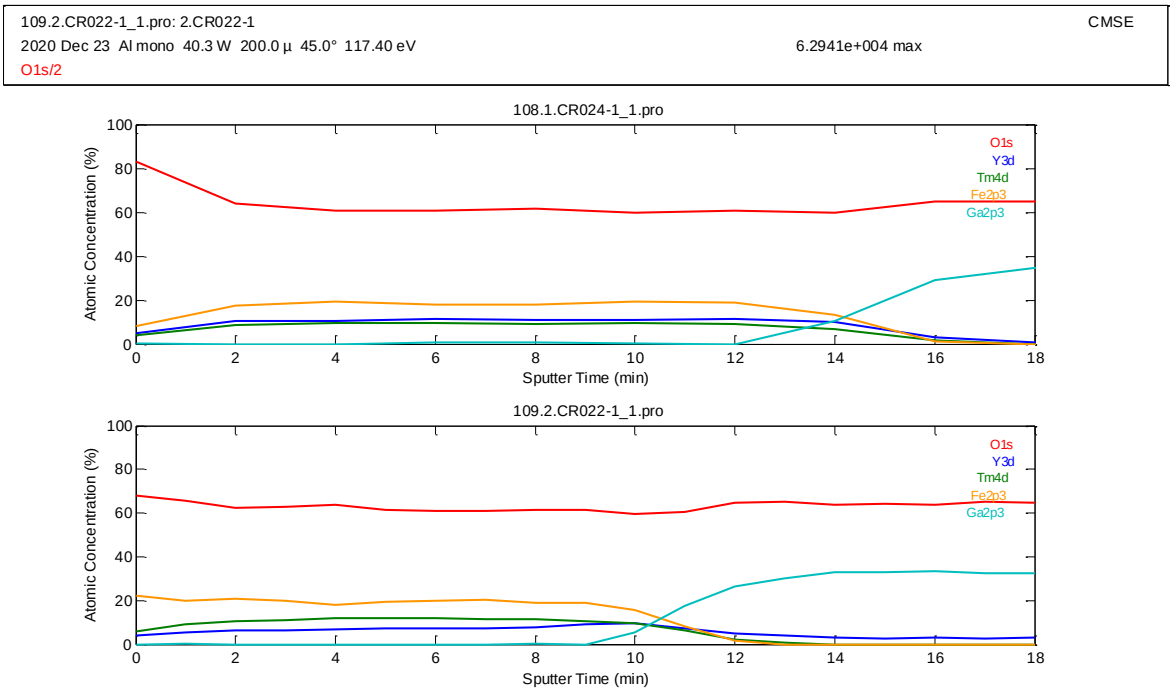

Figure 5.A2: XPS depth profile results from $Y_{1.2}Tm_{1.8}Fe_5O_{12}$ (top) and $Y_{0.83}Tm_{2.17}Fe_5O_{12}$ (bottom). To carry out this measurement, XPS survey scans were taken between ion milling steps (2kV accelerating voltage, 1 microamp ion current). 2-minute ion milling intervals were used for the $Y_{1.2}Tm_{1.8}$ film. 1-minute intervals were used for the $Y_{0.83}Tm_{2.17}$ film due to it being slightly thinner. As described in the main text, no significant through-thickness compositional gradient exists in these films. The apparent gradient in the first 2 nm of each film can be attributed to the removal of carbon contamination from the surface by the ion milling process.

2. Characterization of YIG/GGG and YIG/SGGG films

Because of the large paramagnetic background signal of GGG substrates, special care must be taken when analyzing VSM data for films with anisotropy fields higher than approximately 150 mT. For this reason, a YIG film on SGGG (substituted GGG, which has a larger lattice parameter than GGG) was grown simultaneously with the GGG film mentioned in the main text. Background subtraction was not possible for the YIG/GGG out-of-plane hysteresis loop so instead the YIG/SGGG hysteresis loop was used for the calculation of the YIG saturation magnetization. Due to the existence of a large tensile strain from the SGGG substrate (Figure S2-1) and a negative magnetostriction, the anisotropy field of YIG/SGGG was low enough for VSM background subtraction. The saturation magnetizations of YIG/GGG and YIG/SGGG were found to be identical according the in-plane hysteresis loops – implying that there is no enhancement of M_s due to strain - so this technique was deemed to be valid (Figure S2-2). Finally, the out-of-plane hysteresis loop of YIG/SGGG (see figure S2-3) was used to extract the M_s of the YIG quoted in the main text.

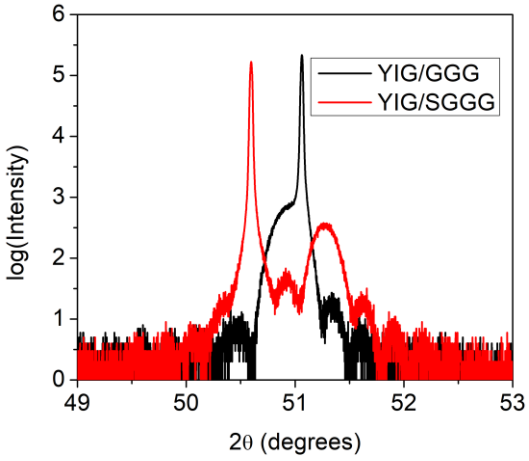

Figure 5.A3: HRXRD 2θ-ω scans of YIG/GGG and YIG/SGGG demonstrating the good crystalline quality of the films and the tensile strain exhibited by YIG/SGGG.

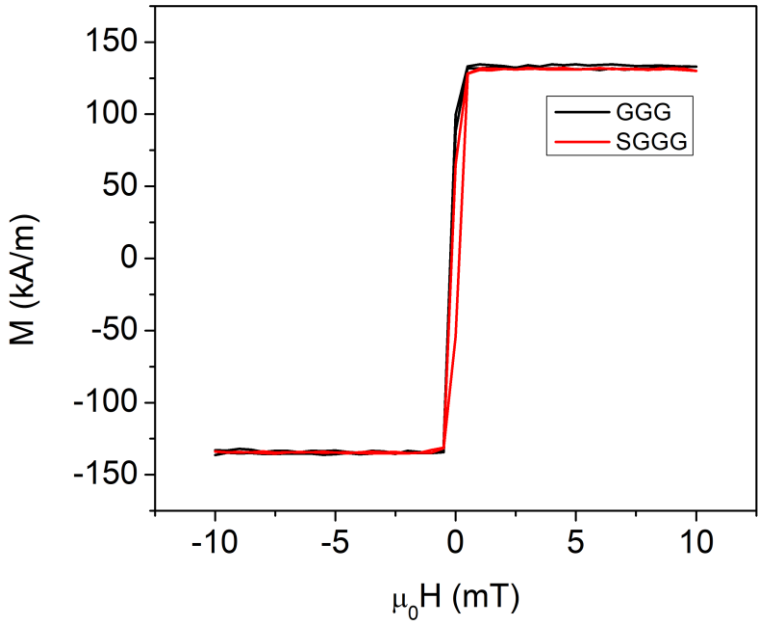

Figure 5.A4: In-plane VSM scans of YIG/GGG and YIG/SGGG demonstrating that their saturation magnetizations are identical.

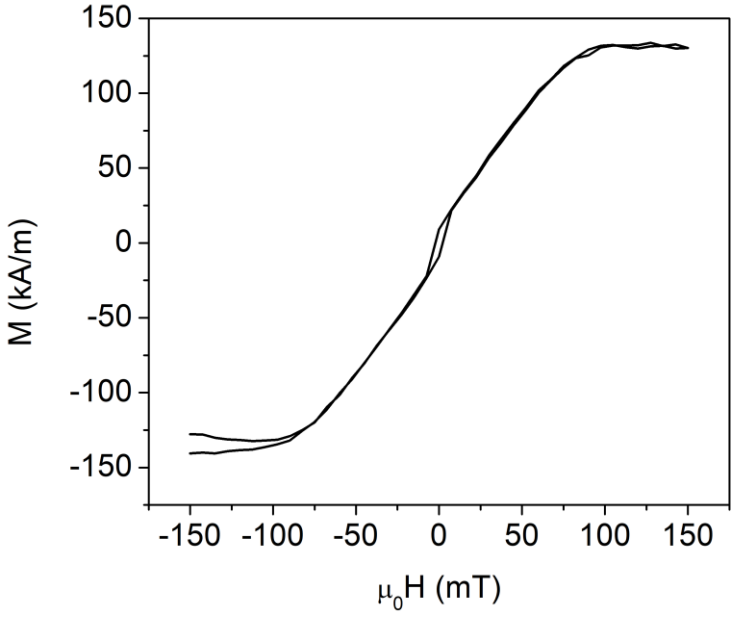

Figure 5.A5: Out-of-plane VSM hysteresis loop of YIG/SGGG which was used for the calculation of M_s in the main text. This out-of-plane scan gives a value of 132 kA/m (the value used in the main text)

3. Analysis of Stoichiometry of YIG film

In the main text, we observed that the YIG film had a larger-than-bulk magnetostriction. In order to determine whether non-ideal stoichiometry was responsible, we analyzed the composition of the YIG film and a stoichiometric bulk YIG reference sample via XPS. A short Ar presputtering process was used to remove excess carbon contamination from the surface.

The results are displayed in Table S3-1. Note that, even though the bulk sample was known to be stoichiometric, the Y:Fe atom ratio obtained from XPS is close to 1:1. This is likely due to errors in the relative sensitivity factors. We can quantify the compositions by scaling the Y:Fe ratios to the known ratio of 0.60 for the bulk reference sample. Thus, we conclude that our YIG film is slightly iron-rich.

Sample	XPS-measured Y:Fe ratio	Corrected Y:Fe ratio
YIG Film	0.976	0.511
YIG bulk reference	1.145	0.6

Table 5.A1: As-measured and corrected Y:Fe ratios for the YIG film and YIG bulk reference standard

4. Multiple Resonances in FMR

All of the films under consideration exhibited multiple closely-spaced resonances in FMR when placed in certain positions on the waveguide for measurement. We attribute this to the magnetic nonuniformity observed by MOKE microscopy. For all films except for YIG, it was possible to find positions exhibiting only single resonances; the data from these positions was used to calculate the g-factor, anisotropy, and damping data in the main text. In the case of YIG, we approximated

the g-factor and M_{eff} by fitting the envelope of the resonances. Such a fit can be seen below in Figure 5.A6.

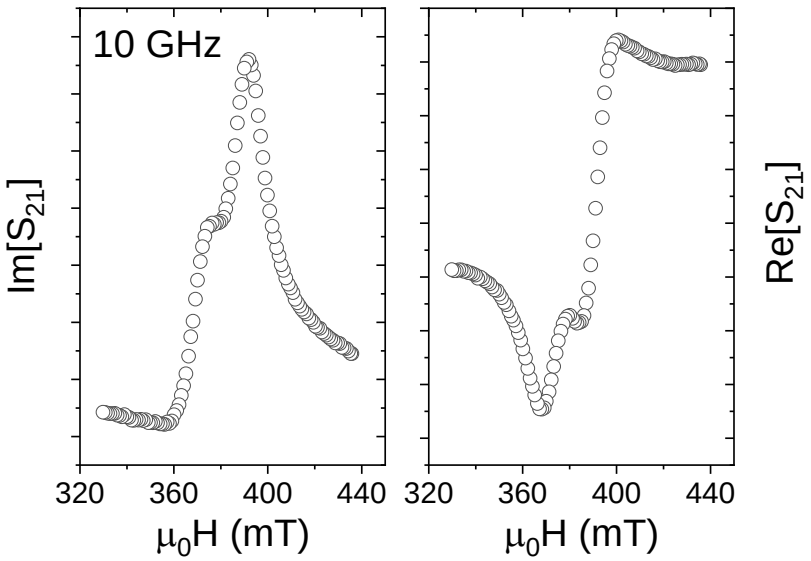

Figure 5.A6: Example of multiple resonances in one position on the $Y_{0.51}Tm_{2.49}Fe_5O_{12}$ film.

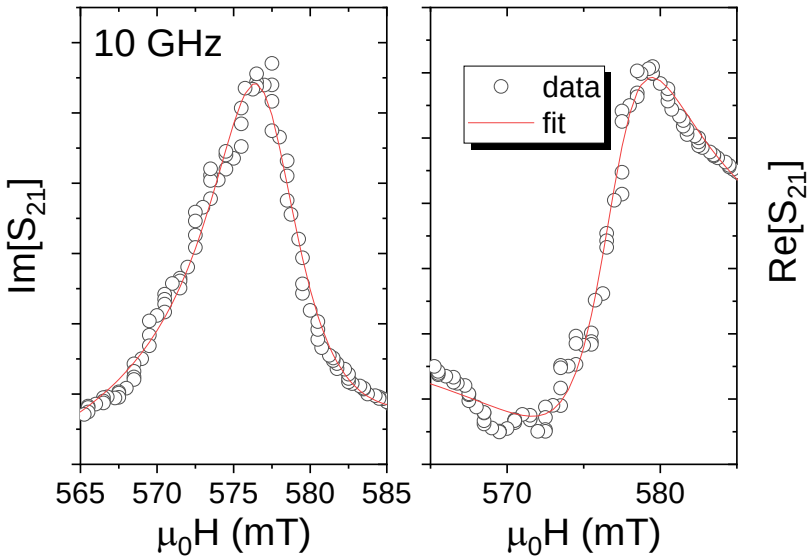

Figure 5.A7: FMR resonance from the YIG film. The structure in the resonance is repeatable and is this not noise – it is the superposition of many small-amplitude resonances. Even so, the envelope of this data could be fit to extract the g-factor and M_{eff}.

5. Broad resonances due to GGG

The GGG substrates exhibited broad resonances that contribute to a large background in the FMR signal. At high frequencies, these resonances could be fit using the same FMR formalism used for the YTmIG resonances. We tentatively attribute this to the electron paramagnetic resonance of the Gd^{3+} ions, which has been previously reported in the literature[198]. However, as shown in Figure 5-2, the losses found in the GGG are not always described by a simple resonance peak. Such large losses from the GGG substrate can present challenges in fitting the much lower amplitude signal from the YTmYIG over some frequency bands.

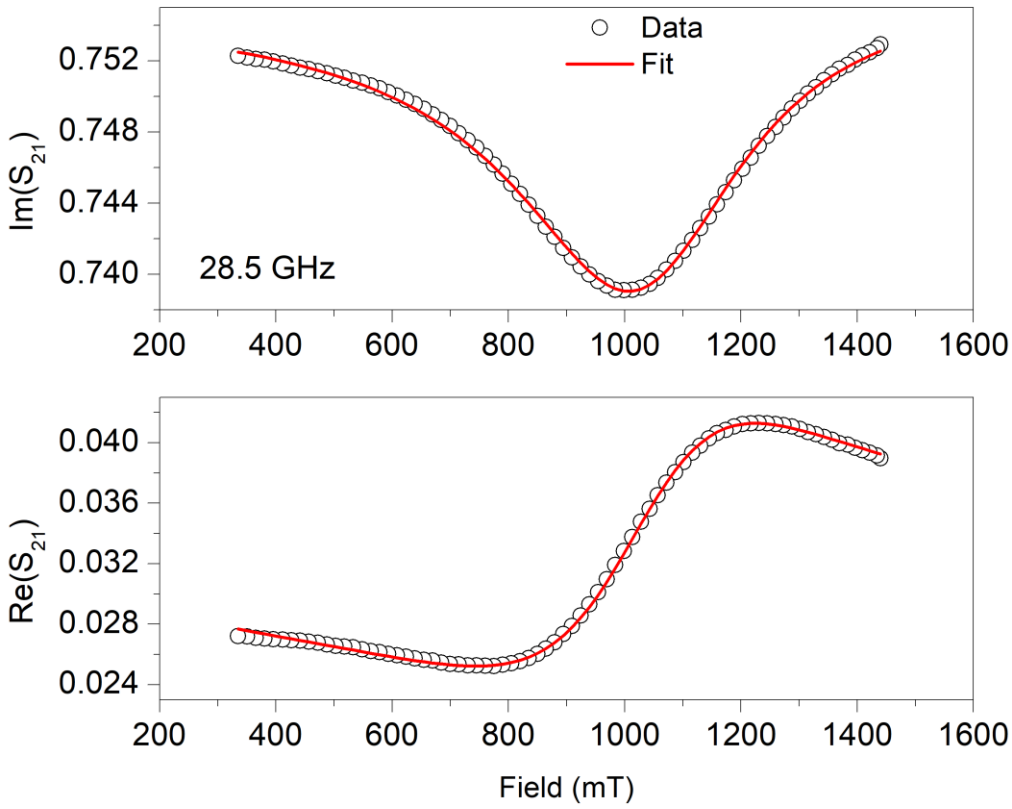

Figure 5.A8: Exemplary FMR data taken on the backside of the $Y_{0.51}Tm_{2.49}Fe_5O_{12}$ sample to isolate the background signal

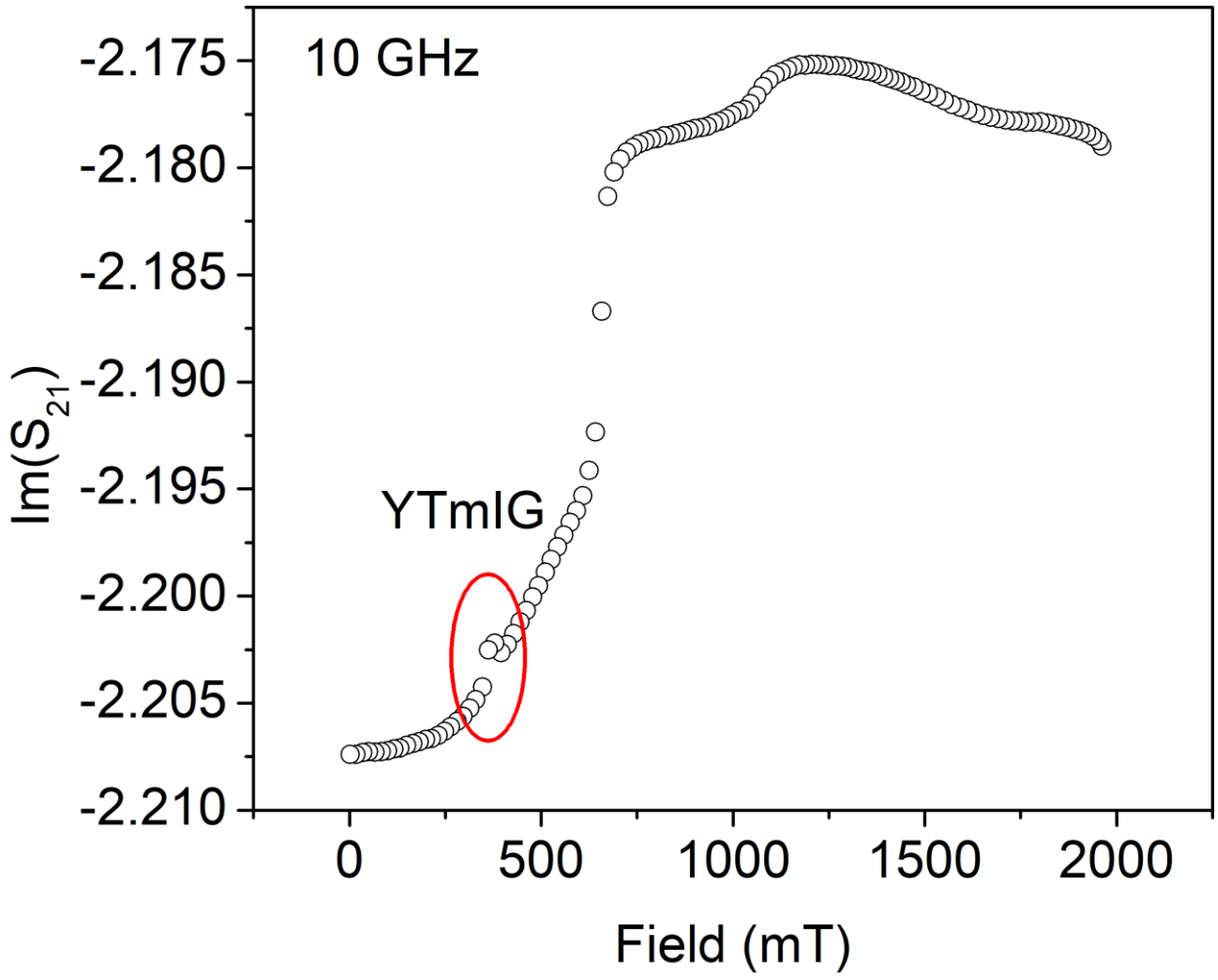

Figure 5.A9: Relative signal strengths of film and substrate signals

Chapter 6

Spintronic Applications of Rare-Earth Iron Garnet Thin Films

In this chapter, we will briefly review three recent coauthored papers to which the author contributed REIG thin films. These selected studies showcase the potential of REIG materials in spintronic applications. The first of these studies (Avci et al. 2017[14]) showed that Pt/TmIG heterostructure devices could be switched very quickly by spin orbit torques, which suggests the existence of fast domain-wall motion. The second and third studies (Avci et al. 2019[13] and Caretta et al. 2020[11]) both deal with DMI in Pt/REIG heterostructures. Only the most relevant results from these studies will be reviewed here; for more information regarding the experimental methods the reader is invited to read the original journal articles. Following this, we will present DMI measurements on Y-substituted TmIG thin films and preliminary data from a study which is aimed at explaining recent AHE measurements on thin Pt/TmIG heterostructures at elevated temperatures.

6.1 Fast Switching and Signature of Efficient Domain Wall Motion Driven by Spin-Orbit Torques in a Perpendicular Anisotropy Magnetic Insulator/Pt Bilayer

As was mentioned in Chapter 1, Pt/TmIG heterostructures were originally switched via spin orbit torques in 2016[10]. However, the TmIG in this study was produced with an un-optimized growth recipe. Further gains in material quality were obtained by optimization of the PLD fluence (see Chapter 2), and the RMS roughness of the TmIG films were reduced from 1.5 nm rms to <1nm rms (in this study, we obtained an rms roughness of 0.65nm over a $1\mu m^2$ area). This in turn led to a greater than sixfold increase in the real spin-mixing conductance with Pt, G_r, from 1.0×10^{14} Ω^{-}

$^{1}m^{-2}$ to 6.5×10^{14} $\Omega^{-1}m^{-2}$ – comparable with or larger than contemporary studies on NM/FMI heterostructures[81,109,131].

The improvements to the TmIG thin film growth recipe paid dividends in the form of improved SOT switching characteristics, which were investigated in a Pt(4nm)/TmIG(9.6nm)/GGG(111) heterostructure[14]. These results are summarized in Table 6.1. An interesting result from this study was an observed dependence of the threshold switching current density on the device pulse history. If a device started in a field-saturated state, it required more current to switch than if it started in a current-saturated state. The reason for this was that the reset voltage (to achieve current saturation) did not fully expel the reverse domain (see Figure 6.1). Also, switching times were faster for the current-saturated state (which switched by domain expansion with no nucleation step necessary): by considering the device geometry and the current pulse time, domain wall velocities of ~1000m/s were achieved, exceeding the fastest reported speeds in contemporary all-metallic heterostructures[199]. These results were further explored in the next two studies we will review.

TmIG Recipe	Roughness (nm rms)	G_r ($\Omega^{-1}m^{-2}$)	Critical J_{switch} (A/m^2)
Avci *et al* 2016[10]	1.5	1.0×10^{14}	1.8×10^{11}
Avci *et al* 2017[14]	0.65	6.5×10^{14}	0.6×10^{11}

Table 6.1: Comparison of unoptimized and optimized TmIG spintronic properties

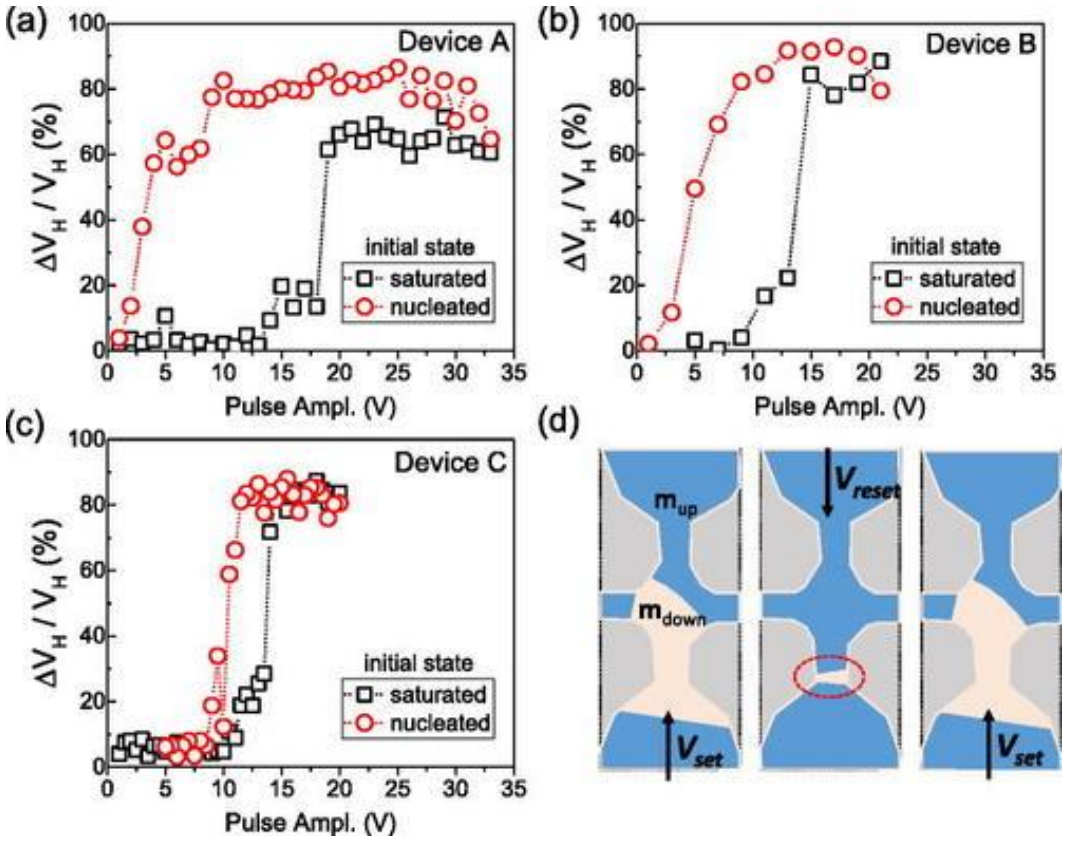

Figure 6.1: (a-c): SOT switching results for field- and current-saturated devices. Experimental conditions: pulse width = 20 ns, H_x = 177 Oe, pulse voltage = +/- 27 V. Panel (d) shows a schematic view of the domain expansion in a current-saturated device. Reprinted from Avci *et al* (2017)[14] with permission.

6.2 Interface-Driven Chiral Magnetism and Current-Driven Domain Walls in Insulating Magnetic Garnets

After the discovery of fast domain wall motion in our improved TmIG thin films, a new study was carried out in which MOKE was used to study domain wall chirality and motion in REIG thin films[13], specifically in TmIG and TbIG. For this study, 5.1nm thick and 7.1nm thick TmIG and TbIG films were used, respectively. These films were patterned into domain wall track structures

with a gold nucleation line so that domain walls could be reproducibly nucleated with current-pulse-induced Oersted fields (see journal article for details about the experiment)

By investigating the critical depinning current as a function of in-plane field, the existence of DMI-stabilized chiral Néel walls (see Chapter 1) was discovered in REIG materials for the first time. Figure 6.2 shows the details of this experiment in a Pt(4nm)/TmIG(5.1nm) heterostructure. The sign change and divergence in the critical depinning current at $H_x \sim \pm 50$ Oe corresponds to the field range over which the Néel domain wall becomes a Bloch wall and then a Néel wall of the opposite chirality (the so-called DMI effective field). The handedness of the DMI-induced chirality was found to be opposite to that of Pt/ferromagnetic metal interfaces. The low M_s of garnet films compared to ferromagnetic metals allowed the DMI to stabilize Néel walls despite its small magnitude of ~0.002mJ/m^{-2} for Pt/TmIG, about two orders of magnitude lower than Pt/ferromagnetic metal heterostructures. In addition, TbIG showed similar DMI magnitudes with and without Cu spacer layers (between the Pt and the garnet), implying that the DMI arose from the bottom interface.

Finally, the high domain wall velocities which were theorized in Avci *et al* 2017[14] were definitively observed in this study (see figure 6.3). Velocities exceeding 800 m/s at current densities of 1.2×10^{12} A/m^2 were observed – higher than metallic systems at comparable current densities. This was attributed to the ferrimagnetic nature of REIG materials – rescaling γ and α using Wangsness' two-sublattice model[200] predicts that domain wall velocity saturation should occur at much higher domain wall velocities in ferrimagnets compared to ferromagnets (see figure 6.3)[199].

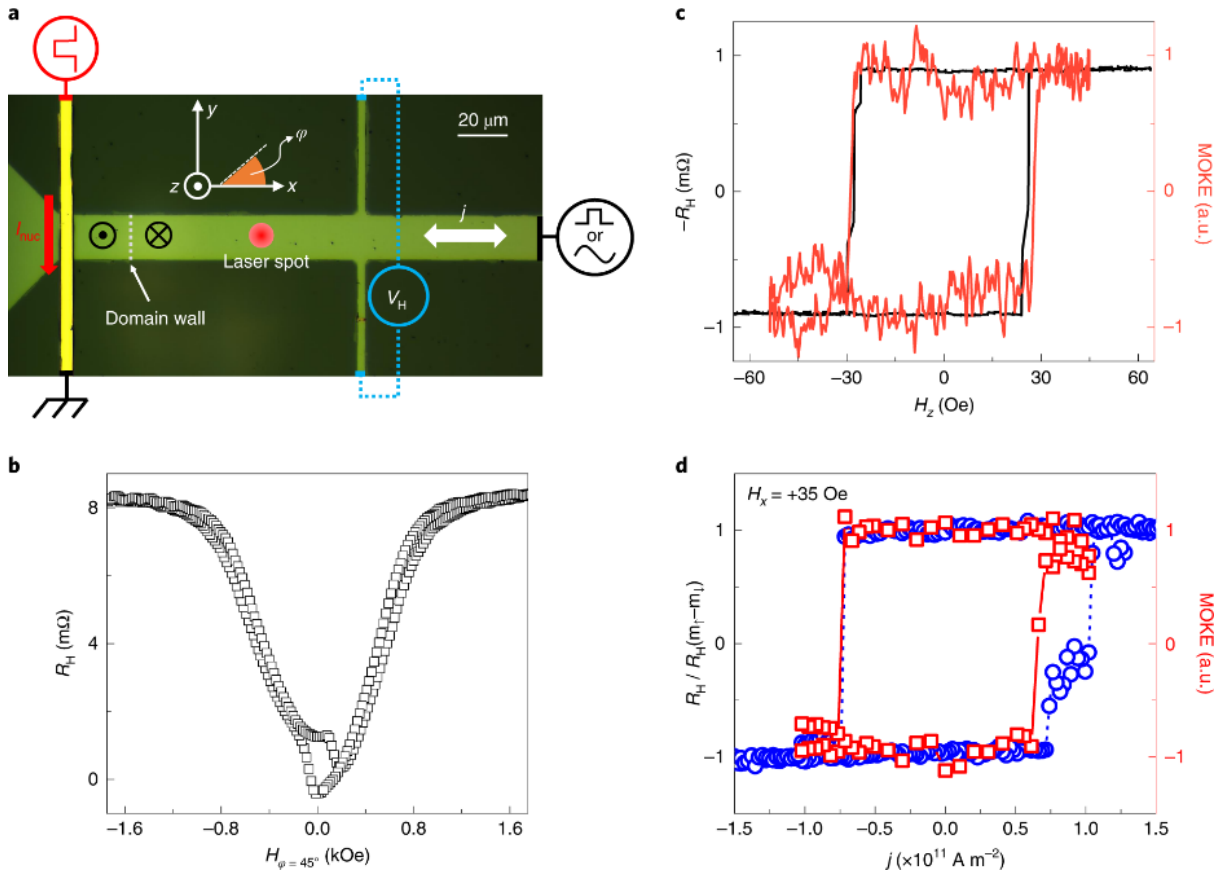

Figure 6.2: (a): Optical micrograph of the domain wall track/nucleation line device used in this study. (b-d): SMR, MOKE, and SOT switching hysteresis loops taken on the Pt/TmIG/GGG device shown in (a). Reprinted from Avci *et al* (2019)[13] with permission.

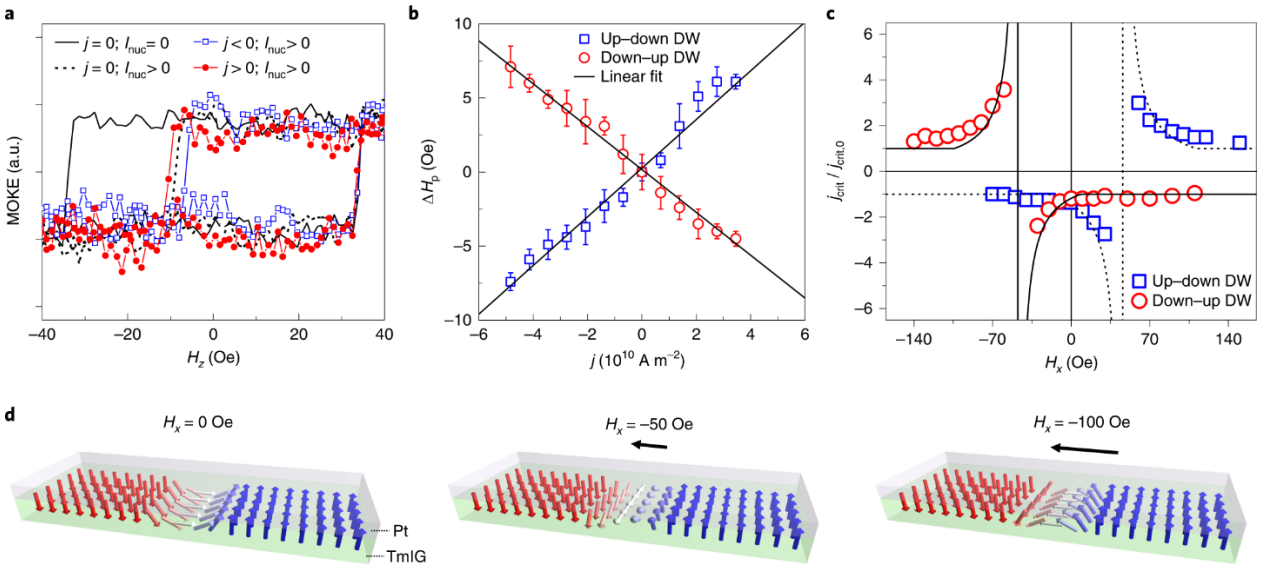

Figure 6.3: (a): Dependence of the field-induced domain-wall depinning (~ -10 Oe) on current injection showing that the SOT exerts an effective out-of-plane field. (b): Domain-wall depinning field as function of injected current density. (c): Critical switching current as a function of in-plane field. (d): Schematic showing the evolution of a chiral Neél wall as a function of in-plane field. Reprinted from Avci *et al* (2019)[13] with permission.

6.3 Interfacial Dzyaloshinskii-Moriya Interaction Arising from Rare-Earth Orbital Magnetism in Insulating Magnetic Oxides

Following the discovery of DMI in Pt/REIG heterostructures, a more in-depth investigation was carried out to determine the possible origins of the interaction[11]. Thin films of TmIG ranging in thickness from 2.4 nm to 24 nm were grown. The structural and magnetic characteristics of the thin films are displayed in figure 6.4. The good epitaxial quality of the films is evident from the XRD and the cross-sectional HAADF STEM measurements. Interestingly, VSM reveal a magnetic dead layer at the substrate interface approximately 1.4 nm in thickness. EELS

measurements show that this is likely due to interdiffusion of Gd and Ga from the substrate into the film.

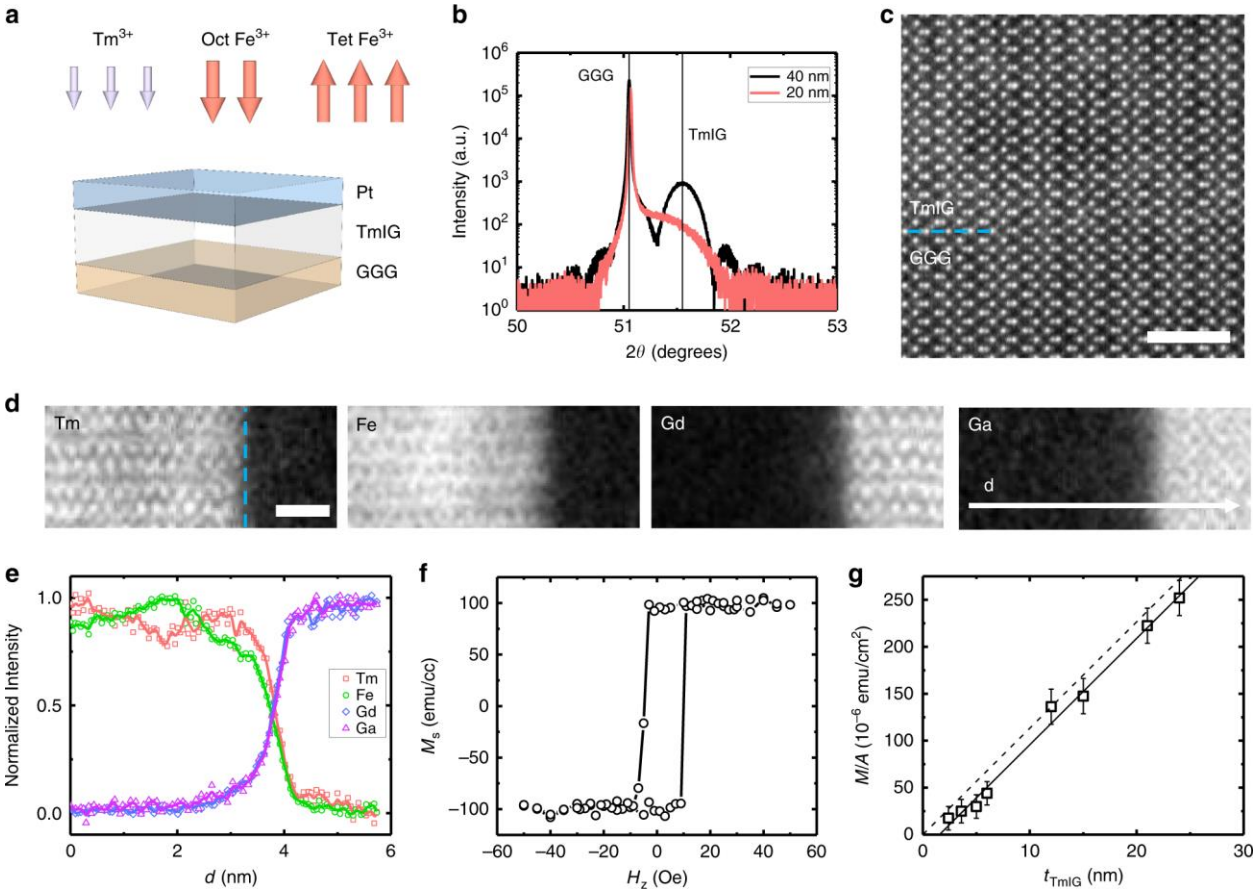

Figure 6.4: (a): Schematic of the thin film heterostructures studied in this work. (b): Exemplary XRD patterns from thick TmIG/GGG (111) thin films. (c-e): Cross-sectional TEM and elemental mapping from a TmIG/GGG (111) thin film showing high epitaxial quality and interdiffusion with the substrate. (f): Exemplary OOP VSM hysteresis loop from a 12 nm thick TmIG/GGG thin film. (g): Areal magnetization vs. TmIG thickness.

The DMI was measured using the same domain wall motion method discussed in the previous section (see Figure 6.5). By applying in-plane fields along the current direction, the Néel character (chirality) of the domain walls could be switched and detected by the efficiency of

current-induced domain wall motion (Figure 6.5a,b). Only films under 12 nm showed a remanent Néel wall (in the absence of an in-plane field). The DMI strength was found to vary inversely with the thickness, implying that the DMI is an interfacial rather than a bulk interaction (Figure 6.5c). Also, the SOT efficiency χ scaled inversely with the thickness implying a constant spin Hall angle over the range of thicknesses studied (Figure 6.5d).

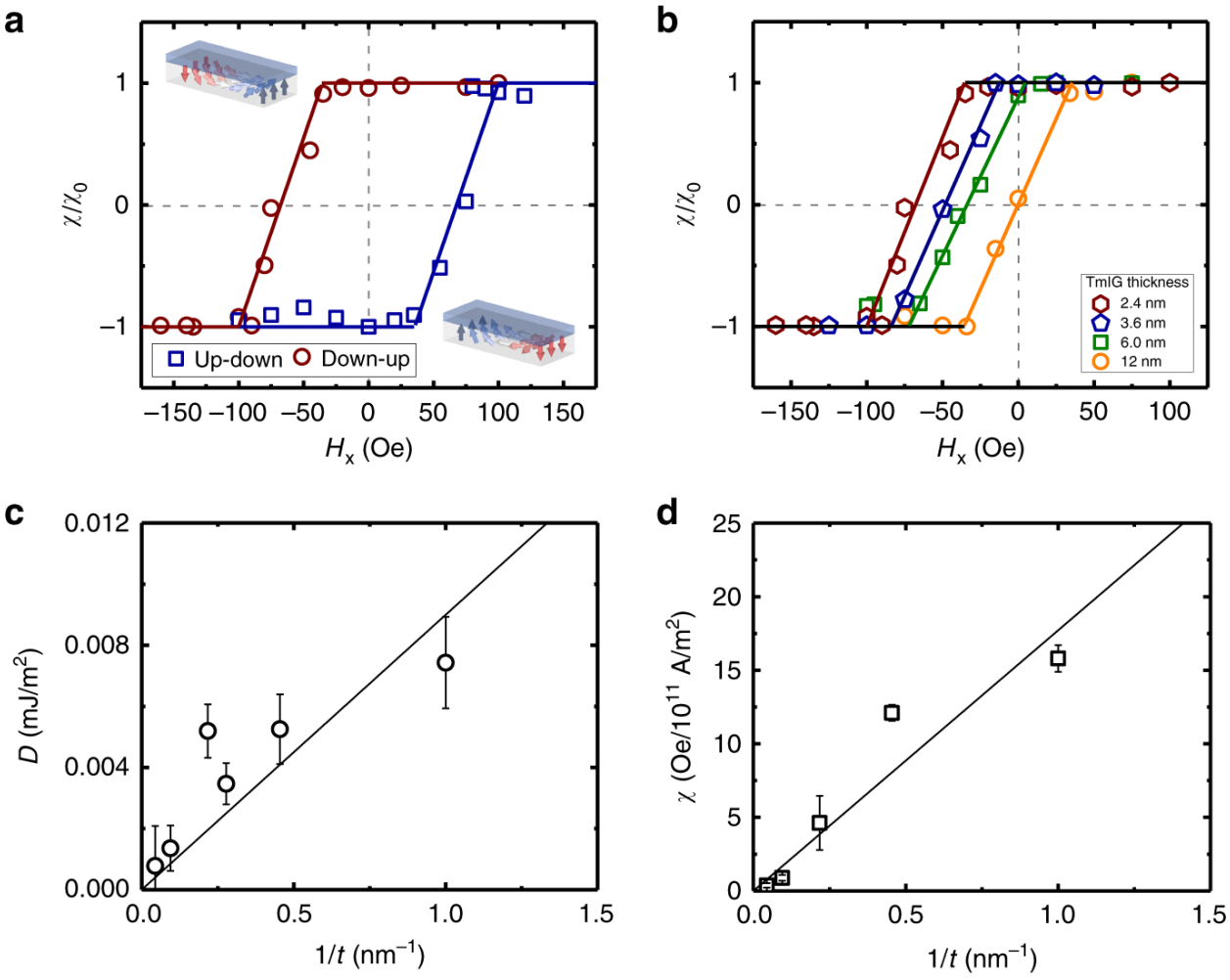

Figure 6.5: (a-b): Normalized SOT efficiency versus in-plane field for down-up and up-down domain walls (a) and for TmIG films of different thicknesses (b). (c): DMI energy as a function of TmIG thickness. (d): SOT efficiency as a function of thickness.

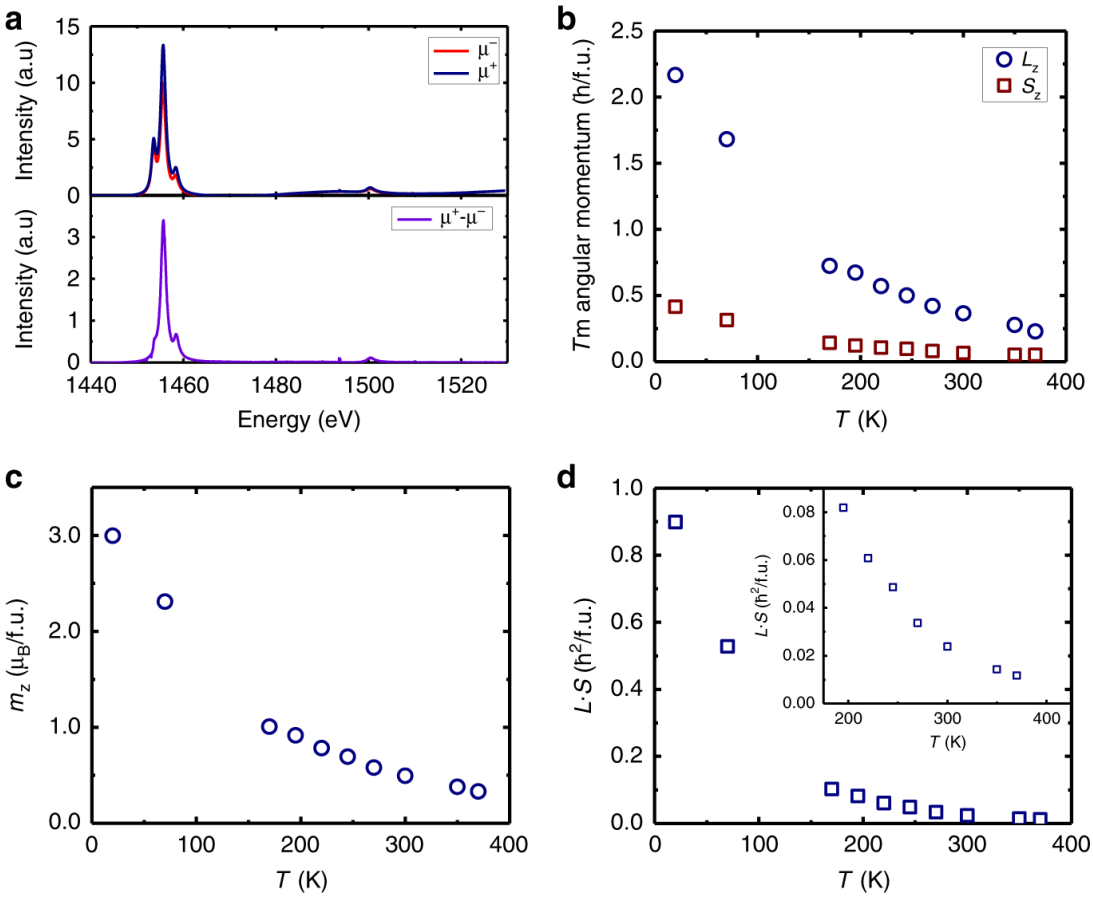

Figure 6.6: (a): Exemplary Tm polarization-dependent XAS (top) and XMCD (bottom) spectra. (b): Tm orbital and spin angular momentum as a function of temperature, derived from XMCD sum rules. (c): Tm magnetization as a function of temperature. (d): Tm SOC strength as a function of temperature.

Finally, XMCD measurements were performed as a first step towards uncovering the physical origins of interfacial DMI in REIG materials. Spin-orbit coupling (SOC) is a necessary component for DMI (see Chapter 1) and Fe^{3+} has a quenched orbital angular momentum in solids so the Tm^{3+} ions were the logical place to look. Using XMCD sum rules[161], the orbital (spin) angular momentum **L** (**S**), magnetic moment m_z, and SOC strength **L**·**S** of the Tm^{3+} ions were extracted (Figure 6.6). The SOC strength was found to be strongly temperature dependent, with

L·**S** increasing dramatically at low temperatures. Temperature-dependent DMI measurements were conducted and the DMI field was found to vary in the same way. This implies that the rare-earth ion SOC is involved in the DMI mechanism within REIG thin film heterostructures.

Chapter 7: Conclusion

In this thesis, the magnetic and spintronic properties of rare-earth iron garnet (REIG) thin films were investigated. These materials show great promise for future applications involving spin-orbit torque switching and current-induced domain wall motion due to their record-breaking domain wall velocities and highly tunable magnetic properties. However, the great complexity of the REIG materials system (especially regarding its tolerance for defects) also brings about challenges in understanding the relationship between growth and materials properties.

In Chapter 1, the motivation for this work was presented and the theoretical background was reviewed. Special attention was given to the sources of anisotropy in REIG materials. Spintronic phenomena and domain/domain wall structures of importance to the remainder of the theses were also covered.

In Chapter 2, the main experimental methods used in this work were reviewed. The operating principles and major mathematical relationships were presented, and specific recipes or procedures were covered when applicable.

In Chapter 3, two novel REIG thin film materials – EuIG and TbIG – were reported. Strain-induced PMA and pseudomorphic growth were achieved in both materials up to thicknesses exceeding 50 nm. The spin-mixing conductance – a measure of the transparency of normal metal/ferrimagnetic insulator interfaces to spin – was measured and found to be insensitive to the rare-earth ion and the orientation. The composition of these materials was found to be iron-deficient with large concentrations of charge defects (Tb^{4+} and Eu^{2+}). The compensation point of TbIG was found to be roughly 80 K higher in the thin film than in the bulk.

In Chapter 4, the compensation temperature of TbIG was revisited. Through a combination of T_{Curie} measurements, XAS/XMCD analysis, Rietveld refinement, and molecular field simulations, a model involving iron vacancies and terbium antisite defects was constructed which reproduced the observed compensation temperature.

In Chapter 5, the growth and magnetic characterization of Y-substituted TmIG (YTmIG) thin films were presented. Y substitution was found to have a profound impact on the anisotropy and the remanent domain structure in YTmIG thin films, with behavior running the gamut from strong PMA to remanent stripe domains to in-plane anisotropy over the composition range studied. Detailed calculations of the different anisotropy contributions in YTmIG revealed a strong contribution from growth-induced anisotropy – one of the first reports of this type of anisotropy in PLD-grown garnet thin films.

In Chapter 6, three coauthored spintronic studies to which the author contributed garnet thin films were reviewed. In the first, the optimization of the garnet growth recipe was shown to greatly improve previously reported values of the spin-mixing conductance and fast, efficient SOT switching was achieved. In the second and third, the Dzyaloshinskii-Moriya interaction (DMI) in Pt/REIG heterostructues was studied, with ultrafast domain wall velocities reported. Evidence that the rare-earth ion spin-orbit coupling is involved in the DMI was presented.

There is great potential for future work in the REIG thin film field. The appearance of growth-induced anisotropy in mixed garnets such as YTmIG implies that different combinations of ions may give enough anisotropy to achieve PMA even without strain. Also, the classical garnet literature[18] reports that (110)-oriented mixed garnets can display orthorhombic anisotropy, which could facilitate field-free SOT switching.

Questions still remain regarding the existence of a higher-than-bulk compensation temperature in TbIG. Our defect model accurately reproduces the compensation temperature, but the question of *why* the defects occur during PLD growth is still open. It is especially interesting that polycrystalline garnet thin films show bulk-like compensation temperatures while single-crystal thin films show discrepancies[62]. Studies in which the RE:Fe ratio is varied through codeposition may shed more light on how nonstoichiometry is accommodated through defects, and changing the RE ion to one which is too large to sit on Fe octahedral sites could provide more information in support of Tb antisite defects. Finally, point-defect-sensitive methods such as resonant x-ray diffraction could provide definitive proof for the existence of vacancies and antisite defects in REIG thin films.

Works Cited

[1] S.-W. Lee and K.-J. Lee, Proc. IEEE **104**, 1831 (2016).

[2] D. Apalkov, B. Dieny, and J.M. Slaughter, Proc. IEEE **104**, 1796 (2016).

[3] E. Technologies, M. Ddr, and S.- Mram, 3 (2016).

[4] K. Garello, C.O. Avci, I.M. Miron, M. Baumgartner, A. Ghosh, S. Auffret, O. Boulle, G. Gaudin, and P. Gambardella, Appl. Phys. Lett. **105**, 212402 (2014).

[5] G. Prenat, K. Jabeur, P. Vanhauwaert, G. Di Pendina, F. Oboril, R. Bishnoi, M. Ebrahimi, N. Lamard, O. Boulle, K. Garello, J. Langer, B. Ocker, M.-C. Cyrille, P. Gambardella, M. Tahoori, and G. Gaudin, IEEE Trans. Multi-Scale Comput. Syst. **2**, 49 (2016).

[6] M. Cubukcu, O. Boulle, M. Drouard, K. Garello, C. Onur Avci, I. Mihai Miron, J. Langer, B. Ocker, P. Gambardella, and G. Gaudin, Appl. Phys. Lett. **104**, 042406 (2014).

[7] A. van den Brink, S. Cosemans, S. Cornelissen, M. Manfrini, A. Vaysset, W. Van Roy, T. Min, H.J.M. Swagten, and B. Koopmans, Appl. Phys. Lett. **104**, 012403 (2014).

[8] A.D. Kent and D.C. Worledge, Nat. Nanotechnol. **10**, 187 (2015).

[9] P. Li, T. Liu, H. Chang, A. Kalitsov, W. Zhang, G. Csaba, W. Li, D. Richardson, A. DeMann, G. Rimal, H. Dey, J.S. Jiang, W. Porod, S.B. Field, J. Tang, M.C. Marconi, A. Hoffmann, O. Mryasov, and M. Wu, Nat. Commun. **7**, 12688 (2016).

[10] C.O. Avci, A. Quindeau, C.-F. Pai, M. Mann, L. Caretta, A.S. Tang, M.C. Onbasli, C.A. Ross, and G.S.D. Beach, Nat. Mater. (2016).

[11] L. Caretta, E. Rosenberg, F. Büttner, T. Fakhrul, P. Gargiani, M. Valvidares, Z. Chen, P.

Reddy, D.A. Muller, C.A. Ross, and G.S.D. Beach, Nat. Commun. **11**, 1 (2020).

[12] L. Caretta, S.H. Oh, T. Fakhrul, D.K. Lee, B.H. Lee, S.K. Kim, C.A. Ross, K.J. Lee, and G.S.D. Beach, Science **370**, 1438 (2020).

[13] C.O. Avci, E. Rosenberg, L. Caretta, F. Büttner, M. Mann, C. Marcus, D. Bono, C.A. Ross, and G.S.D. Beach, Nat. Nanotechnol. **14**, 561 (2019).

[14] C.O. Avci, E. Rosenberg, M. Baumgartner, L. Beran, A. Quindeau, P. Gambardella, C.A. Ross, and G.S.D. Beach, Appl. Phys. Lett. **111**, 072406 (2017).

[15] S. Vélez, J. Schaab, M.S. Wörnle, M. Müller, E. Gradauskaite, P. Welter, C. Gutgsell, C. Nistor, C.L. Degen, M. Trassin, M. Fiebig, and P. Gambardella, Nat. Commun. **10**, 1 (2019).

[16] S. Ding, A. Ross, R. Lebrun, S. Becker, K. Lee, I. Boventer, S. Das, Y. Kurokawa, S. Gupta, J. Yang, G. Jakob, and M. Kläui, Phys. Rev. B **100**, 100406 (2019).

[17] H. Forestier and G. Guiot-Guillain, (1950).

[18] A.H. Eschenfelder, *Magnetic Bubble Technology* (Springer Berlin Heidelberg, Berlin, Heidelberg, 1980).

[19] S.C. Abrahams and S. Geller, Acta Crystallogr. **11**, 437 (1958).

[20] P.W. Anderson, Phys. Rev. **115**, 2 (1959).

[21] R. O'Handley, *Modern Magnetic Materials: Principles and Applications*, 1st ed. (Wiley, New York, NY, 1999).

[22] J. Kanamori, J. Phys. Chem. Solids **10**, 87 (1959).

[23] G.F. Dionne, *Magnetic Oxides*, 1st ed. (Springer Science+Business Media, New York, NY,

2009).

[24] L. Néel, Proc. Phys. Soc. Sect. A **65**, 869 (1952).

[25] E.E. Anderson, Phys. Rev. **134**, A1581 (1964).

[26] W.P. Wolf and J.H. Van Vleck, Phys. Rev. **118**, 1490 (1960).

[27] L. Caretta, M. Mann, F. Büttner, K. Ueda, B. Pfau, C.M. Günther, P. Hessing, A. Churikova, C. Klose, M. Schneider, D. Engel, C. Marcus, D. Bono, K. Bagschik, S. Eisebitt, and G.S.D. Beach, Nat. Nanotechnol. **13**, 1154 (2018).

[28] J. Finley and L. Liu, Phys. Rev. Appl. **6**, 054001 (2016).

[29] A. Hubert and R. Schäfer, *Magnetic Domains : The Analysis of Magnetic Microstructures* (Springer, 1998).

[30] J.C. Slonczewski, J. Appl. Phys. **32**, 253 (1961).

[31] J.C. Slonczewski, *Origin of Magnetic Anisotropy in Cobalt-Substituted Magnetite** (1958).

[32] K.-H. Hellwege and A.M. Hellwege, editors , *Landolt-Börnstein - Group III Crystal and Solid State Physics Vol 12a* (Springer-Verlag, Berlin/Heidelberg, 1978).

[33] S. Iida, J. Phys. Soc. Japan **22**, 1201 (1967).

[34] R.L. White, IEEE Trans. Magn. **9**, 606 (1973).

[35] H. Callen, Appl. Phys. Lett. **18**, 311 (1971).

[36] S. Chikazumi, *Physics of Ferromagnetism*, 2nd ed. (Oxford University Press, Oxford, 1997).

[37] A.H. Eschenfelder, J. Appl. Phys. **49**, 1891 (1978).

[38] F.B. Hagedorn, J. Appl. Phys. **45**, 3123 (1974).

[39] R. Wolfe, R.C. LeCraw, S.L. Blank, and R.D. Pierce, **172**, 172 (2009).

[40] S.A. Manuilov, S.I. Khartsev, and A.M. Grishin, J. Appl. Phys. J. Appl. Phys. Submicron Film Magnetostatic Wave Band Pass Filters J. Appl. Phys. **1063446840**, 123917 (2009).

[41] L. Soumah, N. Beaulieu, L. Qassym, C. Carrétéro, E. Jacquet, R. Lebourgeois, J. Ben Youssef, P. Bortolotti, V. Cros, and A. Anane, (n.d.).

[42] T. Hibiya, H. Makino, and S. Konishi, J. Appl. Phys. **52**, 7347 (1981).

[43] E.R. Rosenberg, L. Beran, C.O. Avci, C. Zeledon, B. Song, C. Gonzalez-Fuentes, J. Mendil, P. Gambardella, M. Veis, C. Garcia, G.S.D. Beach, and C.A. Ross, Phys. Rev. Mater. **2**, 094405 (2018).

[44] M.W. Muller, Phys. Rev. **122**, 1485 (1961).

[45] C. Kooy and U. Enz, Philips Res. Repts **15**, 17 (1960).

[46] C. Kittel, Phys. Rev. **70**, 965 (1946).

[47] B. Kaplan and G.A. Gehring, J. Magn. Magn. Mater. **128**, 111 (1993).

[48] R. Skomski, H.-P. Oepen, and J. Kirschner, *Micromagnetics of Ultrathin Films with Perpendicular Magnetic Anisotropy* (1998).

[49] I. Lemesh, F. Büttner, and G.S.D. Beach, Phys. Rev. B **95**, 174423 (2017).

[50] A. Thiaville, S. Rohart, E. Jué, V. Cros, and A. Fert, (2012).

[51] H. Yang, A. Thiaville, S. Rohart, A. Fert, and M. Chshiev, (2015).

[52] M. Kubota, A. Tsukazaki, F. Kagawa, K. Shibuya, Y. Tokunaga, M. Kawasaki, and Y. Tokura, Appl. Phys. Express **5**, 103002 (2012).

[53] A. Quindeau, C.O. Avci, W. Liu, C. Sun, M. Mann, A.S. Tang, M.C. Onbasli, D. Bono, P.M. Voyles, Y. Xu, J. Robinson, G.S.D. Beach, and C.A. Ross, Adv. Electron. Mater. 1600376 (2016).

[54] S. Vélez, J. Schaab, M.S. Wörnle, M. Müller, E. Gradauskaite, P. Welter, C. Gutgsell, C. Nistor, C.L. Degen, M. Trassin, M. Fiebig, and P. Gambardella, Nat. Commun. **10**, 1 (2019).

[55] F. Büttner, M.A. Mawass, J. Bauer, E. Rosenberg, L. Caretta, ‡ Can, O. Avci, J. Gräfe, S. Finizio, C.A.F. Vaz, N. Novakovic, M. Weigand, K. Litzius, J. Förster, N. Träger, F. Groß, D. Suzuki, M. Huang, J. Bartell, F. Kronast, J. Raabe, G. Schütz, C.A. Ross, and G.S.D. Beach, Phys. Rev. Mater. **4**, (2020).

[56] C.N. Wu, C.C. Tseng, Y.T. Fanchiang, C.K. Cheng, K.Y. Lin, S.L. Yeh, S.R. Yang, C.T. Wu, T. Liu, M. Wu, M. Hong, and J. Kwo, Sci. RepoRTS | **8**, 11087 (2018).

[57] J. Fu, M. Hua, X. Wen, M. Xue, S. Ding, M. Wang, P. Yu, S. Liu, J. Han, C. Wang, H. Du, Y. Yang, and J. Yang, Appl. Phys. Lett. **110**, 202403 (2017).

[58] J. Ding, C. Liu, Y. Zhang, U. Erugu, Z. Quan, R. Yu, E. Mccollum, S. Mo, S. Yang, H. Ding, X. Xu, J. Tang, X. Yang, and M. Wu, Phys. Rev. Appl. **10**, 14017 (2020).

[59] E. Popova, A.F. Franco Galeano, M. Deb, B. Warot-Fonrose, H. Kachkachi, F. Gendron, F. Ott, B. Berini, and N. Keller, J. Magn. Magn. Mater. **335**, 139 (2013).

[60] X. Liu, Q. Yang, D. Zhang, Y. Wu, and H. Zhang, AIP Adv. **9**, 115001 (2019).

[61] J.J. Bauer, E.R. Rosenberg, and C.A. Ross, Appl. Phys. Lett. **114**, 052403 (2019).

[62] J.J. Bauer, E.R. Rosenberg, S. Kundu, K.A. Mkhoyan, P. Quarterman, A.J. Grutter, B.J. Kirby, J.A. Borchers, and C.A. Ross, Adv. Electron. Mater. **6**, 1900820 (2020).

[63] A. Vansteenkiste, J. Leliaert, M. Dvornik, M. Helsen, F. Garcia-Sanchez, and B. Van Waeyenberge, AIP Adv. **4**, 107133 (2014).

[64] J.C. Mallinson, IEEE Trans. Magn. **36**, 1976 (2000).

[65] M.D. Stiles and J. Miltat, in *Spin Dyn. Confin. Magn. Struct. III* (Springer Berlin Heidelberg, n.d.), pp. 225–308.

[66] P.M. Haney, H.-W. Lee, K.-J. Lee, A. Manchon, and M.D. Stiles, Phys. Rev. B **87**, 174411 (2013).

[67] Y.-T. Chen, S. Takahashi, H. Nakayama, M. Althammer, S.T.B. Goennenwein, E. Saitoh, and G.E.W. Bauer, J. Phys. Condens. Matter **28**, 103004 (2016).

[68] L. Liu, C.-F. Pai, Y. Li, H.W. Tseng, D.C. Ralph, and R.A. Buhrman, Science (80-.). **336**, (2012).

[69] L. Liu, O.J. Lee, T.J. Gudmundsen, D.C. Ralph, and R.A. Buhrman, Phys. Rev. Lett. **109**, 096602 (2012).

[70] A. Brataas, Y. V. Nazarov, and G.E.W. Bauer, Phys. Rev. Lett. **84**, 2481 (2000).

[71] K.-S. Lee, S.-W. Lee, B.-C. Min, and K.-J. Lee, Appl. Phys. Lett. **102**, 112410 (2013).

[72] N. Mikuszeit, O. Boulle, I.M. Miron, K. Garello, P. Gambardella, G. Gaudin, and L.D. Buda-Prejbeanu, Phys. Rev. B **92**, 144424 (2015).

[73] M. Collet, X. De Milly, O. D'Allivy Kelly, V. V. Naletov, R. Bernard, P. Bortolotti, J. Ben

Youssef, V.E. Demidov, S.O. Demokritov, J.L. Prieto, M. Muñoz, V. Cros, A. Anane, G. De Loubens, and O. Klein, Nat. Commun. **7**, 1 (2016).

[74] Q. Shao, C. Tang, G. Yu, A. Navabi, H. Wu, C. He, J. Li, P. Upadhyaya, P. Zhang, S.A. Razavi, Q.L. He, Y. Liu, P. Yang, S.K. Kim, C. Zheng, Y. Liu, L. Pan, R.K. Lake, X. Han, Y. Tserkovnyak, J. Shi, and K.L. Wang, Nat. Commun. **9**, 1 (2018).

[75] J. Li, G. Yu, C. Tang, Y. Liu, Z. Shi, Y. Liu, A. Navabi, M. Aldosary, Q. Shao, K.L. Wang, R. Lake, and J. Shi, Phys. Rev. B **95**, 241305 (2017).

[76] S. Foner, (1956).

[77] B. Bhoi, N. Venkataramani, S. Prasad, R.P.R.C. Aiyar, G. Kumar, I. Samajdar, and M. Kostylev, J. Magn. Magn. Mater. **483**, 191 (2019).

[78] U. Pietsch, V. Holy, and T. Baumbach, *High Resolution Xray Scattering* (2004).

[79] B.D. Cullity, *Elements of X-Ray Diffraction*, 2nd ed. (Addison-Wesley Publishing Company, Inc, Reading, MA, 1978).

[80] Y.-T. Chen, S. Takahashi, H. Nakayama, M. Althammer, S.T.B. Goennenwein, E. Saitoh, and G.E.W. Bauer, Phys. Rev. B **87**, (2013).

[81] N. Vlietstra, J. Shan, V. Castel, B.J. van Wees, and J. Ben Youssef, Phys. Rev. B **87**, 184421 (2013).

[82] J. Kerr, Phil. Mag. **3**, 321 (1877).

[83] L. Beran, Optical and Magneto-Optical Studies of Ferrimagnetic Garnets for Photonic and Spintronic Applications, Charles University, 2020.

[84] A.K. (Anatoliĭ K. Zvezdin and V.A. (Viâčheslav A. Kotov, *Modern Magnetooptics and Magnetooptical Materials* (CRC Press, Boca Raton, FL, 1997).

[85](n.d.).

[86] R.W. Vook, Int. Met. Rev. **27**, 245 (1982).

[87] R. Eason, editor , *Pulsed Laser Deposition of Thin Films* (John Wiley & Sons, Inc., Hoboken, NJ, USA, 2006).

[88] B. Shin and M.J. Aziz, (n.d.).

[89] B. Hinnemann, H. Hinrichsen, and D.E. Wolf, Phys. Rev. E - Stat. Physics, Plasmas, Fluids, Relat. Interdiscip. Top. **67**, 9 (2003).

[90] B. Shin, J.P. Leonard, J.W. McCamy, and M.J. Aziz, Appl. Phys. Lett. **87**, 1 (2005).

[91] P. Ohresser, J. Shen, J. Barthel, M. Zheng, C. V Mohan, M. Klaua, and J. Kirschner, *Growth, Structure, and Magnetism of Fcc Fe Ultrathin Films on Cu"111… by Pulsed Laser Deposition* (n.d.).

[92] B.B. Krichevtsov, S. V. Gastev, S.M. Suturin, V. V. Fedorov, A.M. Korovin, V.E. Bursian, A.G. Banshchikov, M.P. Volkov, M. Tabuchi, and N.S. Sokolov, Sci. Technol. Adv. Mater. **18**, 351 (2017).

[93] M. Aldosary, J. Li, C. Tang, Y. Xu, J.-G. Zheng, K.N. Bozhilov, and J. Shi, Appl. Phys. Lett. **108**, 242401 (2016).

[94] Y. Krockenberger, K.-S. Yun, T. Hatano, S. Arisawa, M. Kawasaki, and Y. Tokura, J. Appl. Phys. **106**, 123911 (2009).

[95] T. Gün, Y. Kuzminykh, F. Tellkamp, K. Petermann, and G. Huber, Appl. Phys. A Mater. Sci. Process. **93**, 387 (2008).

[96] R.K. Singh and J. Narayan, *Pulsed-Laser Evaporation Technique for Deposition of Thin Films: Physics and Theoretical Model* (1990).

[97] T. Ohnishi, H. Koinuma, and M. Lippmaa, in *Appl. Surf. Sci.* (Elsevier, 2006), pp. 2466–2471.

[98] N.. Ibrahim, C. Edwards, and S.. Palmer, J. Magn. Magn. Mater. **220**, 183 (2000).

[99] Y. Li, X. Yao, and K. Tanabe, J. Appl. Phys. **84**, 4797 (1998).

[100] K.H. Young, Phys. C Supercond. Its Appl. **211**, 1 (1993).

[101] Y. Kajiwara, K. Harii, S. Takahashi, J. Ohe, K. Uchida, M. Mizuguchi, H. Umezawa, H. Kawai, K. Ando, K. Takanashi, S. Maekawa, and E. Saitoh, Nature **464**, 262 (2010).

[102] K. Uchida, H. Adachi, T. Ota, H. Nakayama, S. Maekawa, and E. Saitoh, Appl. Phys. Lett. **97**, 172505 (2010).

[103] K. Uchida, H. Adachi, Y. Kajiwara, S. Maekawa, and E. Saitoh, in *Recent Adv. Magn. Insul. from Spintron. to Microw. Appl. Vol. 64*, edited by M. Wu and A. Hoffmann, 1st ed. (Academic Press, 2013), pp. 1–27.

[104] I.M. Miron, K. Garello, G. Gaudin, P.-J. Zermatten, M. V. Costache, S. Auffret, S. Bandiera, B. Rodmacq, A. Schuhl, and P. Gambardella, Nature **476**, 189 (2011).

[105] M. Kubota, K. Shibuya, Y. Tokunaga, F. Kagawa, A. Tsukazaki, Y. Tokura, and M. Kawasaki, J. Magn. Magn. Mater. **339**, 63 (2013).

[106] H. Wang, C. Du, P.C. Hammel, and F. Yang, Phys. Rev. B **89**, 134404 (2014).

[107] W. Yang, S. Yang, Q. Zhang, Y. Xu, S. Shen, J. Liao, J. Teng, C. Nan, L. Gu, Y. Sun, K. Wu, and Y. Li, Appl. Phys. Lett. **105**, 092411 (2014).

[108] P. Wei, F. Katmis, B.A. Assaf, H. Steinberg, P. Jarillo-Herrero, D. Heiman, and J.S. Moodera, Phys. Rev. Lett. **110**, 186807 (2013).

[109] M. Isasa, A. Bedoya-Pinto, S. Vélez, F. Golmar, F. Sánchez, L.E. Hueso, J. Fontcuberta, and F. Casanova, Appl. Phys. Lett. **105**, 142402 (2014).

[110] P.C. Dorsey, P. Lubitz, D.B. Chrisey, and J.S. Horwitz, J. Appl. Phys. **79**, 6338 (1998).

[111] H. Yamahara, M. Mikami, M. Seki, and H. Tabata, J. Magn. Magn. Mater. **323**, 3143 (2011).

[112] N. Kumar, N.G. Kim, Y.A. Park, N. Hur, J.H. Jung, K.J. Han, and K.J. Yee, Thin Solid Films **516**, 7753 (2008).

[113] E. Lage, L. Beran, A.U. Quindeau, L. Ohnoutek, M. Kucera, R. Antos, S.R. Sani, G.F. Dionne, M. Veis, and C.A. Ross, APL Mater. **5**, 036104 (2017).

[114] P. Sellappan, C. Tang, J. Shi, and J.E. Garay, Mater. Res. Lett. **5**, 41 (2017).

[115] S. Geprägs, A. Kehlberger, F. Della Coletta, Z. Qiu, E.-J. Guo, T. Schulz, C. Mix, S. Meyer, A. Kamra, M. Althammer, H. Huebl, G. Jakob, Y. Ohnuma, H. Adachi, J. Barker, S. Maekawa, G.E.W. Bauer, E. Saitoh, R. Gross, S.T.B. Goennenwein, and M. Kläui, Nat. Commun. **7**, 10452 (2016).

[116] C.L. Jermain, H. Paik, S. V. Aradhya, R.A. Buhrman, D.G. Schlom, and D.C. Ralph, Appl. Phys. Lett. **109**, 192408 (2016).

[117] C.N. Wu, C.C. Tseng, K.Y. Lin, C.K. Cheng, S.L. Yeh, Y.T. Fanchiang, M. Hong, and J. Kwo, Cit. AIP Adv. **8**, (2018).

[118] C. Tang, P. Sellappan, Y. Liu, Y. Xu, J.E. Garay, and J. Shi, Phys. Rev. B **94**, 140403 (2016).

[119] Y. Sun, Y.-Y. Song, H. Chang, M. Kabatek, M. Jantz, W. Schneider, M. Wu, H. Schultheiss, and A. Hoffmann, Cit. Appl. Phys. Lett. J. Appl. Phys. J. Appl. Phys. **101**, 152405 (2012).

[120] D.-Y. Lu, T. Ogata, H. Unuma, X.-C. Li, N.-N. Li, and X.-Y. Sun, Solid State Ionics **201**, 6 (2011).

[121] D.-Y. Lu, Solid State Ionics **276**, 98 (2015).

[122] M. Balaguer, C.-Y. Yoo, H.J.M. Bouwmeester, and J.M. Serra, J. Mater. Chem. A **1**, 10234 (2013).

[123] E.-J. Cho and S.-J. Oh, Phys. Rev. B **59**, R15613 (1999).

[124] D.H. Kim, N.M. Aimon, L. Bi, J.M. Florez, G.F. Dionne, and C.A. Ross, J. Phys. Condens. Matter **25**, 026002 (2013).

[125] Z. Zhou, Y. Zhang, Z. Wang, W. Wei, W. Tang, J. Shi, and R. Xiong, Appl. Surf. Sci. **254**, 6972 (2008).

[126] T.-C. Lin, G. Seshadri, and J.A. Kelber, Appl. Surf. Sci. **119**, 83 (1997).

[127] T. Taffary, D. Autissier, F. Boust, and H. Pascard, IEEE Trans. Magn. **34**, 1384 (1998).

[128] V. Sharma and B.K. Kuanr, J. Alloys Compd. **748**, 591 (2018).

[129] M. Weiler, G. Woltersdorf, M. Althammer, H. Huebl, and S.T.B. Goennenwein, in *Solid State Phys. - Adv. Res. Appl.* (2013), pp. 123–156.

[130] B.F. Miao, S.Y. Huang, D. Qu, and C.L. Chien, Phys. Rev. Lett. **112**, 236601 (2014).

[131] M. Althammer, S. Meyer, H. Nakayama, M. Schreier, S. Altmannshofer, M. Weiler, H.

Huebl, S. Geprägs, M. Opel, R. Gross, D. Meier, C. Klewe, T. Kuschel, J.-M. Schmalhorst, G. Reiss, L. Shen, A. Gupta, Y.-T. Chen, G.E.W. Bauer, E. Saitoh, and S.T.B. Goennenwein, Phys. Rev. B **87**, 224401 (2013).

[132] S. Geprägs, S. Meyer, S. Altmannshofer, M. Opel, F. Wilhelm, A. Rogalev, R. Gross, and S.T.B. Goennenwein, Appl. Phys. Lett. **101**, 262407 (2012).

[133] Y.M. Lu, Y. Choi, C.M. Ortega, X.M. Cheng, J.W. Cai, S.Y. Huang, L. Sun, and C.L. Chien, Phys. Rev. Lett. **110**, 147207 (2013).

[134] S. Geprägs, S.T.B. Goennenwein, M. Schneider, F. Wilhelm, K. Ollefs, A. Rogalev, M. Opel, and R. Gross, (2013).

[135] T. Kuschel, C. Klewe, J.-M. Schmalhorst, F. Bertram, O. Kuschel, T. Schemme, J. Wollschläger, S. Francoual, J. Strempfer, A. Gupta, M. Meinert, G. Götz, D. Meier, and G. Reiss, Phys. Rev. Lett. **115**, 097401 (2015).

[136] C. Onur Avci, E. Rosenberg, J. Mendil, L. Beran, P. Gambardella, C.A. Ross, and G.S.D. Beach, (n.d.).

[137] A.B. Cahaya, A.O. Leon, and G.E.W. Bauer, Phys. Rev. B **96**, 144434 (2017).

[138] K. Ganzhorn, J. Barker, R. Schlitz, B.A. Piot, K. Ollefs, F. Guillou, F. Wilhelm, A. Rogalev, M. Opel, M. Althammer, S. Geprägs, H. Huebl, R. Gross, G.E.W. Bauer, and S.T.B. Goennenwein, Phys. Rev. B **94**, 094401 (2016).

[139] M. Guillot, H. Le Gall, J.M. Desvignes, and M. Artinian, IEEE Trans. Magn. **30**, 4419 (1994).

[140] C. Gonzalez-Fuentes, R.K. Dumas, and C. García, J. Appl. Phys. **123**, 023901 (2018).

[141] J.E.R. Ibarra, MAGNETIC IONS-DOPED ZnO NANOCRYSTALS: STUDY OF THE STRUCTURAL, ELECTRONIC, OPTICAL AND MAGNETIC PROPERTIES, Universidade de Brasilia, 2018.

[142] Q. Shao, A. Grutter, Y. Liu, G. Yu, C.-Y. Yang, D.A. Gilbert, E. Arenholz, P. Shafer, X. Che, C. Tang, M. Aldosary, A. Navabi, Q. Lin He, B.J. Kirby, J. Shi, and K.L. Wang, *Exploring Interfacial Exchange Coupling and Sublattice Effect in Heavy Metal/Ferrimagnetic Insulator Heterostructures Using Hall Measurement, XMCD and Neutron Reflectometry* (n.d.).

[143] M. Kuila, Z. Hussain, and V.R. Reddy, J. Magn. Magn. Mater. **473**, 458 (2019).

[144] Y.K. Liu, H.F. Wong, K.K. Lam, K.H. Chan, C.L. Mak, and C.W. Leung, J. Magn. Magn. Mater. **468**, 235 (2018).

[145] H.-A. Zhou, Y. Dong, T. Xu, K. Xu, L. Sánchez-Tejerina, L. Zhao, Y. Ba, P. Gargiani, M. Valvidares, Y. Zhao, M. Carpentieri, O.A. Tretiakov, X. Zhong, G. Finocchio, S.K. Kim, and W. Jiang, ArXiv (2019).

[146] L. Liensberger, A. Kamra, H. Maier-Flaig, S. Geprägs, A. Erb, S.T.B. Goennenwein, R. Gross, W. Belzig, H. Huebl, and M. Weiler, Phys. Rev. Lett. **123**, 117204 (2019).

[147] B.W. Dong, J. Cramer, K. Ganzhorn, H.Y. Yuan, E.J. Guo, S.T.B. Goennenwein, and M. Klaui, J. Phys. Condens. Matter **30**, 035802 (2018).

[148] P. Hansen, J. Appl. Phys. **45**, 3638 (1974).

[149] M. Oron, I. Barlow, and W.F. Traber, *Ferrimagnetic Garnet Thin Films: Growth, Structure and Some Magnetic Properties* (1969).

[150] G. Van Der Laan, J. Electron Spectros. Relat. Phenomena **86**, 41 (1997).

[151] P.H. Butler, *Point Group Symmetry Applications: Methods and Tables* (Plenum Press, New York, NY, 1981).

[152] C. Carvallo, P. Sainctavit, M.A. Arrio, N. Menguy, Y. Wang, G. Ona-Nguema, and S. Brice-Profeta, Am. Mineral. **93**, 880 (2008).

[153] G. Cressey, C.M.B. Henderson, and G. van der Laan, Phys. Chem. Miner. **20**, 111 (1993).

[154] P. Kuiper, B.G. Searle, L.C. Duda, R.M. Wolf, and P.J. Van Der Zaag, J. Electron Spectros. Relat. Phenomena **86**, 107 (1997).

[155] R.A.D. Pattrick, G. Van Der Laan, C.M.B. Henderson, P. Kuiper, E. Dudzik, and D.J. Vaughan, Eur. J. Mineral. **14**, 1095 (2002).

[156] J.C. Fuggle and J.E. Inglesfield, editors , *Unoccupied Electronic States* (Springer Berlin Heidelberg, Berlin, Heidelberg, 1992).

[157] F.M.F. De Groot, J.C. Fuggle, B.T. Thole, and G.A. Sawatzky, Phys. Rev. B **42**, 5459 (1990).

[158](n.d.).

[159] Z. Zheng-Wu, W. Ping-Feng, Y. Jian-Hua, and Z. Kang-Wei, Phys. Rev. B **48**, 16407 (1993).

[160] B. Liu, C. Piamonteze, M.U. Delgado-Jaime, R.P. Wang, J. Heidler, J. Dreiser, R. Chopdekar, F. Nolting, and F.M.F. De Groot, Phys. Rev. B **96**, 1 (2017).

[161] F.M.F. de Groot and A. Kotani, *Core Level Spectroscopy of Solids* (CRC Press, Boca Raton, FL, 2008).

[162] H.B. Vasili, B. Casals, R. Cichelero, F. Macià, J. Geshev, P. Gargiani, M. Valvidares, J. Herrero-Martin, E. Pellegrin, J. Fontcuberta, and G. Herranz, Phys. Rev. B **96**, 1 (2017).

[163] G.F. Dionne, Http://Oasc12039.247realmedia.Com/RealMedia/Ads/Click_lx.Ads/Www.Aip.Org/Pt/Adcenter/Pdfcover_test/L-37/386502181/X01/AIP-PT/JAP_ArticleDL_092017/Scilight717-1640x440.Gif/434f71374e315a556e61414141774c75?X (1999).

[164] M.A. Gilleo and S. Geller, J. Appl. Phys. **29**, 380 (1958).

[165] M. Lahoubi, M. Guillot, A. Marchand, F. Tcheou, and E. Roudault, IEEE Trans. Magn. **20**, 1518 (1984).

[166] S. Geller, J. Appl. Phys. **37**, 1408 (1966).

[167] G. Vilela, H. Chi, G. Stephen, C. Settens, P. Zhou, Y. Ou, D. Suri, D. Heiman, and J.S. Moodera, J. Appl. Phys. **127**, 115302 (2020).

[168] V.H. Ortiz, M. Aldosary, J. Li, Y. Xu, M.I. Lohmann, P. Sellappan, Y. Kodera, J.E. Garay, and J. Shi, APL Mater. **6**, 121113 (2018).

[169] S. Mokarian Zanjani and M.C. Onbaşlı, J. Magn. Magn. Mater. **499**, 166108 (2020).

[170] G. Li, H. Bai, J. Su, Z.Z. Zhu, Y. Zhang, and J.W. Cai, APL Mater. **7**, 041104 (2019).

[171] Y. Zhang, Q. Du, C. Wang, W. Yan, L. Deng, J. Hu, C.A. Ross, and L. Bi, APL Mater. **7**, 081119 (2019).

[172] S.A. Manuilov, S.I. Khartsev, and A.M. Grishin, J. Appl. Phys. **106**, 123917 (2009).

[173] S.A. Manuilov and A.M. Grishin, J. Appl. Phys. J. Appl. Phys. J. Appl. Phys. J. Appl. Phys. Appl. Phys. Lett. **1081**, 13902 (2010).

[174] S.A. Manuilov, R. Fors, S.I. Khartsev, and A.M. Grishin, J. Appl. Phys. **105**, 033917 (2009).

[175] B. Bhoi, B. Kim, Y. Kim, M.K. Kim, J.H. Lee, and S.K. Kim, J. Appl. Phys. **123**, 203902 (2018).

[176] J.C. Gallagher, A.S. Yang, J.T. Brangham, B.D. Esser, S.P. White, M.R. Page, K.Y. Meng, S. Yu, R. Adur, W. Ruane, S.R. Dunsiger, D.W. McComb, F. Yang, and P.C. Hammel, Appl. Phys. Lett. **109**, 072401 (2016).

[177] R. Kumar, Z. Hossain, and R.C. Budhani, J. Appl. Phys. **121**, 113901 (2017).

[178] S. Estraḋ, J.M. Rebled, J. Arbiol, F. Peiró, I.C. Infante, G. Herranz, F. Sánchez, J. Fontcuberta, R. Córdoba, B.G. Mendis, and A.L. Bleloch, Appl. Phys. Lett. **95**, 072507 (2009).

[179] A. Bhattacharya and S.J. May, (2014).

[180] R. Bertacco, J.P. Contour, A. Barthélemy, and J. Olivier, Surf. Sci. **511**, 366 (2002).

[181] R.D. Shannon, *Revised Effective Ionic Radii and Systematic Studies of Interatomie Distances in Halides and Chaleogenides* (1976).

[182] B.D. Cullity and C.D. Graham, *Introduction to Magnetic Materials*, 1st ed. (John Wiley & Sons, Inc., Hoboken, NJ, USA, 2008).

[183] E.A. Geiss, J.E. Davies, C.F. Guerci, and H.L. Hu, Mater. Res. Bull. **10**, 355 (1975).

[184] R. Wolfe, R.C. LeCraw, S.L. Blank, and R.D. Pierce, Appl. Phys. Lett **815**, 815 (1976).

[185] N. Nakamura, H. Ogi, M. Hirao, T. Fukuhara, K. Shiroki, and N. Imaizumi, Jpn. J. Appl. Phys. **47**, 3851 (2008).

[186] H.T. Nembach, T.J. Silva, J.M. Shaw, M.L. Schneider, M.J. Carey, S. Maat, and J.R. Childress, Phys. Rev. B - Condens. Matter Mater. Phys. **84**, 054424 (2011).

[187] Y. Ding, T.J. Klemmer, and T.M. Crawford, J. Appl. Phys. **96**, 2969 (2004).

[188] I. Neudecker, G. Woltersdorf, B. Heinrich, T. Okuno, G. Gubbiotti, and C.H. Back, J. Magn. Magn. Mater. **307**, 148 (2006).

[189] S.S. Kalarickal, P. Krivosik, M. Wu, C.E. Patton, M.L. Schneider, P. Kabos, T.J. Silva, and J.P. Nibarger, J. Appl. Phys. **99**, 093909 (2006).

[190] B. Heinrich, J.F. Cochran, and R. Hasegawa, J. Appl. Phys. **57**, 3690 (1985).

[191] C. Kittel, Phys. Rev. **115**, 1587 (1959).

[192] T.B. Mitchell and P.E. Wigen, J. Appl. Phys. **61**, 3259 (1987).

[193] M.C. Onbasli, A. Kehlberger, D.H. Kim, G. Jakob, M. Kläui, A. V. Chumak, B. Hillebrands, and C.A. Ross, APL Mater. **2**, 106102 (2014).

[194] S. Crossley, A. Quindeau, A.G. Swartz, E.R. Rosenberg, L. Beran, C.O. Avci, Y. Hikita, C.A. Ross, and H.Y. Hwang, Appl. Phys. Lett. **115**, 172402 (2019).

[195] P.-G. De Gennes, C. Kittel, and A.M. Portis, *Theory of Ferromagnetic Resonance in Rare Earth Garnets. II. Line Widths~* (n.d.).

[196] M.H. Sirvetz and J.E. Zneimer, J. Appl. Phys. **29**, 431 (1958).

[197] R. Schäfer, J. Magn. Magn. Mater. **215**, 652 (2000).

[198] J. Barak, M.X. Huang, and S.M. Bhagat, J. Appl. Phys. **71**, 849 (1992).

[199] S.H. Yang, K.S. Ryu, and S. Parkin, Nat. Nanotechnol. **10**, 221 (2015).

[200] R.K. Wangsness, Phys. Rev. **91**, 1085 (1953).